CFD MODELLING AND EXPERIMENTAL INVESTIGATIONS OF AIR WATER FLOW THROUGH SERPENTINE CHANNEL

Ph.D. THESIS

by

SNEHA MALHOTRA

DEPARTMENT OF CHEMICAL ENGINEERING
INDIAN INSTITUTE OF TECHNOLOGY ROORKEE
ROORKEE - 247667 (INDIA)
FEBRUARY, 2019

CFD MODELLING AND EXPERIMENTAL INVESTIGATIONS OF AIR WATER FLOW THROUGH SERPENTINE CHANNEL

A THESIS

Submitted in partial fulfilment of the requirements for the award of the degree

of

DOCTOR OF PHILOSOPHY

in

CHEMICAL ENGINEERING

by

SNEHA MALHOTRA

DEPARTMENT OF CHEMICAL ENGINEERING
INDIAN INSTITUTE OF TECHNOLOGY ROORKEE
ROORKEE - 247667 (INDIA)
FEBRUARY, 2019

INDIAN INSTITUTE OF TECHNOLOGY ROORKEE
ROORKEE

CANDIDATE'S DECLARATION

I hereby certify that the work which is being presented in the thesis entitled **"CFD MODELLING AND EXPERIMENTAL INVESTIGATIONS OF AIR WATER FLOW THROUGH SERPENTINE CHANNEL"** in partial fulfilment of the requirements for the award of the Degree of Doctor of Philosophy and submitted in the Department of Chemical Engineering of the Indian Institute of Technology Roorkee, Roorkee is an authentic record of my own work carried out during a period from July, 2014 to February, 2019 under the supervision of Dr. Sumana Ghosh, Assistant Professor, Department of Chemical Engineering, Indian Institute of Technology Roorkee, Roorkee.

The matter presented in this thesis has not been submitted by me for the award of any other degree of this or any other Institution.

(SNEHA MALHOTRA)

This is to certify that the above statement made by the candidate is correct to the best of my knowledge.

(Sumana Ghosh)
Supervisor

Date: February 2019

Dedicated to

My Family

& My Friends

ACKNOWLEDGEMENT

I would like to express my gratitude to **Dr Sumana Ghosh** of Department of Chemical Engineering, IIT Roorkee for providing me the opportunity to work under her able guidance. It has been a great opportunity of learning under her supervision because of the depth of her knowledge in my field of research. Her guidance at every stage of the research from the problem definition to technical advice during experimentation and writing research papers has been very helpful.

I am also grateful to the members of the Departmental Research Committee, **Prof. Shishir Sinha** (HOD, Chemical Engineering), and **Dr. Amit Dhiman** of the Department of Chemical Engineering, IIT Roorkee and **Dr. Sudhakar Subudhi** of the Department of Mechanical Engineering, IIT Roorkee for their constructive criticism and helpful suggestions. I express my thankfulness to the Department of Chemical Engineering, IIT Roorkee for providing me all the required facilities. I also want to thank **Prof. Majumdar** (Ex-HOD, Chemical Engineering) and **Prof. B Prasad** (Chairman, DRC) for enabling a smoother research experience.

I convey my sincere thanks to **Prof. Sri Chand**, **Dr. Shabina Khanam** and **Dr. Prasenjit Mondal** of the Department of Chemical Engineering for giving me significant knowledge during the coursework. I have been able to derive invaluable inputs for my research work from their lectures. I also wish to express my sincere thanks to **Dr Arup Kumar Das** of Department of Mechanical Engineering, IIT Roorkee for his support during the research work.

I convey my thanks to my wonderful lab-mates **Raj**, **Ravi**, **Ranjana, Pooja and Liril** of Multiphase Flow Lab of Department of Chemical Engineering, IIT Roorkee for their valuable assistance during the course of my research work. I would also like to thank **Pramod, Chandan** and **Lokesh** of Two-Phase Flow Lab of Department of Mechanical Engineering, IIT Roorkee for their help. I am also thankful to **Mr. Dhiman** (Private Vendor) for his great help and sincere cooperation during my research work.

I will be forever grateful to my friends **Vatsal Sanjay, Rishabh Chaudhary, Yogesh Mirage and Uday Bhaskar** who have been with me constantly through the thick and thin, inspiring

and helping me throughout my time at IIT Roorkee. My hostel life would have been lonely and monotonous without my friends **Anusha, Chetna, Smita, Vibha and Anju**.

I also wish to thank the Department of Science and Technology, India for extending the financial support during my research period at Indian Institute of Technology, Roorkee. Finally, I would like to express my appreciation towards my brother **Aakash Malhotra** and my husband **Yuvraj Patil** for their constant encouragement, support and advice that helped me to achieve my goals.

Date: 8th February 2019

Sneha Malhotra

CONTENTS

LIST OF SYMBOLS

Nomenclature

A	Area of modified bottom surface [mm^2]
A_{act}	Active area of fuel cell [m^2]
A_i	Surface area of i^{th} slug [m^2]
A_n	Instantaneous area covered by slug [mm^2]
A_w	Area occupied by water [mm^2]
B_0	Boiling Number [-]
Bo	Bond number [-]
C	Constant [-]
C	Martinelli parameter [-]
C_0	Convection Number [-]
Ca_{LS}	Capillary Number Liquid Phase [-]
Co	Confinement number [-]
D	Diameter of channel [m]
D_H	Hydraulic diameter [m]
f	Single phase friction factor [-]
F	Faraday's Constant
F	Body force acting on the system [N]
f_m	Friction factor using mixture Reynolds number [-]
Fr_l	Froud Number [-]
F_s	Additional Surface Force [N]
G	Acceleration due to gravity [m/s^2]
h_l	Liquid heat transfer coefficient [W/m^2K]
I	Current Density (A/cm^2)
k_w	Bend loss coefficient for single-phase water flow [-]
L	Length of test section [m]

L_b	Length of the bend [m]
L_f	Length of a particular frame considered
M_G	Molar mass (g/mol)
N	Proposed constant [-]
P	Pressure in the flow field [N/m^2]
E	Parameter [-]
P_t	Time average pressure [Pa]
Q_G	Volumetric flow rate of gas [l/min]
R	Radius of curvature of the bend [m]
R	Radius [mm]
Re_{GS}	Reynolds number gas phase [-]
Re_{LS}	Reynolds number liquid phase [-]
Re_m	Mixture Reynolds number [-]
S	Mass source [kg/m^3s]
Su	Suratman number [-]
T1	Test section [1.65 mm]
T2	Test section [1 mm]
T3	Test section [0.65 mm]
U_g	Air velocity [m/s]
U_{GS}	Superficial gas velocity [m/s]
U_l	Water Velocity [m/s]
U_{LS}	Superficial liquid velocity [m/s]
U_m	Mixture velocity [m/s]
We_{GS}	Weber number gas phase [-]
We_{LS}	Weber number liquid phase [-]
X	Ratio of liquid only and gas only pressure drop [-]
x	Vapour quality [-]
ΔP	Pressure Drop [Pa]
$\Delta P(n)$	Normalised Pressure Drop [-]
ΔP_{Bend}	Pressure drop due to change in direction [Pa]

ΔP_f Frictional pressure drop in the straight portions [Pa]

ΔP_g Gravitational effect [Pa]

ΔP_{hydro} Pressure drop at return bend [Pa]

Greek Symbols

α Water coverage ratio [-]

γ Interfacial tension between air and water [kg/ms]

ε Error [%]

ρ Density of fluid [kg/m^3]

μ Viscosity [m^2/s]

$\Delta\rho$ Density difference [kg/m^3]

α_1 Volume fraction phase 1 [-]

α_2 Volume fraction phase 2 [-]

θ_f Forward contact angle [°]

$\phi_L{}^2$ Two-phase flow multiplier [-]

ϕ_{lo} Multiplier [-]

θ_r Rear contact angle [°]

μ_G Viscosity of air [m^2/s]

μ_L Viscosity of water [m^2/s]

μ_m Viscosity of mixture [m^2/s]

g Acceleration due to gravity [m/s^2]

α_t Time average water coverage ratio [-]

β_L Ex-situ liquid void fraction [-]

λ Laplace constant [-]

λ_s Stoichiometric ratio [-]

ρ_G Density of gas [kg/m^3]

ρ_L Density of liquid [kg/m^3]

ρ_m Density of mixture [kg/m^3]

ρ_W Density of water [kg/m^3]

σ	Surface tension [N/m]
σ_s	Standard Deviation [-]

LIST OF TABLES

LIST OF FIGURES

ABSTRACT

Multiphase flows are ubiquitous in nature. Two-phase flow can be considered as the simplest example of multiphase flow. It can be solid-liquid flow, liquid-liquid flow, gas-solid flow, and gas-liquid flow. Gas-liquid flows displays a lot of complexities due to presence of a deformable interface. These flows are influenced by channel shape, channel orientation and the compressibility of one of the phases. The air water flow in mini channels finds application in compact heat exchangers, microelectronic cooling systems, fuel cell etc. Water removal from gas flow channels in Proton Exchange Membrane Fuel Cell (PEMFC) constitute one of its major applications in miniature systems. Often serpentine shape of these channels is preferred industrially. Despite the increasing applications, the literature on gas-liquid flow is relatively scarce and the present work attempts to investigate the physics of flow through extensive experimentation and numerical analysis.

The experiments have been performed in a test section made up of acrylic plate. This plate has ten serpentine channels milled over and it is covered with another smooth acrylic plate at the top. There were three test sections with different hydraulic diameter. As orientation can play a significant role, hence experiments were performed to understand the effect of fluid flow rate and orientation. The test fluids used for entire range of experiments are zero air and deionised water. It is observed that as the hydraulic diameter of the channel reduced number of flow patterns observed decreased and the range of annular flow (most desirable flow pattern for PEMFC) increased. The vertical orientation in micro channel facilitated water removal from the channel owing to less maldistribution experienced by it. For micro channel vertical orientation exhibited four times of reduction in pressure drop in comparison to horizontal orientation of mini channel at similar combination of fluid flow rates.

As water removal from serpentine channel is of importance attempts have been made to simulate suspended and adhered drop of water as well as slug flow using commercial CFD software ANSYS FLUENT 18. The parameters that are varied are drop size, air velocity and surface characteristics of channel wall. The surface characteristics is

altered by subjecting bottom wall of the channel to a wettability gradient As the pressure drop and water coverage ratio governs the performance of the PEMFC, the effect of wettability gradient on these parameters are estimated. A gradual hydrophobic Gas Diffusion Layer (GDL) surface resulted in lesser pressure drop as well as water coverage for suspended drop. In presence of a wettability gradient, the adhered drop shows very less water coverage of channel bottom surface, however, takes longer time to remove than suspended drop. The presence of wettability gradient enhances the chance of formation of slug flow into a more desirable film flow. Application of hybrid bottom surface proved beneficial with respect to pressure fluctuation in slug flow regime

CHAPTER 1 INTRODUCTION AND LITERATURE REVIEW

Simultaneous flow of two immiscible fluids or a fluid and a granular solid is termed as two-phase flow. Though the examples of two-phase flow are profound in nature, daily life as well as in industrial systems, it is one of the complex branches of fluid dynamics. Flow of gas-liquid constitutes a typical branch of two-phase flow, which has wide number of applications in industries. Such applications cover large diameter pipes in power plant to micro sized conduits in micro fluidics. In all these applications, gas-liquid two-phase flow is very different as observed in macro dimension and micro dimension.

1.1 Applications of gas-liquid two-phase flow

Gas-liquid two-phase flow find wide applications in chemical, process and power plant. It involves in energy systems like heat exchangers (Malapure et al. 2007), cooling of high-powered electronic devices (Pramod and Sen 2018, Raj et al. 2018), fusion reactors (Qiu et al. 2017, Zhou et al. 2010, Jo et al. 2010), cavitation reactors (Gogate et al. 2001, Shivakumar and Pandit 2001), power plant refrigeration systems etc. Such applications are a part of non-adiabatic vapor-liquid flow, where a single liquid changes gradually forms its vapor under the application of heat. In both adiabatic and non-adiabatic gas-liquid flows, hydrodynamics influences the transport rate. Therefore, proper understanding of hydrodynamics, plays an important role in designing any system efficiently.

There is an increasing interest observed in last few decades for gas-liquid flows in miniature devices. However, complications arise when dimension of the geometry is reduced. In reduced dimensioned geometries surface forces become dominating. This gives rise to different interfacial distributions of two-phase flow in miniature geometries that are seldom observed in macro geometries. Hence, it becomes important to understand the role of gravitational, surface, viscous and inertia in order to analyze the system. Few dimensionless numbers are significant to analyze the phenomenon in small diameter channels are listed in Table 1.1.

Table 1.1: Dimensionless Numbers

Nomenclature	**Formula**
Reynolds number	$\frac{D_H U \rho}{\mu}$
Froude number	$\frac{\rho v^2}{\Delta \rho g d}$
Bond number	$\frac{D_H}{\sqrt{\sigma / (g \Delta \rho)}}$
Capillary number	$\frac{\mu U}{\sigma}$
Weber number	$\frac{U^2 D_H \rho}{\sigma}$
Suratman number	$\sigma \rho D_H / \mu^2$

As discussed by Serizawa et al. (2002), the classification for micro channel was proposed by Suo and Griffith dating back to 1964. According to this criterion, any channel is said to be a micro-channel if its confinement number

(Co = λ / D_H) is larger than 3.3. λ is the Laplace constant, estimated as

$$l = \sqrt{\frac{\sigma}{g(\rho_L - \rho_G)}} \qquad (1.1)$$

where σ is the surface tension, g is acceleration due to gravity and ρ_L and ρ_G being densities of liquid and gas respectively.

The classification was further elaborated by Kandlikar (2002) on the basis of hydraulic diameters (D_H)

- Macro channel D_H > 3 mm
- Mini-channels 0.2 mm < D_H < 3 mm
- Micro-channels 0.02 mm < D_H < 0.2 mm

Flow patterns like bubbly, dispersed, slug, stratified and annular were noticed in miniature devices. Few typical flow regimes are given in Figure 1.1. However, the characteristics of these flow distributions observed in miniature geometries are not exactly same as that of macro. On the other hand, some new flow distribution like slug-annular, ring and dispersed bubbly are also reported by researchers (Suo and Griffth 1964, Mishima and Hibiki 1996, Triplett et al.1999, Coleman and Garimella 1999). One of the earlier works in this area dating to 1996 is by Mishima and Hibiki. They observed characteristic differences of same flow pattern in mini tube and conventional tube. They noticed in case of bubbly flow in mini tubes, bubbles are not homogenously distributed in water phase, as observed in conventional tube. Instead, train of bubbles are flowing without coalesce along the tube axis. Characteristics of slug observe in their study also quite different from that in conventional pipes. In case of slug flow, they noted that long slugs are observed which are different for that observed in conventional one.

All these leads to the fact that the results of gas-liquid flow in macro cannot directly be applied to miniature geometries in a straightforward manner.

On the other hand, gas-liquid two-phase flows in mini-channels and micro-channels have received a great deal of attention due to their wide applicability in advanced and modern science applications like Micro-Electro-Mechanical Systems (MEMS), electronic cooling, chemical process engineering and fuel cells. One of the major applications of air-water two-phase flow, lies, in water drop removal from mini/micro channel of proton exchange membrane fuel cell (PEMFC). A schematic of the process is shown in Figure 1.2.

PEMFC is a suitable alternative to automobile devices based on fossil fuels due to its high efficiency, low operation temperature and near zero emissions.

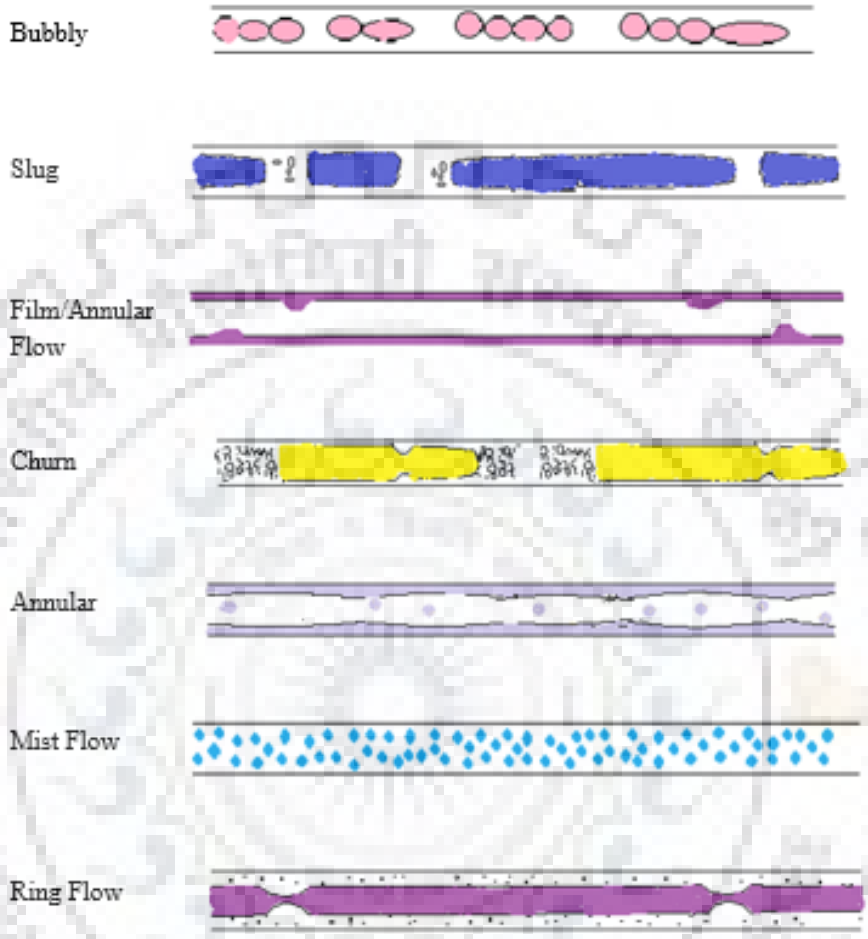

Figure 1.1: Schematics of typical flow regimes observed in miniature geometries

However, there are several issues which have been hindering its commercialization i.e. hydrogen storage, catalyst poisoning (Johnson et al. 2017) and water management etc. One of the prominent issues related to PEMFC is water management which has crucial role in smooth functioning of the PEMFC (Jiao and Zhou 2008, Quan et al. 2005). Excess water is generated due to electrochemical reactions and humidification of air in gas flow channels causing flooding and non-uniform distribution of reactant gases. Typical range of characteristic dimension of these gas flow channels lies within 1-2

mm. On the other hand, non-humidified air causes dehydration of the membrane. Both the situations are undesirable for operation of PEMFC (Anderson et al. 2012).

Therefore, understanding of air-water two-phase flow in mini channels, helps in designing of a gas flow channel which facilitates water removal. As a result, there has been an increased interest in the study of air-water two-phase flow dynamics in gas flow channels of PEMFC in last few decades. Several experimental studies are reported on air and water inside the gas flow channel as well as on water flooding in porous gas diffusion layer (GDL) adjacent to the channels.

Experimental studies are broadly classified as related to active fuel cell and ex-situ studies (Anderson et al. 2010a). Majority of the in-situ experimental studies reported the flow dynamics based on direct visualization in transparent fuel cell, neutron imaging and synchrotron X-ray imaging (Manke et al. 2007, Manke et al. 2008, Chen et al 2009, Hussaini et al. 2009, Banerjee and Kandlikar 2014, Bozorgnezhad et al. 2015, Iranzo et al. 2014, Iranzo et al. 2015). These studies are carried out to visualize water accumulation inside the cell. These studies give vital information about the cell performance with parameter like relative humidity of air, stoichiometric ratio etc.

However as pointed out by Lu et al. 2009, the two-phase flow dynamics in gas flow channels is less explored in case of an active fuel cell study. On the other hand, ex-situ experiments give more flexibility to study the two-phase flow dynamics in gas flow channels under similar operating conditions to active fuel cell.

The above discussion gives a glimpse of the applications of air-water two-phase flow specific in mini channels and provides the incentive for investigating such phenomena. Important investigations on air-water flow are reviewed in the following section.

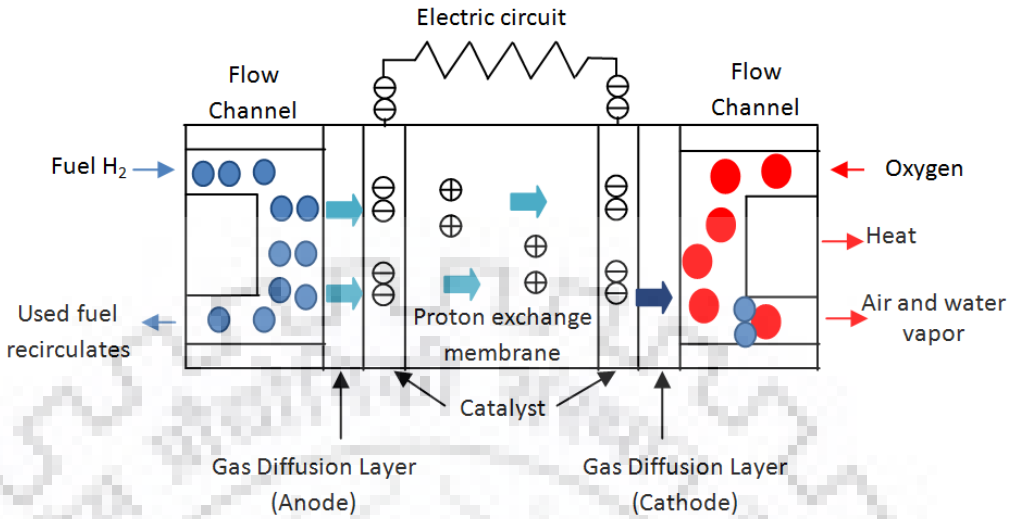

Figure1. 2: Schematic of PEMFC

Adiabatic gas-liquid flows are discussed first followed by non-adiabatic flows and numerical model of two-phase flow in miniature geometries.

1.2. Literature survey on gas liquid adiabatic flow through mini channels

Several studies have been reported on adiabatic gas-liquid flow through mini conduits. Studies are classified as flow through straight and interconnected conduits like parallel or serpentine etc. Flow through straight tube are discussed first flowed by interconnected tube.

1.2.1. Gas-liquid adiabatic flow through straight mini conduits

Several researchers have performed experiments on circular, triangular, rectangular, serpentine cross-section and diameters ranging from less than 1 mm to greater than 3 mm

Triplett et. al. (1999) performed experiments with air -water in a circular channel with 1.1 mm and 1.45 mm inner diameters. They also used semi-triangular (triangular with one corner smoothed) cross-section channel with hydraulic diameters 1.09 mm and 1.49 mm. Major flow pattern observed by them in all the geometries are bubbly, churn, slug,

slug-annular and annular. They noticed that no stratified flow pattern is observed despite the orientation of test section is horizontal.

Coleman and Garimella (1999) investigated the effect of tube diameter and shape on flow regime transitions for air-water system. They have reported flow regimes for four round tubes with inner diameter 5.5 mm, 2.60 mm, 1.75 mm and 1.30 mm. Stratified flow pattern is not noticed for tube diameter less than 5.5 mm. They also concluded that tube diameter played a significant role in flow regime transition. With reduction in tube diameter transition from slug to bubbly regimes occurred at larger liquid velocities.

Zhao and Bi (2001) studied the flow pattern of air-water system in a vertical miniature triangular channel with hydraulic diameter of 0.866 mm, 1.443 mm and 2.886 mm. They observed that flow patterns such as dispersed bubbly, slug, churn and annular occurred in the large size vertical circular tubes, were also observed in tubes having hydraulic diameter 1.443 mm and 2.886 mm. But they did not notice dispersed bubbly flow for tube of hydraulic diameter of 0.866 mm. They observed a single train of bubbles, which are ellipsoidal in shape for this smallest diameter channel. This is very similar with the observation made by Mishima and Hibiki (1996). They also reported shifting of slug to churn and churn to annular flow regime at higher gas velocities.

Akbar et. al. (2003) proposed the feasibility of Weber number based two-phase flow regime map for air-water system. They divide the entire flow region in to four zones. First is surface tension-dominated region which flow regimes like bubbly, plug and slug flow. Secondly, inertia-dominated zone 1, which encompasses annular and wavy-annular regimes. Third is inertia-dominated zone 2, including the dispersed flow regimes and finally transition zone.

English and Kandlikar (2006) investigated air-water two phase flow in a 321 mm long straight channel with 1 mm square cross section. The superficial velocity of air lied in the range of 3.19 m/s - 10.06 m/s and of water in the range of 0.0005 m/s - 0.022 m/s. The surfactants were added to the water which lowered the surface tension and the dominance of surface forces were analyzed. The surfactant used had almost no effect

on pressure drop but shifted the flow regime to annular and it was observed at higher velocities. The stratified regime was not observed for surfactant solutions. They proposed a pressure drop correlation for horizontally placed channel for laminar-laminar two-phase flow.

Ide et. al. (2007) performed experiments with air-water system in capillary tubes with inner diameter of 1 mm, 2.4 mm, 4.9 mm. They have also used rectangular channels with the aspect ratio of 1 to 9. Flow regimes, pressure drop and void fraction are measured for vertical upward, horizontal and vertical downward flow. They concluded that surface forces become predominant if the tube diameter is less than 5 mm. Effect of channel orientation also found to be insignificant in case of round circular tubes. However, in case of non-circular tubes, at higher gas velocities, horizontal orientation has higher hold up during annular distribution.

Yue et. al. (2008) analysed the two-phase flow pattern and pressure drop characteristics during the absorption of CO_2 into water in three horizontal microchannel contactors. It comprised of a Y-type rectangular micro channels having hydraulic diameters of 0.667, 0.4 and 0.2200 mm, respectively. Taylor bubble formation process in micro channels was found to be in the squeezing regime at lower superficial liquid velocities (Capillary number ranging from 0.0019 to 0.029) while the transition to the dripping regime was observed at the highest superficial liquid velocity of 1.0 m/s.

Venkatesan et. al. (2010) studied the effect of tube diameter on two-phase flow patterns of air-water system in circular tubes with inner diameters of 0.6, 1.2, 1.7, 2.6, and 3.4 mm. They also found that stratified flow was not observed for tube diameters less than 2 mm. They did not notice annular flow for smallest diameter tube. They concluded that buoyancy become important for tubes of diameter 2.6 and 3 mm.

Saisorn and Wongwises (2010) investigated the flow characteristics of air-water system in three circular micro channel having inner diameter of 0.53, 0.22 and 0.15 mm respectively. They found seven different flow patterns including slug flow, throat-annular flow, churn flow, annular–rivulet flow, annular flow, liquid-alone flow and

serpentine-like gas core flow. They estimated in-situ void fraction from image analysis and proposed a relationship with inlet void fraction. However, this relationship does not hold good for the smallest diameter pipe they tested (0,15 mm).

Zhao et. al. (2013) studied the hydrodynamics of nitrogen-deionized water system in a T-junction micro-channel of hydraulic diameter of 0.4 mm at elevated pressure. The range of operating pressure considered for their study was 0.1-5.0 MPa. Different flow configurations i.e., bubbly flow, slug flow, unstable slug flow, parallel flow, slug-annular flow, annular flow, and churn flow are observed.

Barreto et. al. (2015) studied frictional pressure drop and void fraction in circular channel of 1.2 mm inner diameter for air-water system. The flow pattern observed was bubbly, slug, churn, annular and transition. They concluded that for the prediction of pressure drop in case of annular flows with superficial gas velocities of over 18.6 m/s can be well predicted using the correlations proposed by Mishima and Hibiki (1996). Traditional correlation used for large pipe presented the best performance for bubbly, slug, churn and annular flow patterns with superficial gas velocities below 14.5 m/s. They concluded that pressure drop correlations developed for refrigerant are not suitable for air-water system.

Coeuriot et al. (2015) studied air-water flow in straight channels of 225 mm long, 1 mm width and of different depths (0.4, 0.7 and 1 mm). They investigate the role of contact angle on flow distribution. Three different static contact angles 75°, 90°and 105° were studied. They noticed that, the hydrophilic channel posed lesser pressure drop as it favored film formation while the hydrophobic channel gave rise to huge droplets. They had also observed that the pressure drop was independent of the depth except at low flow rates.

Timung et al. (2015) studied oil-water flow through a T-shaped microchannel. They observed the interfacial tension and viscosity hugely affects flow patterns and pressure drop in the microchannel. A gradual reduction in interfacial tension caused the slugs to transform into small plugs and plugs broke into tiny droplets.

Flipo (2016) demonstrated the effects of surface wettability on the two-phase flow in channels for PEMFC. They performed the experiments using two different channels made up off hydrophilic PMMA and hydrophobic PDMS. The dimensions of the channel tested were 1 mm× 1 mm× 50 mm and the air inlet and water inlet were separated by a distance of 15 mm. The air velocity varied in the range of 0.27 to 4.7 m/s and that of water lies in the range of 0.00875 m/s to 1 m/s. They observed that the slug formation time was independent of the air flow rate. The liquid films formed spread all along the channel that made the two-phase flow unstable.

Some of the important literature and ranges of operating condition in mini straight conduits is given in Table 1.2.

Table 1.2: Gas Liquid flow through straight mini channels

Authors	**Geometry / Operating conditions**	**Flow Patterns observed**
Mishima and Hibiki (1996)	Round tubes D_H =1 - 4 mm Air velocity (0.079 - 38.9 m/s) Water velocity (0.0116 - 1.7 m/s)	Bubbly, slug, annular, churn
Triplett et al. (1999)	Round tubes D_H =1.1 mm and 1.45 mm Triangular cross-section D_H =1.09 mm and 1.49 mm 0.02-8 m/s, gas and liquid superficial velocities	Bubbly, churn, slug, slug-annular and annular mist flow
Venkatesan et al. (1999)	Round tubes D_H = 0.6 - 3.4 mm Air velocity (0.15 – 31 m/s) Water velocity (0.01 - 1.84 m/s)	Bubbly, dispersed bubbly, slug, slug-annular, wavy annular, stratified, churn

Coleman and Garimella (1999)	Round tubes D_H = 1.3-5.5 mm Rrectangular Channel D_H = 5.36 mm Air velocity (0.1 – 100 m/s) Liquid velocity (0.01 – 10 m/s)	Bubble, dispersed, plug and slug, wavy- annular, annular
Zhao & Bi (2001)	Triangular Channels D_H = 0.866-2.866 mm Air velocity (0.1 – 100 m/s) Liquid velocity (0.08 – 6 m/s)	Bubbly, slug, churn, annular
Ide et al. (2007)	Round tubes D_H = 1 - 4.9 mm Flat Channels Air velocity (0.01 – 10 m/s) Liquid velocity (0.01 – 1 m/s)	Bubbly, slug, stratified, annular, wavy and dispersed bubble
Saisorn and Wongwises (2010)	Round tubes D_H = (0.15 mm-0.53 mm) Air velocity (0.37 - 42.36 m/s) Liquid velocity (0.005 - 3.04 m/s)	Bubbly flow, slug flow, churn flow
Yue et al .(2008)	Rectangular Channel D_H = 0.22-0.66 mm CO_2 velocity = (0.16 – 31 m/s) Water velocity = (0.02 – 1 m/s)	Bubbly, slug, slug-annular, churn, annular
Wang et al. (2012)	Rectangular Channel (150× 4× 4 mm) Air velocity (4.2 m/s)	Wetted channel, Spread film, Elongated drop, Spherical drop

Zhao et al. (2013)	Rectangular Channel D_H = 0.22 - 0.66 mm N_2 velocity (0.01 - 100 m/s) Water velocity (0.01 – 10 m/s)	Bubbly, slug, unstable-slug, parallel, slug-annular, annular, and churn flow
Barreto et al. (2015)	Circular Channel D_H = 1.2 mm Air velocity (0.1 - 34.8 m/s) Liquid velocity (0.1 - 3.5 m/s)	Bubbly, slug, churn and annular flow
Flipo et al. (2016)	Square Channel D_H = 1 mm Air velocity (0.27 - 4.7 m/s) Water velocity (0.00875 - 1 m/s)	Slug flow, Liquid film

1.2.2. Air water flow through interconnected conduits

In this section, gas-liquid flow through interconnected sections like parallel or serpentine channels are described. As pointed out by Li et al. (2008) this type of channels are preferred in industry due to their reliability and durability.

Kirpalani et. al. (2008) investigated air-water system in a straight channel as well as serpentine channels. They considered tubes of 1 mm and 3 mm inner diameter for their study. Slug flow has been observed only for 1 mm tubes. On the other hand, flow patterns in 3 mm straight tube are in agreement with flow pattern map of Taitel and Duckler. However, they also noticed that presence of curves in serpentine channel produces slug breakage resulting a secondary flow.

Zhang et al. (2008) studied the flow regime and pressure drop of air and water in a Y branched parallel channel of dimension 1.59 mm ×1.59 mm and length 300 mm in horizontal orientation. The superficial velocity lies in the range of 0 to 0.03 m/s for

liquid and 0 to 10m/s for gas. They observed slug, stratified and stagnant liquid flow regimes. They have also noticed flow maldistribution at lower gas velocities which tend to disappear at larger gas superficial velocities.

Later **Zhang et al. (2009)** studied the effect of channel orientation on the distribution of air-water inside a parallel square mini channel of 1.59 mm and length 300 mm. The superficial gas velocity varied in the range of 0-7m/s. The major flow pattern observed were stratified, annular and slug. The angle of inclination is varied from + 18^0 to - 12^0.They have noted that with increase in channel inclination, higher gas flow rates are required to maintain a uniform distribution.

Kandilkar et al. (2009) investigated air-water hydrodynamics in parallel gas channels of dimension 0.4 mm × 0.7 mm × 183 mm. They proposed a methodology to measure instantaneous flow rate of individual channels of the parallel flow field. The method provided a way to predict and find individual channel obstructions in real time.

Later **Lu et al. (2009)** performed experiments on the same geometry. The superficial air velocity varied in the range of 0-8.9 m/s. Authors observed annular/film, slug and mist flow regimes. They noticed that slug is the dominating flow pattern at low air flow rate and leads to maldistribution of flow in the channels. At higher air flow rates, the flow distribution become annular/film flow in which reduces the maldistribution. At extremely high flow rates, mist flow was observed that ensured minimized variation in overall pressure drop and flow rate.

Leclerc et. al. (2010) presented different T-junction geometries with hydraulic diameter 0.3 mm and their impact on bubble and slug formations. They have used nitrogen-water as test fluids. They observed that effect of inlet geometry on flow for a given set of fluid flow rates.

Anderson et al. (2010b) studied two-phase flow and pressure drop hysteresis in four parallel rectangular channels with a cross-section of 1 mm× 1 mm and a length of 30

cm. They have reported pressure drop hysteresis for stoichiometry of 1–4 and it was eliminated at a stoichiometry of 5.

Choi et al. (2011) studied two 60 mm long hydrophilic and hydrophobic channel. The hydraulic diameter for hydrophobic and hydrophilic channel is 490 µm and 507 µm. The superficial velocity of Nitrogen varied in the range of 0.066 m/s -34.1 m/s and water velocity in the range of 0.19-0.46 m/s. Authors noticed that, surface wettability influences flow pattern. The dominant flow pattern observed for hydrophobic channel were stratified and wavy stratified. While bubbly and ring flow were prominent flow patterns in hydrophilic channel. Pressure drop in hydrophilic channel was higher than hydrophobic channel. They proposed pressure drop correlation based on Capillary number.

Donaldson et. al. (2011) performed experiments with air and water in straight and serpentine mini channels with 1 mm inner diameter. They considered channels with two different radius of curvature 3 mm and 6 mm. Serpentine geometry observed to play and important role in both flow pattern as well as pressure drop. It causes change in bubble dynamics by bubble coalescence and separation of the bubble film from the channel wall. They identified different flow regimes namely bubbly flow; slug/annular flow; and plug/unstable plug flow with minimal topological changes; deformation, extrusion and bag breakup; and continuous breakup of small and large bubbles. They also proposed transition criteria based on Weber number and length of curved channel between these regimes.

Lu et al. (2011) studied the effect channel surface wettability, geometry and orientation on two phase flow in parallel channels of dimension 0.4 mm × 0.7 mm × 183 mm. the superficial velocity of liquid varied in the range of 0.00015 m/s to 0.0015 m/s and air velocity varied in the range of 0.5 m/s to 29.5 m/s. The major flow pattern observed were slug and film. They considered a hydrophilic surface of contact angle 11° and hydrophobic surface of contact angle 116°. It was concluded, hydrophilically coated channels exhibit a uniform water distribution which is less prone to maldistribution.

The cross section of geometry also influenced the pressure drop as sinusoidal geometry favored the formation of film flow. Horizontal orientation found to be more susceptible to slug formation while vertical orientation is found to be stable.

Steinbrenner et al. (2011) performed experiments on 0.5 mm× 0.5 mm× 600 mm multiple rectangular parallel channel. One side of the channel wall is comprised of porous carbon paper. Different types of flow patterns such as slug, plug and stratified were noticed. The length and number of channels impacted the overall pressure drop. The drop in the pressure was observed as number of channels had increased. Authors noted that the corners of the channel made the evacuation of water. They found that larger pressure drop in long channel favored removal of water.

Zhang et al. (2011) performed experiments to study the two-phase flow pattern and pressure drop in parallel square mini channel of 1.59 mm and length 300 mm bounded by a porous media. The superficial gas velocity is in the range of 0-10 m/s and water velocity is in the range of 0-0.05 m/s. The major flow pattern observed were slug and stratified flow. In order to predict the pressure drop two correlations were provided by modifying Lockhardt–Martinelli model. They have proposed criterion for onset of slug regime from instability of stratified flow**.**

Grim et al. (2012) investigated the effect of GDL on two-phase flow dynamics in the same geometry as Lu et al. (2009). The superficial velocities of fluids were also same. The three predominant observed flow patterns were slug, film and mist. They focused majorly on the changes that are induced when the method of water injection is altered. In their study, water is injected from the bottom of GDL to give uniform distribution of water throughout the channel. Authors noticed that due to change in introduction of water, flow regime transition was prominent along the length of the channel as would happen in an actual fuel cell.

Chinnov et al. (2015) performed experiments with air-water in a horizontal channel of a rectangular cross-section with the height of 0.1–0.5 mm and width of 9–40 mm. the superficial gas velocity varied in the range of 0.1-100 m/s and of liquid in the range of

0.01-10 m/s. Authors noticed that, various flow pattern such as churn, annular, bubbly, stratified and drop. They observed that an increase in the channel width causes the expansion of the zones of stratified and churn flows. As the height of horizontal channels reduced the churn flow zone increased and the zones of the annular, stratified and jet flows decreased. They observed the height of the channel plays a decisive role and it needed more studies as opposite to combined aspect ratio.

Iranzo et al. (2016) performed experiments in a serpentine channel. They investigate the effect of channel orientation on flow distribution. They noticed that, the vertical orientation of channel with an upward gas flows were more prone to water clogging as the gravity made it difficult to remove the water drops. Their findings indicated that in the horizontal orientation, gravity is orthogonal to gas flow and thus the water blockage is less.

Zhou et al. (2017) performed experimental and numerical study to investigate the effect of channel wall wettability and roughness on flow distribution. Authors have used a serpentine channel of length 50 mm and a converging Y shaped inlet of length 10 mm. The channel has a rectangular cross section of 0.8 mm× 0.1 mm. The gas velocity varied in the range of 0.8 to 1.39 m/s and liquid velocity varied in the range of 0.03 to 0.694 m/s. The major flow pattern observed were bubbly flow, slug flow and wall flow. They have observed flow regimes and their transition boundaries shifted depending on wall contact angle. Authors noted that with an increase in contact angle slug flow regime expands.

Zhang et al. (2018) performed experiment to study absorption of carbon dioxide in water in serpentine micro channel. They observed that length of slug and their velocity changes along the length of the channel. Authors have also reported a critical point for mass transfer coefficient.

A summary of literature is provided in table 1.3 for interconnected conduits

Table 1.3: Summary of flow patterns of gas-liquid flow in interconnected channels

Author & Year	**Geometry & Dimensions**	**Flow pattern**	**U_{GS} (m/s)/ Flow rate**	**U_{LS} (m/s)/ Flow rate**
Zhang et al. (2008)	Y branched parallel channel, 1.59 mm	Slug, Stratified and Stagnant liquid	0 – 10 m/s.	0 - 0.03 m/s
Zhang et al. (2009)	Parallel square, 1.59 mm	Stratified, Annular and Slug.	0 – 7 m/s	Stoichiometric ratio of 0 – 50
Lu et al. (2009)	Parallel gas channels, 0.4 mm × 0.7 mm	Static Water Holdup, Annular/Film, Slug, Mist	0 - 8.9 m/s	Stoichiometric ratio of 1 – 45
Kirpalani et al. (2008)	C shaped geometry (1 - 3 mm)	Dispersed bubble, plug, slug, annular	0.01 – 100 m/s	0.01 – 10 m/s
Leclerc et al. (2010)	Square Serpentine Channel D_H = 0.3 mm	Taylor bubble and slug flow (bubble and slug length correlations)	0.03 -0.07 m/s	0.0018 - 0.037 m/s
Lu et al. (2011)	Parallel gas channels, 0.4 mm × 0.7 mm × 183 mm	Slug and Film	0.5 - 29.5 m/s	0.00015 - 0.0015 m/s
Steinbrenner et al. (2011)	Multiple parallel rectangular serpentine channel 0.5 mm × 0.5 mm × 60 cm	Slug, Plug and Stratified	Stoichiometric ratio of 1 - 4	33.6 - 134.6 µl/min

Zhang et al. (2011)	Parallel square mini channel 1.59 mm	Slug and Stratified	0 – 10 m/s	0 - 0.05 m/s.
Grim et al. (2012)	Parallel gas channels, 0.4 mm × 0.7 mm × 183 mm	Slug, Film and Mist.	0 - 8.9 m/s	Stoichiometric ratio of 1 - 45
Chinnov et al. (2015)	Rectangular cross-section, Height = 100 – 500 µm Width = 9 – 40 mm.	Churn, Annular, Bubbly, Stratified and Drop	0.1 -100 m/s	0.01 – 10 m/s
Zhou et al. (2017)	Serpentine channel Length = 50 mm Rectangular cross section = 800 µm × 100 µm	Bubbly Slug and Wall	0.8 - 1.39 m/s	0.03 - 0.694 m/s.

1.3. Two-phase single component flow with phase change in miniature geometries

Single component two-phase flow differs from gas-liquid or liquid-liquid two-phase flow from the fact that in the former case a liquid-vapour mixture is formed in the test section from a single liquid. With transfer of heat, single phase flow changes to two – phase inside the conduit. As volume fraction changes along the length of the conduit therefore, prediction of pressure drop become complicated. Heat transfer plays a key role in the processes involving boiling and condensation and in reactions. They are also having the application in heat exchangers, evaporators, condensers, spry cooling towers, dryers, refrigerators, electronic cooling systems and direct contact heat exchangers.

Lin et al. (1991) performed experiments in two circular conduits of i.d. 0.66 mm and 1.17 mm. They used R-12 as test fluid. The range of mass-flux investigated was in the

range of 1440 - 5090 kg/m^{2}s. They measured the single and two-phase frictional pressure drop and proposed an empirical correlation. Authors suggested a modification in expression of two-phase viscosity by incorporating the vapor quality. With this modification, they had predicted the experimental data within ± 15%. Range of quality for which this modification is proposed is 0 - 0.25.

Later, **Yang and Webbt (1996)** examined the pressure drop in two miniature tubes of rectangular cross-section. Hydraulic diameter of the two test sections were 1.56 mm and 2.64 mm. They have also used R-12 as the test fluid. Authors noted that separated flow model was not able to predict their experimental data.

Yan and Lin (1999) performed experiment with R-134a in capillary tube of i.d. 2 mm. They investigate evaporation heat transfer by imposing a heat flux of 5 to 20 Kw. Authors varied mass flux from 50 to 200 kg/m^{2}s. They reported highest heat transfer coefficient for higher heat fluxes. Authors also presented a correlation for heat transfer coefficient by using the experimental data as a function of Convection number (C_o), Boiling number (B_o) and Froude number (Fr_l)

Tran et al. (2000) investigate two-phase pressure drop using R-134a, R-12 and R-113. They used two circular tubes of inner diameter of 2.46 mm and 2.92 mm. They also proposed a correlation for pressure drop in case of boiling by modifying the Chisholm parameter and found that it is well fitted with experimental data.

Later **Zhang and Webb (2001)** performed experiments in a capillary tube of diameter 2.13 mm. They have used three different refrigerant R-134A, R-22 & R-404A as their test fluid. They propose a two-phase flow multiplier for refrigerant which is a function of vapor quality, liquid and vapor density and viscosity ratio as well as Weber and Froude number.

Garimella et al. (2002) studied experimentally the flow regimes in a horizontal miniature channel with hydraulic diameter 0.5 mm to 4.91 mm. They observed slug, film/bubble region and transition region during condensation of refrigerant R134a.

Authors developed a model based on slug Reynolds number. They identified three regions for the pressure loss due to mixing and reported that 53% accounts by slug flow, 12% by film/bubble region and 35% by the transition region.

Yu and France (2002) performed experiments with boiling water and ethylene glycol in a tube of i.d. 2.98 mm. They varied the mass flux in the range of 50 to 200 kg/m^2 s. and proposed a correlation for heat transfer coefficient.

Lee and Mudawar (2005) investigate dependency of flow regime and quality using R- 134a in a miniature tube. They noticed that, mechanism of heat transfer depends on quality of a particular flow pattern. Authors observed, bubbly regime at low quality. Also, it followed nucleate boiling condition. On the other hand, for higher heat fluxes, the flow may be either medium or high quality. They reported that, at this condition, the it follows annular film evaporation. Therefore, they proposed correlation of heat transfer for different ranges of quality. These correlations predicted well the data for R134a along with data of water.

Wook and Kim (2006) performed experiments with R134a in three miniature tubes of different geometries. They analyzed two-phase frictional pressure drop. Authors proposed a correlation by modifying Chisholm parameter and reported that parameters developed take care of surface tension and channel diameter.

Megahed & Hassan (2009) investigated hydrodynamics and heat transfer characteristics in a mini channel of hydraulic diameter of 0.27 mm. They used FC-72 as their test fluid. They varied the mass flux in the range 341 to 531 kg/m^{2}s and heat flux of 60.4 to130.6 kW/m^2. Author noticed bubbly, slug and annular as the dominant flow regimes. Also, they developed a correlation for pressure drop for five different refrigerants.

Pamitran et al.(2010) performed experiments in three miniature tubes of diameter 0.5 mm, 1.5 mm and 3 mm. Propane, ammonia and carbon di oxide are used as test fluid.

They varied the mass flux 50-600 kg/m^{2}s. They have modified the Chisholm's parameter as a function of the mixture Weber number and Reynolds number.

Zhang et al. (2010) establish neural network technique for Chisholm's parameter as a function of Laplace length. Authors reported that technique work well for adiabatic gas-liquid and liquid vapor flow and the Dukler's correlation based homogenous model and correlations proposed by Mishima and Hibiki (1996).

Soupremanien et al. (2011) performed experiments in two rectangular channels of hydraulic diameter 1.4 mm and aspect ratio of 1.43 for one and 0.43. Forane 365 HX is used as test fluid. They varied the mass flux in the range of 200 to 400 kg/m^{2}s and heat flux 25-62 kW/m^2. Authors noticed that for low heat fluxes, channel with higher aspect ratio has higher values of heat transfer coefficient. On the other hand, for high heat fluxes, lower aspect ratio channel has higher values of heat transfer coefficient.

Charnay et al. (2014) examined the flow regime and its effect on differential pressure drop in flow boiling of R-245fa in a mini tube of 3 mm diameter. They varied the mass flux in the range of 100 to 1500 kg/m^{2}s and heat flux 10-50 kW/m^2 They observed four different types of flow regimes. Authors also reported that high saturation temperature increases the possibility of stratified character of the flow.

Falsetti et al. (2017) studied pressure drop, heat transfer and two-phase operational map for flow boiling of R236fa in a micro pin evaporator with a diameter of 50 µm. The mass flux varied in the range of 500 kg m^2/s to 2500 kg m^2/s and heat flux ranged from 20W/cm^{2}to 48W/cm^2. Four flow regimes were identified, namely, jet-flow, single phase followed by two-phase flow, unstable two-phase flow and fully stable two-phase flow. Heat transfer coefficient varies widely with the flow conditions (mass flux and heat flux), indicating the dependence on two-phase flow pattern development.

Zhou et al. (2017) studied pressure drop, local heat transfer coefficient and flow pattern in a 30 mm long microchannel with deionized water as working fluid. The mass fluxes varied in the range of 120–360 kg/m^{2}s and the inlet vapor qualities varied from 0.03 to

0.1. Most of the experimental data points lied in the annular flow regime and a local dry out phenomenon was observed in hydrophilic surface. Heat transfer deterioration was observed on the hydrophilic surface with greater inlet vapor quality, while superhydrophilic surface exhibited a constant behaviour for the same parameter.

1.4. Computational simulation of gas-liquid flow in miniature geometries

Numerical algorithm is very helpful for analysing the hydrodynamics, heat transfer and mass transfer in miniature reactor because they provide an insight of the phenomena. They provide a virtual pilot plant where one can do the experiments and can solve many difficult problems and further able to correlate and validate with the experimental results. Several studies have been dedicated to numerical analysis of air-water flow. In this section the studies related to numerical modeling of air-water flow in mini conduits are discussed.

Harries et. al. (2003) developed a model using CFD tools and studied the characteristics of the segmented flow in a micro channel reactor. They validated the results with the experimental results of several other authors. They found that developed model was well predicting the flow characteristics and mass transfer of the segmented flow.

Quan et al. (2005) studied the behavior of air–water flow inside a serpentine channel for PEMFC using volume-of-fluid (VOF) model. The computational domain was a 40 mm long U-bend with round tip and rectangular cross section of 1 mm× 1 mm. The air velocity was kept constant at 10m/s and water volume varied in the range of 0.035 mm^3 to 16.10 mm^3. The bend area of the channel had significant effects on the flow field and flooding occurred in the “after-bend” section of the channel. For large water volume it was found that after-bend lowered the fuel cell performance by blocking the reactant supply to the reaction sites thus adversely affecting the transport of reactant inside the gas flow channel.

Qian and Lawal (2006) numerically analysed the effect of various parameters on the slug length of gas and liquid in micro channel reactors. They observed that the gas slug length increases with increase in superficial gas velocity and decrease in superficial liquid velocity. On the other hand, liquid slug length increases with increase of superficial liquid velocity and decrease of superficial gas velocity. They also found that wider channels have longer slug length at the same superficial gas and liquid velocities. The reason is attributed to the fact that, it was determined by phase hold-up. Also, surface tension and wall adhesion moderately impact the slug lengths.

Cai et al. (2006) studied the movement of water inside in a straight rectangular channel and the effect of hydrophobic/ hydrophilic wall characteristics on its behavior. The straight channel is 20 mm long and has a cross-section of 1 mm× 1 mm. The water droplet of 0.033m^3 and water film of volume 1 mm^3 was attached to the surface of MEA and the air velocity was kept constant at 5m/s. As the material properties exhibited a great influence on water distribution the hydrophobic channels favored the water removal. The water removal was faster when MEA had hydrophobic surface and the side walls had a hydrophilic surface

Jiao & Zhou (2007) numerically simulated air water flow in a serpentine channel of length 15 mm and minimum cross section of 1 mm× 1 mm. The water volume of 1.04 mm^3 was placed on the membranes and air velocity of 10m/sec was applied at the upper section. The pore size of the GDL was varied between 10-30 μm and two shapes namely cuboidal and trapezoidal were considered. The secondary flow around the downstream of the corner strongly influences the water removal. The water removal was maximized with the trapezium porous holes as they had minimum area facing the gas flow channel.

Jiao & Zhou (2008) studied liquid water transport in a serpentine channel and reported the effect of wettability of electrode on the flow patterns. The computational domain was 15 mm long with a cross section of 1 mm× 1 mm. The air velocity was kept constant at 10m/s and water film of volume 1.04 mm^3 and thickness of 0.03 mm was placed on the catalyst layer. They varied the contact angle of GDL and catalyst layer from

hydrophilic to hydrophobic (contact angle of 45° and 135°). Hydrophobic catalyst layer and GDL was found to be beneficial for water breakage provided the hydrophobicity of catalyst layer is high that allows water movement in one direction.

Onea et. al. (2008) performed numerical study of effect of unit cell length, liquid slug length and aspect ratio on mass transfer in square and rectangular mini channel. They observed that short unit cell provides more efficient mass transfer. Authors noticed that rectangular channel with large aspect ratio was superior than the square channel. They also concluded that shorter liquid slug length provides higher mass transfer than longer slug length.

Carton et al (2012) studied water droplet movement and slug formation in mini channels of PEM fuel cell. Their computational domain is 3D double serpentine channel and the dimensions are 20 mm× 1 mm× 1 mm. The radius of water droplet varies from 0.3 mm to 0.9 mm and air velocity is kept constant at 1 m/s. It was observed that the interaction of droplets in the bend region led to slug formation that caused velocity fluctuations and high pressure in PEM fuel cell. The increase in flow rate along with introduction of bends and steeps, reduced the slug formation.

Pant et al. (2012) proposed a model to measure GDL permeability and diffusivity. They have shown that Darcy's law is not predicting the pressure drop well because of Knudsen diffusivity. Hence porous structure of GDL must be accounted for the simulation.

Chen et al (2013) performed numerical simulations in order to investigate the effect of GDL wettability, air velocity and microstructure on drop dynamics inside a mini channel. The straight channel has a dimension of 340 mm× 300 mm× 1200 mm with a square pore of side 60 μm. The air velocity was varied in the range of 5 m/s to 15 m/s and inlet water velocity was fixed at 0.1 m/s. The microstructure of GDL seemed to affect the drop dynamics.

Qin et al (2013) studied water dynamics and transport in a straight channel of length 50 mm and of cross section of 1 mm× 1 mm. The droplet diameter was fixed at 0.6 mm and the air inlet velocity was kept constant at 6m/sec. A hydrophilic needle of contact angle 10° was inserted in the channel at a distance of 1 mm from channel inlet. The diameter of the needle was varied in the range of 0.04 to 0.2 mm and the length of the needle was in the range of 0.4 mm to 1.2 mm. The capillary force exerted by the needle changed the direction of droplet away from MEA wall and pushed it towards the bottom wall of the channel. The optimum diameter for the needle was fixed at 0.1 mm and length at 0.7 mm. The increase in needle length facilitated the water removal from the electrode but also increased the pressure drop by 12% if three needles were used**.**

Mansour et. al. (2014) analysed the third direction effect on the slug length, axial velocity and void fraction in gas- liquid two phase flows in a microchannel. They carried out the numerical studied on 2-D and 3-D simulation using VOF. They observed that bubble slug length increases with the increasing of the inlet bubble volume flux and axial velocity for 3-D simulation was reported higher than 2-D simulation. They also found that void fraction for the 3-D simulations were close to the homogeneous flow line.

Song et al (2014) studied the droplet dynamics in a serpentine channel of length 5 mm and rectangular cross sectional of 1.1 mm× 0.6 mm. The droplet emerged through four adjacent pores having a size of 50 µm× 50 µm. The air velocity was kept constant at 2 m/s and water velocity at 0.2 m/s. The influence of contact angle was quantified in terms of liquid water saturation and water coverage ratio. They noticed that a hydrophilic channel with hydrophobic bend section, showed better results in terms of water removal in comparison with a homogenous hydrophilic and homogenous hydrophobic channel.

Ferreira et al (2015) studied droplet dynamics in a straight channel of length 5 mm and a cross section of 1 mm× 1 mm. The diameter of droplet was fixed at 600 µm and hydrogen velocity was varied in the range of 1 to 2.5 m/sec. The contact angle of GDL

was varied in the range of 45° to 160°. Hydrophilic channel favored film formation while hydrophobic channel resulted into more spherical drops. An increase in operating temperature and contact angle facilitated the water removal. The rise in hydrogen velocity positively impacted the water removal but adversely effected the pressure profile of the channel.

Jo & Kim (2015) studied the emergence of water droplet from a micro pore of 50 µm. The channel is bent at right angles with a 250 mm× 250 mm square cross section and 1000 mm× 1000 mm length in the x and z coordinate. The air velocity was kept constant at 10 m/s and water injection velocity at 1m/s to have an optimum computational time. The static contact angle for GDL was fixed at 140° and for top and side walls as 45°. The GDL contact angle plays an important role in determining the flow pattern and interaction of air and water in the channel. By decreasing the contact angle of the GDL water droplets from the corner pore were pushed away to the side walls. On the other hand, by increasing the contact angle of side and top wall water coverage in the GDL increased. The air velocity also impacted the water fraction as by increasing the velocity a drop is experienced in the water coverage.

Engelbrecht et. al. (2016) studied numerically the reactor performance for CO_2 methanation reaction in a rectangular micro channel reactor. They observed that at 10 bar pressures and 375 ^{0}C temperature and a space velocity of 32.6 $Lg_{cat}^{-1}h^{-1}$96.8% CO_2 conversion and 97.5% Yield of CH_4 was reported however, higher flow rate was desirable. They also pointed out that higher temperature and higher-pressure conditions were yields favourable flow characteristics and concentration profiles.

Kim et al. (2018) studied air water two phase flow in a straight channel with trapezoidal and rectangular inlet. The dimensions of the channel are 100 µm× 700 µm× 4 mm. The air velocity is varied in the range of 1-5 m/s and water velocity is fixed at 0.1m/s. The contact angle of GDL is fixed at 130° and of top and side walls are varied in the range of 60° &130°. The trapezoidal cross section displayed the best water removal

characteristics. Water slugs moved faster and were smaller in sizes as the air inlet velocity increased.

Qin et al. (2018) studied droplet dynamics in a straight channel with dimension of 1 mm× 1 mm× 300 mm and analysed the impact of dynamic wettability on droplet deformation. The droplet diameter was fixed at 0.6 mm and air velocity is fixed at 6m/s. The static contact angle is fixed at 140° and sliding angle 10° to 50°.They observed that the smaller sliding angle facilitates the water removal from the channel. As the pressure drop is hugely dependent on oscillation of droplet, the pressure drop for 10° sliding angle was found to be the least.

1.5. Lacunae in literature

A review of above literature reveals that, different parameters which affect flow distribution in case of gas-liquid flow in mini channels have been studied. However, majority of the studies are performed either in straight or parallel channels. But, serpentine gas flow channels are most commonly used in industry. Very little information is available on air-water flow through serpentine mini channel.

Most of the serpentine investigations are reported on micro devices (D_H < 1 mm, Co > 3.3). Leaving a gap of understanding for gas-liquid flow in serpentine mini channel geometry (2 mm > D_H > 1 mm), which is the geometric range of operation for PEMFC gas flow channel as well. Less information is available on the influence of orientation on the hydrodynamics of such flow. At the same time, not much is known about the influence of surface wettability on hydrodynamics of such flow. There is also ample scope for computational modeling either by using standard software or by developing numerical algorithm to capture some unique features of gas-liquid flow.

1.6. Motivation of the present work

The topic of the present investigation has been planned carefully based on the above discussions. As there are many unknown aspects of gas-liquid two-phase flow in mini

channels, it is a major objective of the present work to enhance our understanding through extensive experimentation. Therefore, an interest is felt to study the two-phase flow dynamics in three different serpentine channels. The range of which varies from micro (D_H < 1 mm, Co ≥ 4) to mini (2 mm> D_H >1 mm, Co≤ 1.6). Experiments are performed to identify flow patterns and pressure drop in all channels. The novelty of this work is its gas flow channel design and comparison of hydrodynamics in mini and micro serpentine channels. In all cases, both orientations are considered.

Therefore, one of the objectives of the present work is to find out the effect of channel orientation on flow. As the wettability of the channels also influences flow distribution in serpentine channels, experiments are performed with two different set of test sections having different bottom surface contact angle. Thus, this study is expected to find out the difference of hydrophilic and hydrophobic bottom surfaces on the flow. A survey of available literature reveals that only a limited number of investigations has been undertaken to simulate simultaneous gas-liquid flow in presence of wettability gradient. The wettability gradient can be defined as the gradual change in contact angle of a liquid drop on a solid surface with the change in axial location. In view of this, another objective of the present work is to develop CFD models for some typical phenomena of air-water two-phase flow for surfaces having wettability gradient.

1.7. Objectives of the present work

- To investigate air-water flow in serpentine geometries
- To investigate the effect of hydraulic diameter and orientation on flow regimes and pressure drop in the serpentine channel.
- To develop a numerical model, to study, water removal from single serpentine U-shaped geometry
- To investigate role of the wettability gradient on removal of suspended and adhered drop in single serpentine U-shaped geometry

1.8. Organization of thesis

The present work is undertaken to understand the physics behind the gas liquid flow through mini channels. As the serpentine channel finds its application in many areas, the forces governing the flow in the channel are of quite an interest.

The present chapter highlights the most relevant work and identifies the scope where improvement is required.

The second chapter deals with the details of the experimental set-up and describes the experimental methodology adopted for the same.

The results obtained after experimental investigations undertaken are reported in chapters three. In the third chapter the effects of hydraulic diameter on air water flow through mini serpentine channels have been studied. The flow pattern map and pressure drop graphs for air-water flow for both horizontal and vertical orientation have been discussed. The pressure drop models have been developed based on relevant dimensionless numbers. It also focuses on the influences of wall characteristics of the channel.

As the hydrodynamics is governed hugely by surface forces, this chapter deals with the transition that comes along by changing the contact angle of the bottom wall of the channel. The change of flow pattern regimes and its boundaries, the difference in pressure drop that comes along by introducing the hydrophobicity in the channel has been reported.

The fourth chapter describes the simulation of drop dynamics inside a serpentine channel. It consists of model development and description of computational domain. The chapter deals majorly with the effect of wettability gradient on air water interface, residence time of drop and water coverage ratio inside the channel. The variation of magnitude of gradient has also been reported. The effect of air velocity and drop diameter is also studied in detail. The simulations are performed with a solid GDL (gas diffusion layer). The co-current flow of air and water has been studied focusing the slug

flow regime and two directional wettability gradient has been applied to reduce mal-distribution in this regime.

In the fifth chapter conclusion and future scope of work are discussed.

CHAPTER 2 EXPERIMENTAL SETUPS AND PROCEDURES

In order to understand the hydrodynamics of air-water flow in serpentine geometry, extensive experiments have been carried out. Influence of different parameters such as hydraulic diameter, orientation and flow rate combination on flow distinction and pressure drop are estimated. The experiments have been carried out over a wide range of phase velocities as well as both for horizontal and vertical orientation. The details of the experimental setup and procedure are discussed in the present chapter. Moreover, different measuring instrument are also reported here in.

2.1. Fluids used

Zero air and de-ionized water are used as working fluids for all experiments. Zero air is filtered air which contains less than 0.1 ppm of hydrocarbon. The physical properties of the water namely viscosity, surface tension and density have been measured by viscometer, ring tensiometer and specific gravity bottle respectively. All the physical properties were measured at 27°. The experiments have been carried out at a temperature range of around 25° C – 35° C. The experimental results were found to be little or no variation with temperature.

Table 2.1: Properties of test fluids

Fluids Used	Density (kg/m^3)	Viscosity (kg/ms)	Interfacial Tension (N/m)
De-Ionized Water	1000	0.00095	0.071
Zero Air	1.29	0.000018	0.071

2.2. Experimental setup

Schematic of the experimental set up are shown in Figure 2.1. The setup comprises of fluid handling devices (syringe pump, rotameter), three test sections (T1, T2, T3) and connectors.

The experiments are performed in three different test sections.

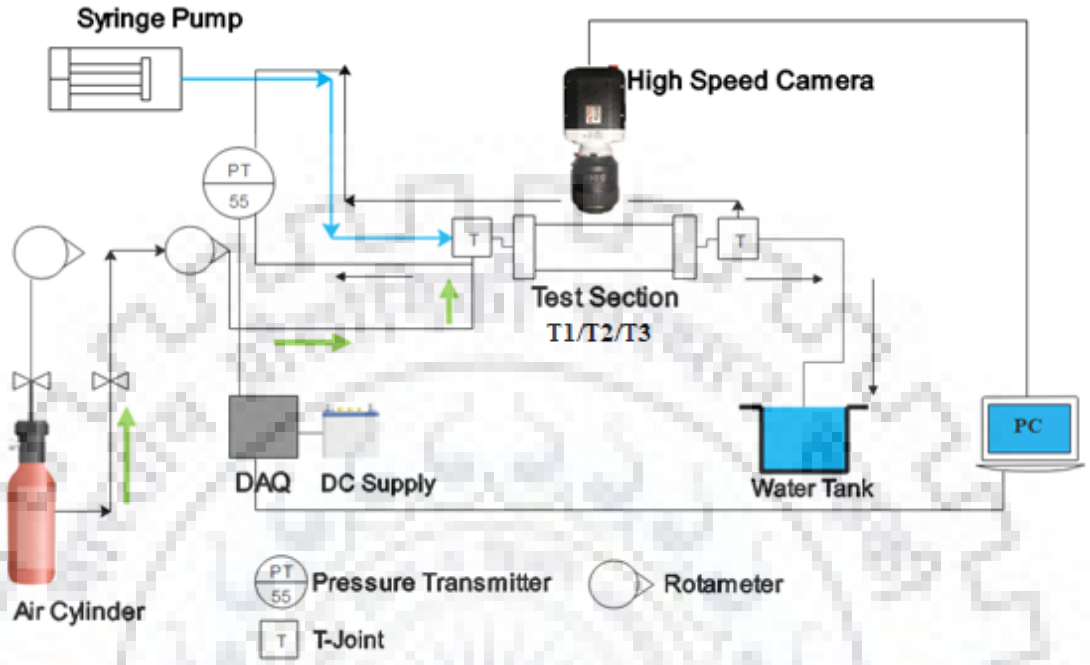

Figure 2.1: Schematic of the experimental set up

2.2.1. Fluid circulation and measurement system

Water was pumped by a syringe pump SP201 manufactured by Silver Meditech Corporation. The flow rate was varied from 10 ml/hr. to 600 ml/hr. An air cylinder operating approximately at the pressure of 0.4kg/ cm^2 has been used to supply air to the Rotameter. Two Rotameters, ranging from 0 LPM to 0.5 LPM and 0 LPM to1 LPM have been used. The detailed flow circuit for the liquids is presented in Figure 2.1. In the figure the blue lines represent the flow of de-ionized water and green arrows represents the flow of zero air. The arrows in black are indicating the two-phase flow.

2.2.2. Connectors

In order to introduce the two fluids in the test section copper connector is used. The copper connector is attached to ball valve which is a three-way valve. The valve is

connected to the test section, pressure transmitter high port and copper connector as shown in Figure 2.2

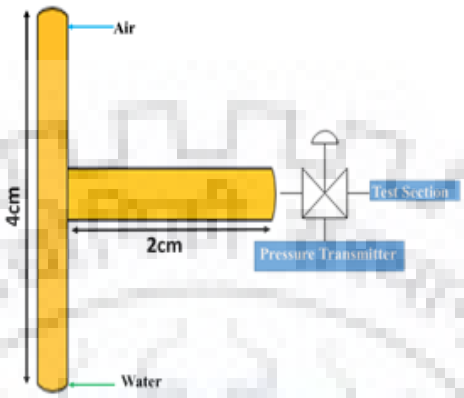

Figure 2.2: Connectors used in the system

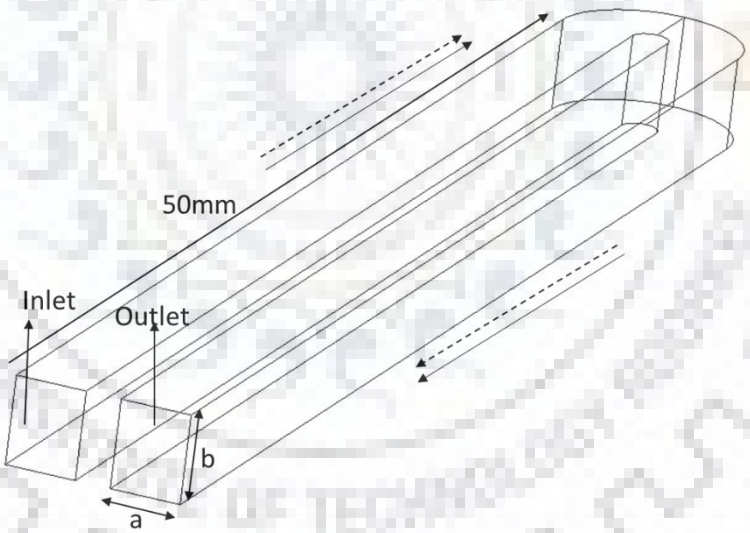

Figure 2.3: Schematic of U shape unit of test section

2.2.3. Test sections

As mentioned earlier three different categories of test sections namely T1, T2 and T3 are used for experimental investigations.

Each test section is comprised of 5 U shaped units as shown in Figure 2.3. Each arm of the U-shaped geometry is 0.05 m long. The test sections are viewed as 10 straight channels connected by nine 180° return bend. The width and depth of the cross section is denoted by 'a' and 'b' in Figure 2.3. Depending on different values of 'a' and 'b', Hydraulic diameter, D_H of the test sections are varied. Test sections are further classified according to hydraulic diameter. In all the test sections, the channels are fabricated in acrylic plate using a milling machine. The channels are covered with another smooth plate of same dimension. There are total three test sections of different hydraulic diameters. First, serpentine channels with a rectangular cross section of 5 mm^2 (D_H of 1.65 mm, a - 5 mm, b - 1 mm), second one with square cross section of 1 mm^2 (D_H of 1 mm) and the third of cross section 0.5 mm^2 (D_H of 0.65 mm, a - 5 mm, b - 1 mm). These test sections are referred as T1, T2 and T3. Photographic view of these test sections is given in Figure 2.4.

T1 **T2** **T3**

Figure 2.4: Photographic view of test sections

2.3. Instrumentations

Different instruments are used to measure pressure, contact angle as well as visualize the flow are discussed in the in this section

2.3.1. Differential Pressure Transmitter

Pressure drop across the serpentine channel was determined by a precision differential pressure transmitter (STD 700, 34-ST-03-101) manufactured by Honeywell and it possesses an accuracy of 0.05% of span. The high port of the pressure transmitter was connected at the inlet and low port to the outlet. Time averaged pressure drop data was obtained with the help of a data acquisition system (NI-cDaq 9174, 32-bit, 500 Hz) procured from National Instruments Corporation. The time span of data recording was approximately 5 minutes. The reason of choosing the specific time range is to ensure that the flow conditions remain same for a period of time. This produces large number of datapoints. This data needs to be analyzed in-order to minimize the chances of erroring pressure drop. Also, to compare the slugs, in order to find out water coverage ratio, for different orientations a fixed period of time is needed.

2.3.2. Visualization and Image processing

Visualization of flow distribution inside the channels is carried out using a high-speed video camera (Phantom Micro Lab 110). The frame speed was varied within a range of 2100 fps to 6200 fps along with an altering resolution range of 1027 × 780 pixels to 712 × 712 pixels depending upon the orientation of the channel. The exposure time was fixed at 40μs. An adjustable light source is used at the back of the test section in order to acquire the best quality images.

The images obtained are used to calculate certain significant parameters and are processed using Image J software as shown in Figure 2.5

The procedure is used to calculate time averaged in-situ water coverage ratio in slug regime. First, the picture is converted to detect the edges properly and finally it is

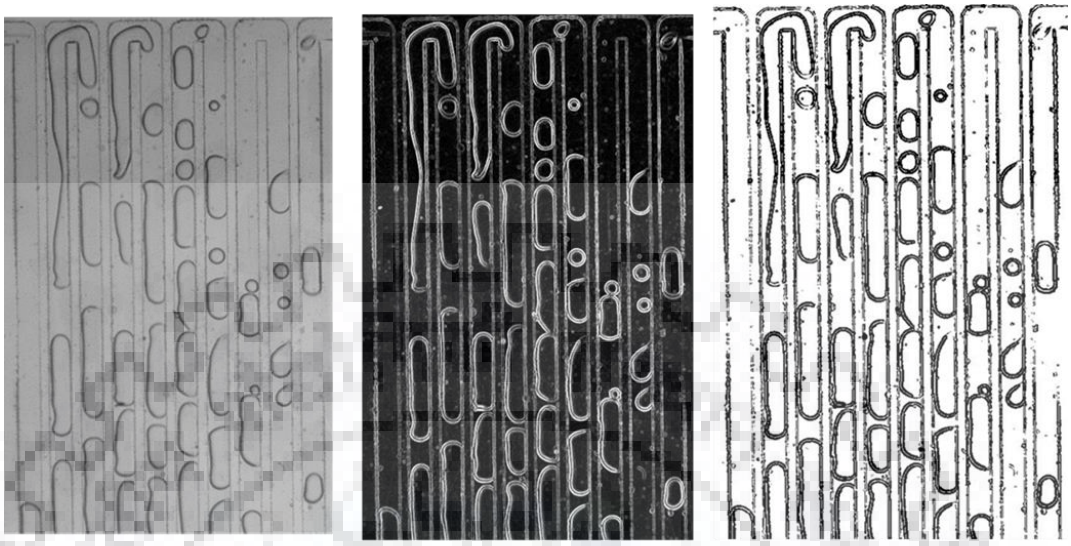

Figure2.5: Representative figure for image analysis

converted to a binary image. The individual slug area (A_i) is calculated using ImageJ. Instantaneous areas covered by slugs are calculated as follows in each channel:

$$A_n = \sum_i A_i \tag{2.1}$$

where, A_i is the area of ith slug in the nth frame as shown in Figure 2.5. Instantaneous water coverage ratio α is calculated as follows:

$$\alpha = 1 - \frac{A_n}{L_f * D_H} \tag{2.2}$$

where L_f is the length captured in the picture, that is nothing, but the length of the particular frame considered. Similar procedure is repeated to calculate α for a given number of frames for a specific video. Finally, the time averaged value of water coverage ratio (α_t) is estimated from these instantaneous values over a period of time.

2.3.3. Goniometer

The contact angle of water with acrylic is measured using a contact angle goniometer (Kruss Drop Shape Analyser (DSA25)). The accuracy of goniometer lies in the range of ±0.5° and the method for measuring the angle is sessile drop method using Young Laplace equation. The contact angle of water with acrylic is 72°.

2.4. Experimental procedure

The experimental procedures adopted are discussed below.

Before the experiments, the channels are cleaned with ethanol. The flow regimes are observed for both horizontal and vertical orientation for all channels. After the experiments are over, the channels are dried by passing high velocity air for 15 minutes.

Before initiation of the experiments, the syringe pump and rotameter are calibrated, and the fluid properties are evaluated. Then air is introduced in the test section. After introducing the air flow rate is introduced at the entry section. The two-phase mixture flows through the test section and enters the exit section. Initially, water velocity is increased at a constant air flow rate. The air velocity is then changed, and the readings are repeated.

The range of water and air velocities are varied from 0.0011 m/s to 0.33 m/s and 0.33 m/s to 16.66 m/s, respectively. Thus, the range of gas phase Reynolds number varies from 67-1348 however that of liquid phase varied from 2 to 333**.** In order to correlate with active fuel cell, from the volumetric flow rate of air (Q_G), current density (i) is calculated for a given range of stoichiometric ratio (λ_s, 0 - 10), as discussed by Steinbrenner et al. (2011) as follows:

$$Q_G = \frac{iA_{act}M_G}{0.21F\rho_G}\lambda_s \tag{2.3}$$

The active area of the channel is the channel area. The range of water and air velocities, Reynolds number and corresponding current density in case of an active fuel cell are reported in Table 2.2.

For each combination of air-water velocities, the flow patterns are identified from visual and photographic observations and the pressure drop has been measured by differential pressure transmitter. Each reading is repeated 3 - 4 times and an average value is taken. The readings are observed to vary within ± 5%. This exercise is repeated over the entire range of phase velocities.

Table 2.2: Operating condition for T1, T2 and T3

Diameter (mm)	**Re_{GS} (Reynolds Number Air)**	**Re_{LS} (Reynolds Number Water)**	**Current Density (A/cm^2)**	**Active Area (mm^2)**	**Suratman Number** $Su = \sigma \rho_L D_H / \mu_L^2$	**Bond Number** $Bo = \frac{D_H}{\sqrt{\sigma / (g \Delta \rho)}}$
1.65 (D_H 165)	67-1348	2-54	1.5	888.6	112600	0.61
1.00 (D_H 100)	203-1016	5-166	2.6	521.4	72000	0.36
0.65 (D_H 065)	146-734	16-333	2.6	521.4	44357	0.24

2.5. Uncertainty Analysis

To measure the uncertainties associated with different parameters in subsequent calculations, Single Sample Error Propagation Method is used. The overall measurement of uncertainty of a parameter, *E* is given by:

$$\delta E = \sqrt{\sum_{i=1}^{n} \left(\frac{\delta E}{\delta x_i}\, \delta x_i\right)^2} \tag{2.4}$$

Here $E = f(x_1, x_2 \ldots\ldots\ldots)$ and x_n represents the variable. After calculating the uncertainties in measurement error for each data point is obtained by using the formula given below:

$$\in = \frac{\delta E}{E} * 100 \tag{2.5}$$

Table 2.3 summarizes uncertainties of all the parameters involved.

Table 2.3: Uncertainty of parameters

Quantity	**Uncertainty**
Volumetric Flow rate (Water)	±1%
Volumetric Flow rate (Air)	±2%
Tube Diameter	±2%
Tube length	±0.25%
Pressure Drop(normalised)	±2%
Reynolds number liquid phase (Re_{LS})	2.01%
Reynolds number gas phase (Re_{GS})	2.01%
Weber number gas phase (We_{GS})	2.03%
Weber number liquid phase (We_{LS})	2.03%
Discharge from Channel	4%
Contact Angle	±0.5°

CHAPTER 3 EXPERIMENTAL INVESTIGATION OF AIR-WATER FLOW

In this chapter experimental observations of air-water flow through the test sections are presented and efforts have been made to understand the hydrodynamics of the flow. All three variations of test sections along with orientations are studied. Flow regimes, as observed from photographic recording are presented. Flow patterns are found to be varied for different hydraulic diameter, orientation and flow combinations. Different transitions criterion in terms of Weber Number are proposed. Modified form of friction factor is also suggested.

3.1. Flow patterns observed

Several unique flow patterns are observed during the flow of air and water. The interfacial distributions characterizing each flow pattern are described below. Photographic representation of each flow regime is presented in Figure 3.1, 3.2 and 3.3 for T1, T2 and T3 respectively.

A detailed discussion on the flow regimes are given below.

Annular Flow

This flow pattern is observed both in T1 and T3. For T1 the annular flow is mainly observed in the range of air superficial velocity (U_{GS}) and water superficial velocity (U_{LS}) with values varying between 0.33 m/s to 6.66 m/s and 0.0033 m/s to 0.0055 m/s respectively. For T3 the range of air superficial velocity (U_{GS}) and water superficial velocity (U_{LS}) varies between 13.33 m/s to 16.33 m/s and 0.0055 m/s to 0.11 m/s respectively.

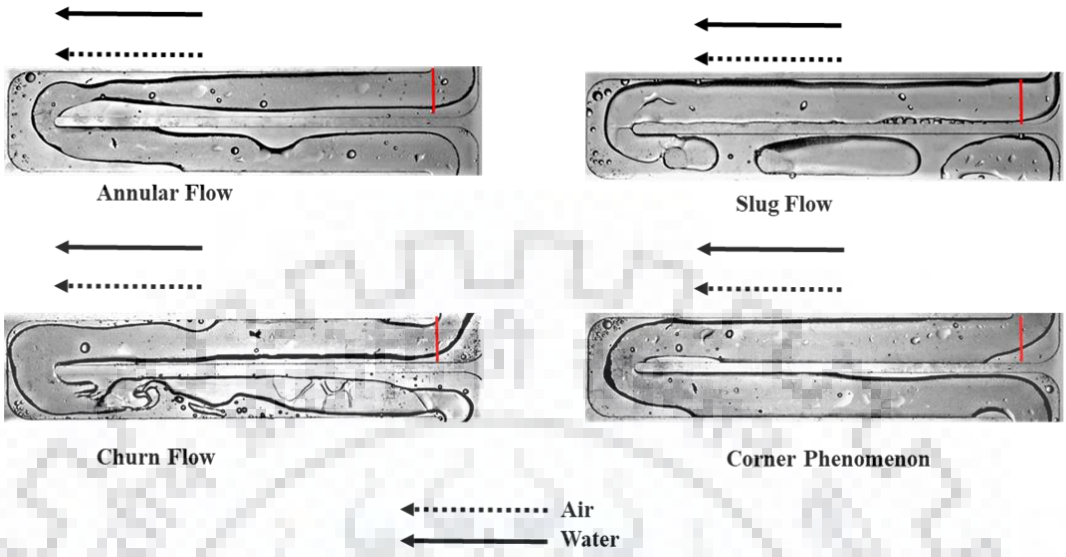

a) Horizontal

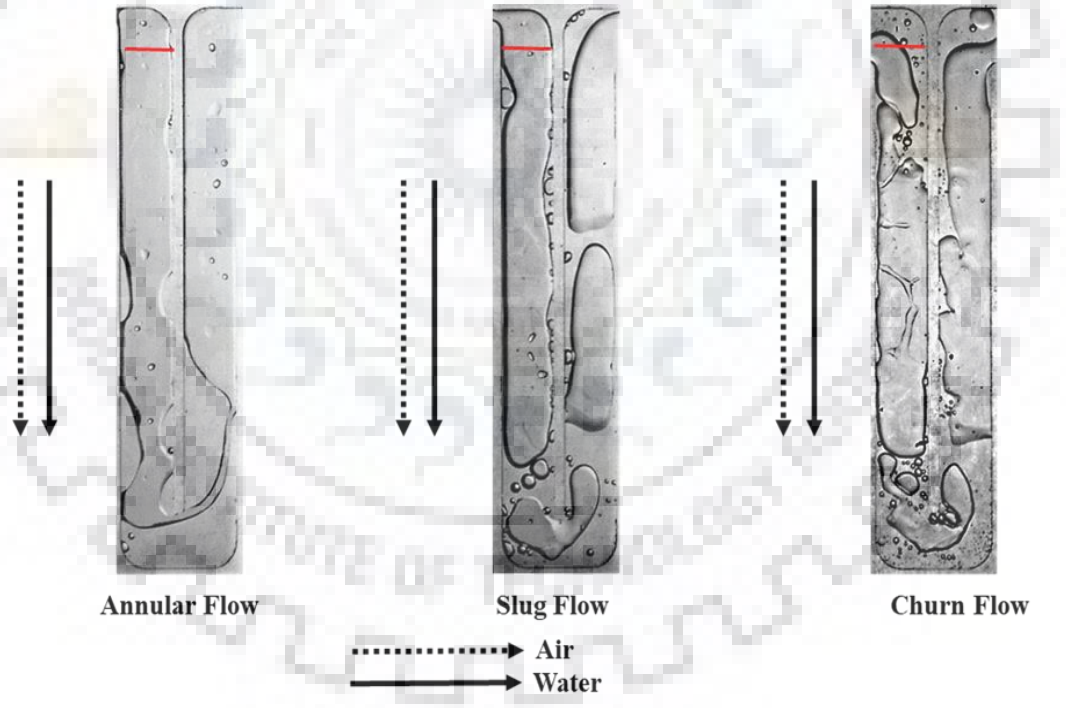

b) Vertical

Figure 3.1: Photographic representation of flow patterns for T1in both orientations (length of bar 5 mm)

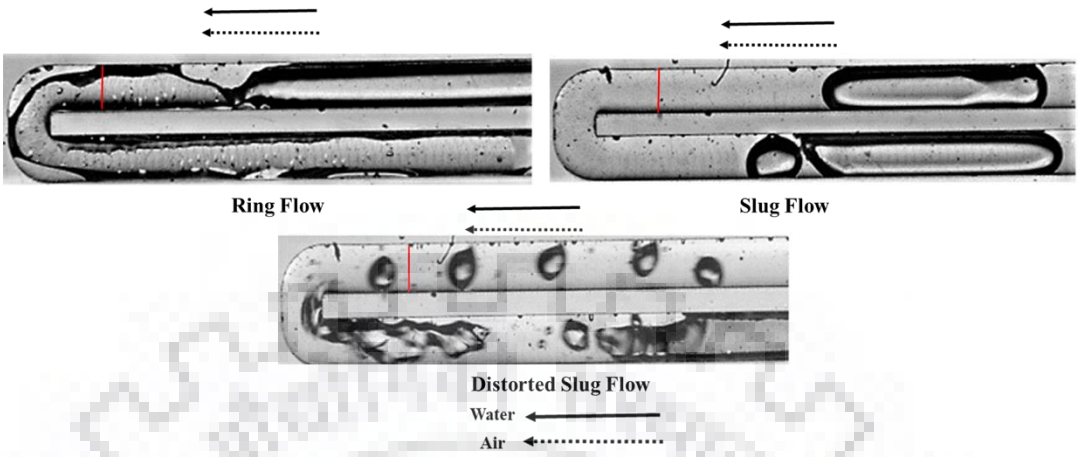

a) Horizontal

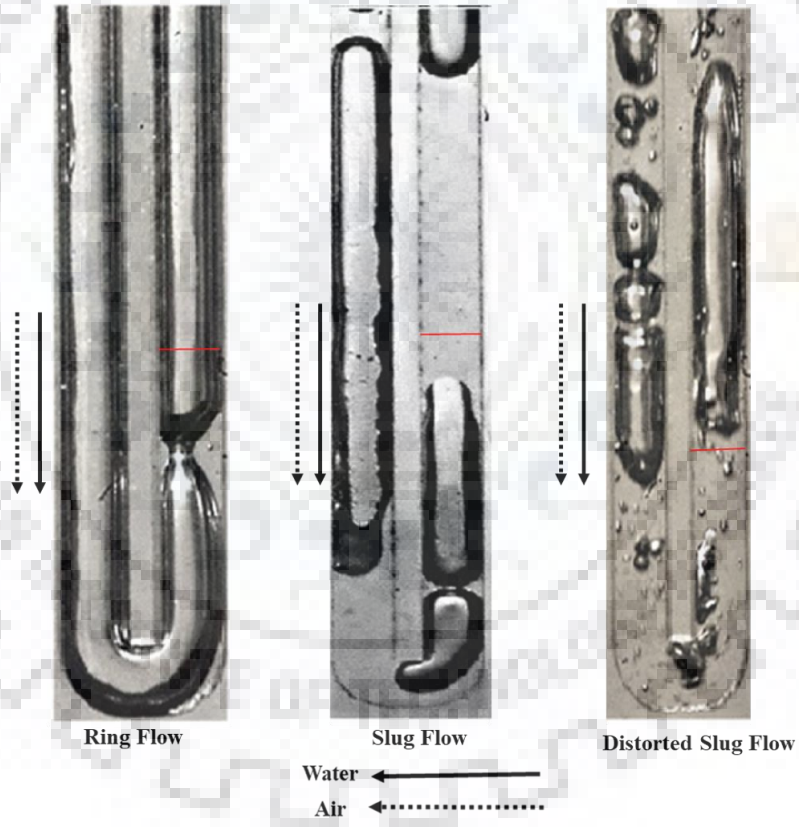

b) Vertical

Figure 3.2: Photographic representation of flow patterns for T2in both orientations (length of bar 1 mm)

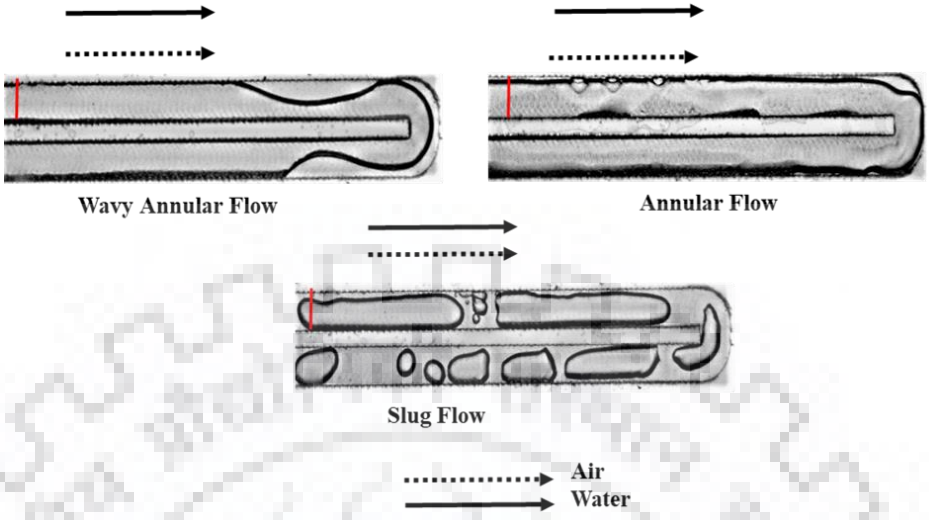

a) Horizontal

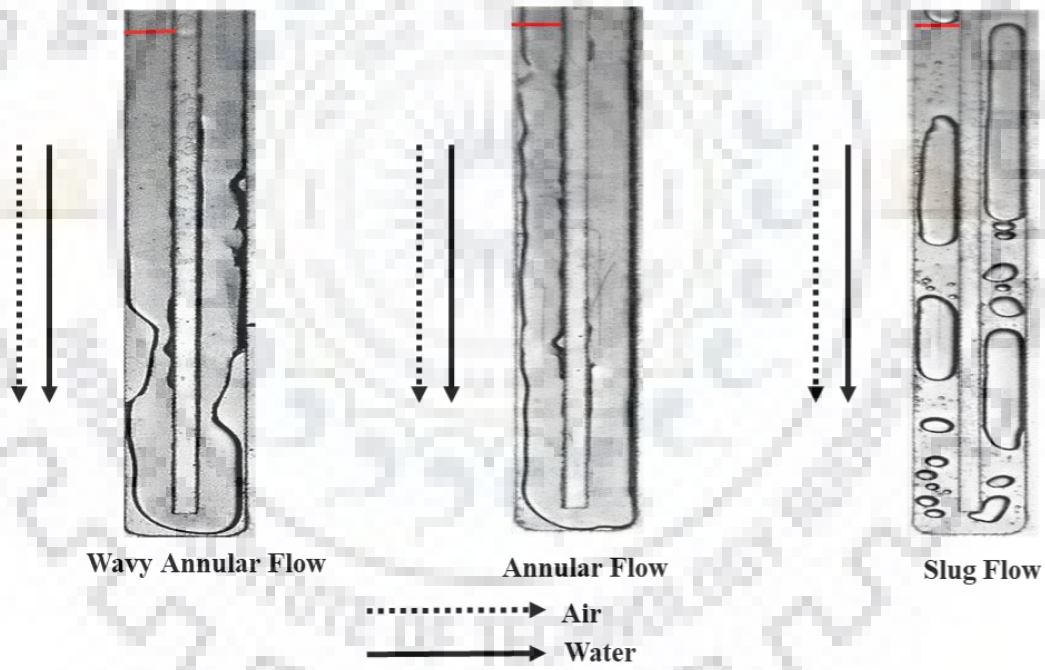

b) Vertical

Figure 3.3: Photographic representation of flow patterns for T3 in both orientations (length of bar 1 mm)

It is characterized by the presence of a thin water film at the wall and air at the central core. At the interface of air and water irregular waves are present. Often small water drops are also spotted inside the gas core. This results in an asymmetric appearance of the interface on both sides of the air core. The amplitude and wavelength of the interfacial wave depend on phase velocities.

Churn Flow

This flow regime is observed only in T1. It is mainly observed in the range of air superficial velocity (U_{GS}) and water superficial velocity (U_{LS}) with values varying between 1 m/s to 6.66 m/s and 0.0044 m/s to 0.033 m/s respectively. The flow is quite chaotic in nature and not very well structured. High velocity causes breaking down of stable slug flow, giving its way to oscillatory motion of liquid in the channel. It is an intermittent flow pertaining to large fluctuations in void fraction and interface of gas-liquid.

At lower liquid velocity, it is often characterized by the degeneration of annular film flow forming large wave like structure at the interface. At higher gas velocity, the flow can be seen as the breaking of slug flow along with occasional bridging across the channel (Figure 3.1). Churn flow is a characteristic of mini, meso and conventional macro channel. The test sections T2 and T3 exhibits the behavior of microchannel and the flow patterns reported in these channels are dominated by slug flow regime because they are more surface tension dominated.

Slug Flow

It is observed in all the three test sections. Slug flow is characterized by the frequent appearance of bullet shaped bubbles surrounding by thin liquid film with a liquid bridge forming a plug between them. The slugs observed in the channel often equalizes the channel width. Slugs are generally long at the upstream of any bend. However, on encountering a bend at the downstream it breaks to give smaller slugs and sometimes drops.

In case of T1 it is observed for a narrow range of air superficial velocity (U_{GS}) and water superficial velocity (U_{LS}) with values varying typically in the range of 0.33 m/s to 0.66 m/s and 0.022 m/s to 0.033 m/s respectively. In case of T2, slug flow was observed for a wide range of air superficial velocity (U_{GS}) and water superficial velocity (U_{LS}) with values varying typically in the range of 1.67 m/s to 5 m/s and 0.027 to 0.16 m/s respectively. For T3 the value of air superficial velocity (U_{GS}) varies between 13.33 m/s to 16.66 m/s and water superficial velocity (U_{LS}) varies between 0.07 m/s to 0.2 m/s. It is characterized by alternate passage of air and water plugs through the test section. The air plugs are regular in shape with a clear round nose. Sometimes, small air bubbles are found in the water slug entrapped between two successive air plugs. With increasing water velocity, the water bridge between two successive air plug increases. However, there is a difference of slug flow observed in macro channel and the present investigation. The slugs are not entirely present in all channels at the same point of time as seen in Figure 3.2. Similar observation can be made with Figure 3.3a. Slugs are only present in one or two channels. This gives rise to mal distribution in real channels of PEMFC.

Distorted Slug Flow

It is majorly seen in the range of 0.07 to 0.21 m/s of U_{LS} and 8 to 10 m/s of U_{GS} in T2. At higher gas velocities well defined slug flow gets disturbed and larger air plug along with distorted water slugs were observed in the channel. The reason can be attributed to increase of interfacial surface forces due to increase of air velocity which results in deformed interface of water slug. However, at this higher velocity of air and water the non-uniform distribution of flow pattern disappears as can be seen in Figure 3.2. Majority of the channels are now filled with long distorted air plugs.

Ring Flow

This flow pattern is observed in T2. The value for superficial gas velocity (U_{GS}) typically ranges from 1.66 m/s to 8.33 m/s and superficial water velocity lies in the range of 0.0055 m/s to 0.055 m/s (U_{LS}). At lower water flow rates, the ring flow prevails at the entire range of air flow rate. At lower water flow rates, the channel wall is wetted by water and air flows at the core. A drop of water appears intermittently in the form of ring moving from inlet to outlet. The air- water interface of the gas core is compressed due to presence of this drop giving rise to a ring structure. This is clearly visible from Figure 3.2.

The thickness of the interface is not uniform on both sides of the drop in horizontal flow. This can be attributed to the effect of buoyancy is in horizontal flow. This flow disappears as the water velocity is increased to 0.03 m/s. The channel wall is hydrophilic (contact angle 72°), as soon as the flow initiates, the channel wall is wetted by water. As a result of this hydrophilicity the rings formed at lower superficial velocities surrounding the air core tries to adhere to the wall surface and resist the movement of air. With an increase of water flow, the holdup of the water increases to form well defined slugs of air.

Wavy Annular Flow

This flow pattern is observed only in T3. The value for superficial gas velocity (U_{GS}) typically ranges from 3.33 m/s to 10 m/s and superficial water velocity lies in the range of 0.0055 m/s to 0.11 m/s (U_{LS}).Water is present along the side wall in a thin film. The majority of the channel is covered with gas core surrounded by very thin film of water. The air-water interface is characterized by the presence of waves of higher amplitude closer to bends. It gives the flow regime a wavy appearance. Interface has an axisymmetric appearance due to presence of wave on both sides. However, the amplitudes of waves are not large enough to break the gas core and form slugs (Figure 3.3).

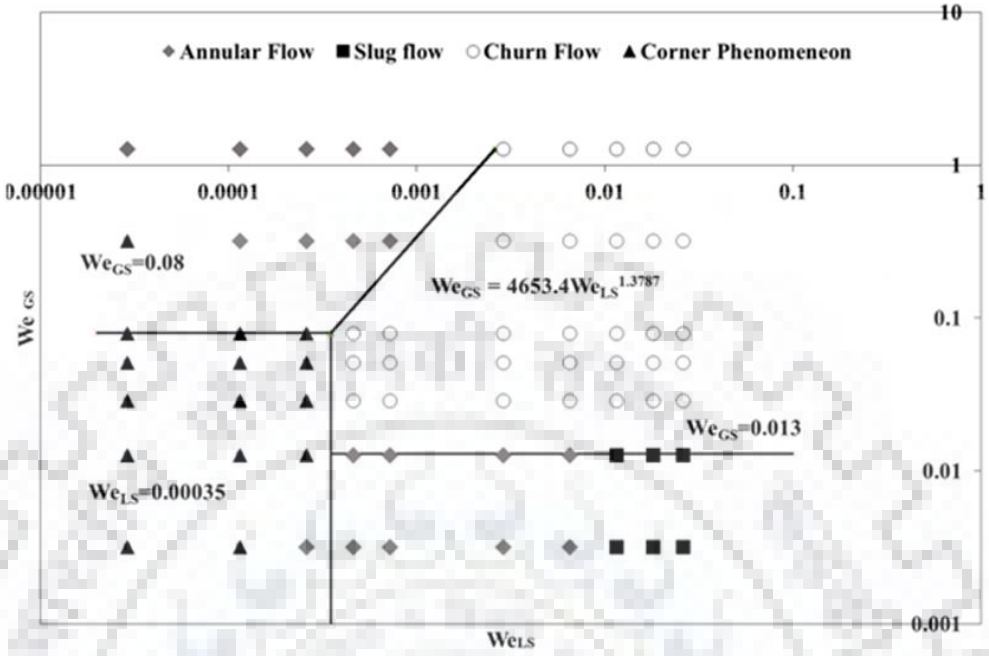

a) Horizontal

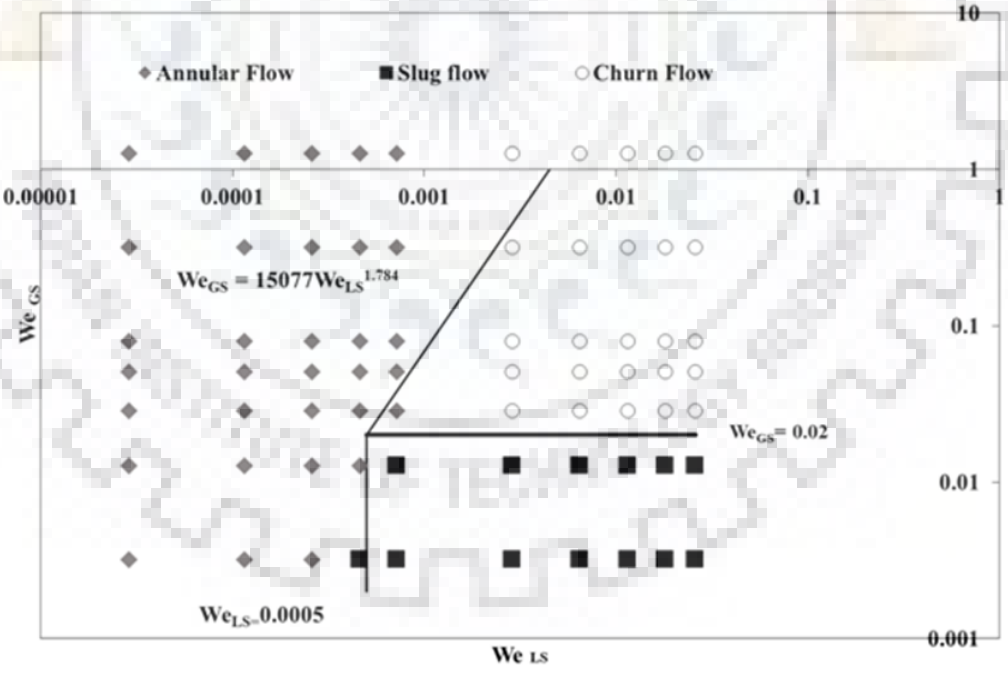

b) Vertical

Figure 3.4: Flow regime maps for T1 in both orientations in terms of phase Weber number

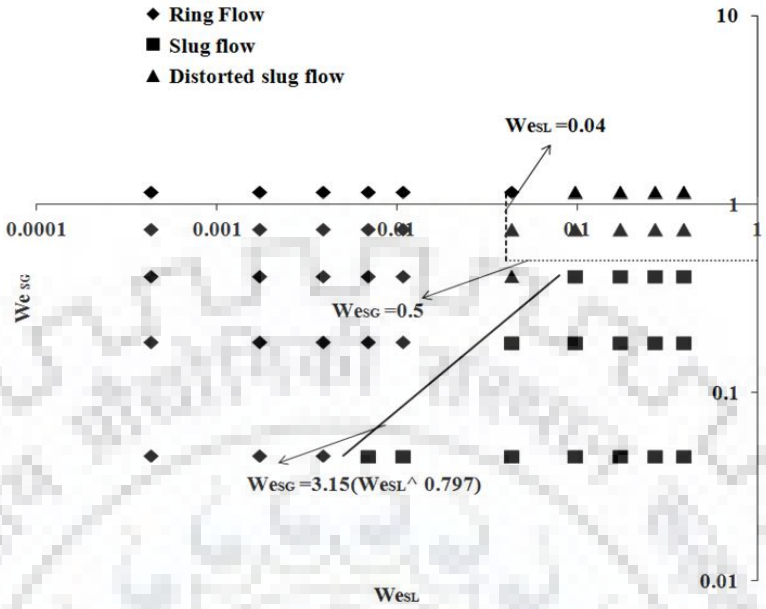

a) Horizontal

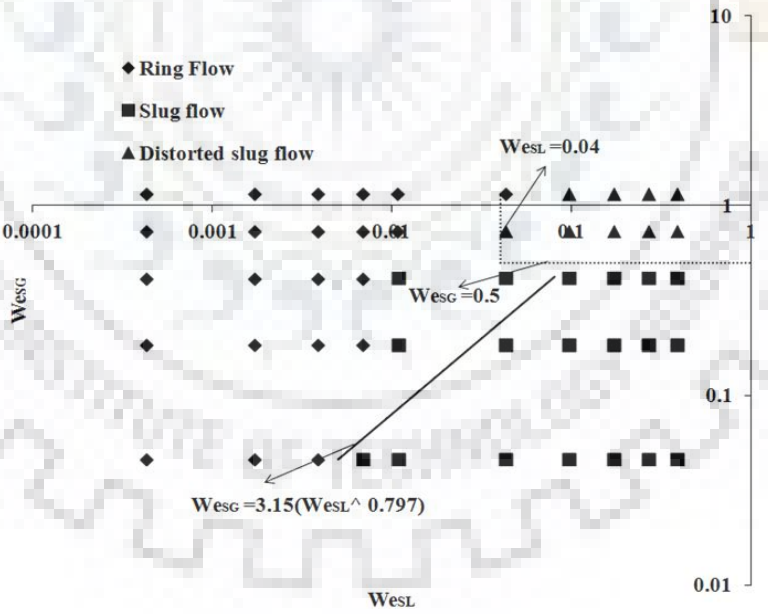

b) Vertical

Figure 3.5: Flow regime maps for T2 in both orientations in terms of phase Weber number

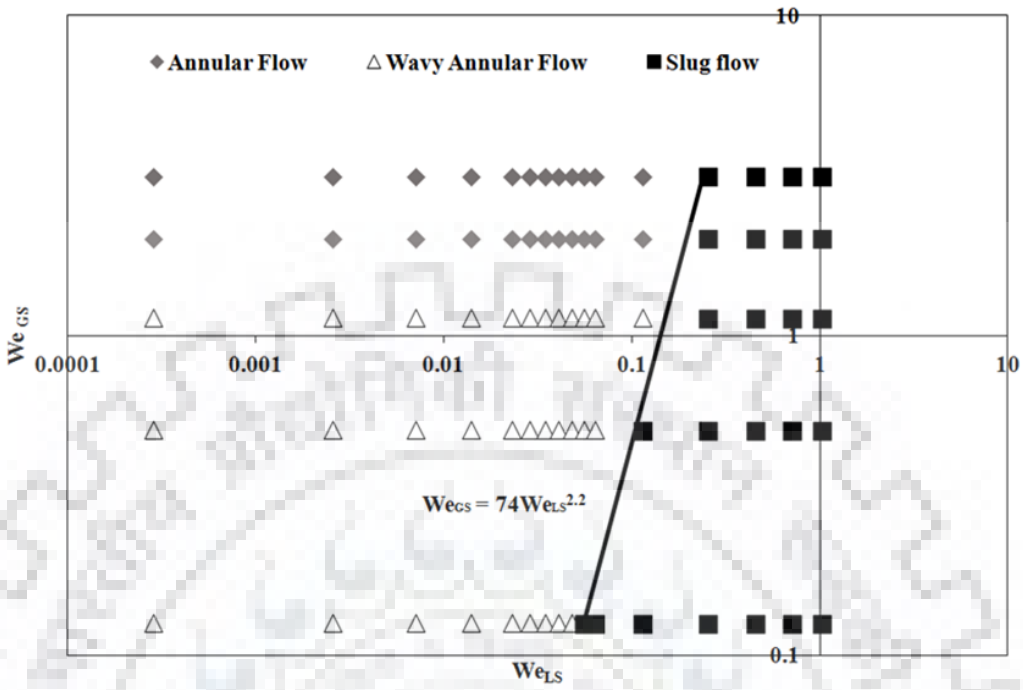

a) Horizontal

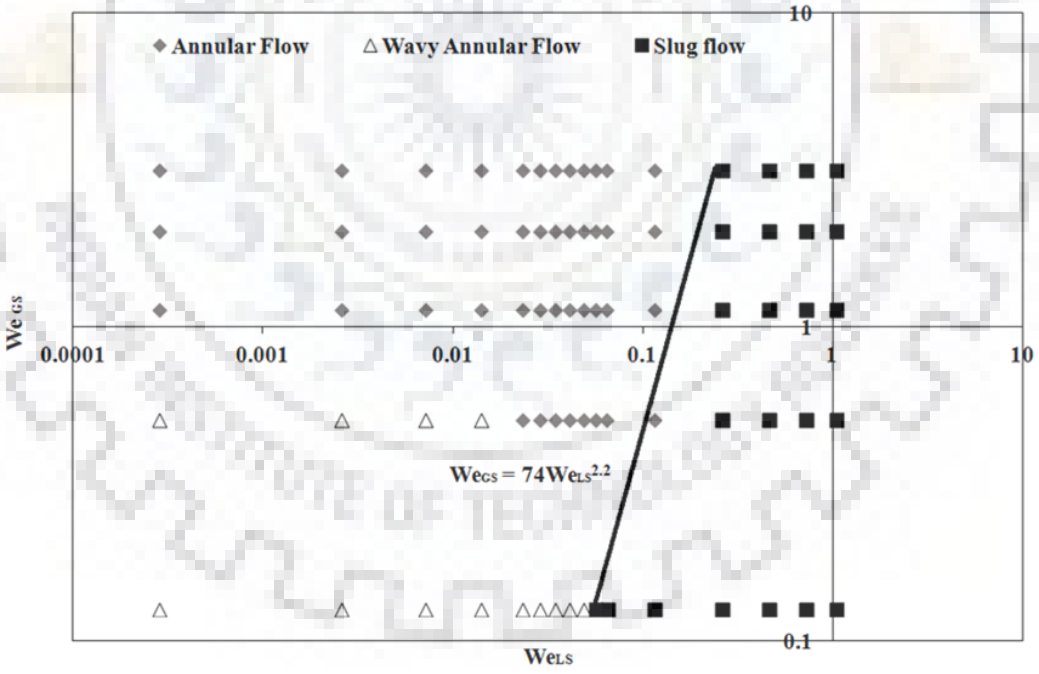

b) Vertical

Figure 3.6: Flow regime maps for T3 in both orientations in terms of phase Weber number

Range of existence of these flow patterns are plotted in terms of phase Weber number as

$$We_{LS} = \frac{U_{LS}^2 D_H \rho_L}{\sigma} \tag{3.1}$$

$$We_{GS} = \frac{U_{GS}^2 D_H \rho_G}{\sigma} \tag{3.2}$$

Figures 3.4, 3.5 and 3.6 show the flow pattern map for T1, T2 and T3 respectively. Important outcomes are and comparative study of T1, T2 and T3 are discussed below.

3.1.1. Effect of orientation

A comparison of Figure 3.4a and b shows that stagnant water pockets are formed in horizontal orientation. This has been termed as corner phenomenon. It is observed for

$$We_{GS} < 0.08 \text{ and } We_{LS} < 0.00035 \tag{3.3}$$

- In this flow pattern, the channel is majorly occupied with gas core and water running on the walls forming a noticeable interface along the side of the walls. Water accumulates at the bend forming a water pocket and thus increases the water clogging in the channel.
- A time series of such a phenomenon is depicted in Figure 3.7. Large amount of stagnant pocket of water at the bends are visible from this figure. The water clogging can affect the performance of fuel cell as it blocks the effective area as well as giving an additional resistance to flow. Beyond $We_{GS} > 0.08$ corner phenomenon is converted to slug flow.

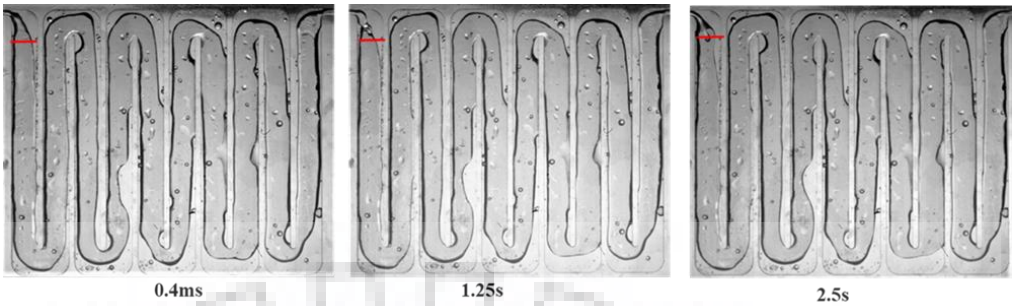

Figure 3.7: Corner phenomenon in T1 (A)

- Another interesting observation is that, the existence of annular flow at lower gas phase Weber number, $We_{GS} < 0.013$ in horizontal orientation of T1. This happens when enough liquid accumulation occurred in horizontal orientation after corner phenomenon.

- With increasing We_{LS} beyond 3.5×10^{-4}, corner phenomenon gives rise to annular flow. This flow regime subsequently changes to slug flow with further increase in We_{LS}. Hence, this annular distribution at lower We_{GS} can be taken as a transition to slug from corner phenomenon. For $We_{GS} > 0.013$ corner phenomenon form churn flow.

- On the other hand, in case of vertical orientation of T1, annular flow is observed for very low We_{LS} (3×10^{-5}) and We_{GS} (3.2×10^{-3}) instead of corner phenomenon. Range of existence of annular flow is different in vertical orientation than horizontal one.

- Hence, it can be said that the vertical orientation favours draining of water and therefore formation of annular flow for very low air and water velocities. It avoids accumulation of water as observed in horizontal orientation. With increasing We_{LS} beyond 5×10^{-4}, it converted to slug for $We_{GS} < 0.02$.

- It can be seen from Figure 3.4b that in the case of vertical orientation the boundaries are shifted to a greater extent and can be demarcated sharply at $We_{GS} = 0.02$. For $We_{GS} > 0.02$ annular flow gives way to churn flow as

$$We_{GS} = 15077 We_{LS}^{1.8} \tag{3.4}$$

On the other hand, for horizontal orientation this transition is predicted for $We_{GS} > 0.08$ as

$$We_{GS} = 4653.4 We_{LS}^{1.4} \tag{3.5}$$

Both transition lines showed similar character with difference in slope.

- In case of vertical orientation of T1, slug is converted to churn as $We_{GS} > 0.02$ for $We_{LS} > 0.0005$ and for the horizontal orientation that happens for $We_{GS} > 0.013$ and $We_{LS} > 0.00035$. Hence transition of slug to churn is also similar in nature for both the orientations.
- In case of T2, transition lines are same for vertical and horizontal orientations (Figure 3.5a and b). In both the orientations, ring flow in both the orientation gives way to slug flow. At a particular water superficial velocity, droplet encircling the gas core increases its size, disrupt the gas core to form well defined slugs. With an increase in interfacial waviness ($U_{SG} > 6$ m/s) the air plugs are deformed and become larger in size to form distorted slug flow.
- For $We_{GS} < 0.5$, Ring to slug transition followed as:

$$We_{GS} = 3.15 We_{LS}^{0.797} \tag{3.6}$$

For $We_{GS} > 0.5$, Ring to distorted slug transition followed as:

$$We_{LS} > 0.05 \tag{3.7}$$

- On the other hand, for T3, Figure 3.6a and b are almost identical with only two major flow regimes in both orientations, annular and slug. The transition from annular to slug in both the orientation is predicted as

$$We_{GS} = 184.55 We_{LS}^{2.5} \tag{3.8}$$

- Other interesting phenomenon observed, in case of T2, is that as channels are interconnected, the flow in one channel affects the other. If a large slug of air encounters a bend in its flow path its shape changes. At lower air superficial velocity (< 3 m/s) the large slug breaks and formed larger number of small slugs and drops followed by bridges of water in the downstream of bend in case of horizontal orientation.

- On the other hand, upstream of bend is filled with air at core and water at side wall giving rise to annular structure. Slug coalesce is also taking place, however that is more common in vertical orientation as the slugs are moving upward which reduces the water bridges length. This gives rise to more annular like structure at the downstream of bend in vertical orientation.

- However, in horizontal orientation more smaller slugs and drops are produced at the downstream of bends giving rise to non-uniform distribution in the channels (Figure 3.2a and 3.2b). Similar observation is also made by Lu et al. (2011) for parallel channels.

3.1.2. Effect of reduction of hydraulic diameter from mini to micro

A comparison of Figure 3.4, 3.5 and Figure3.6 reveals the followings:

- As the confinement number of the channels changes from mini to micro (1.6 to 4.4), numbers of flow patterns are less. As the confinement number increases the annular flow and slug flow appears to be dominant flow patterns.
- For the micro-channel, surface forces dominate over gravity (Bond number is 0.24). As a result, in T3 the flow patterns and their range of existence are almost similar in both the orientation. Similar observation can be made for T2. Hence,

it can be said that as the confinement number increases from 1.6 to 2.2 to 4.4, the influence of orientation on flow regimes and their transition boundaries eliminates.

- A comparison of Figure 3.4, 3.5 and 3.6 reveals that phase Weber numbers in case of T3 are higher than that of T1 and T2. In case of T3, maximum value of We_{GS} increases to 3.2 while that of We_{LS} is close to 1.
- Hence, it can be said that, in case of T3, majority of the flow regimes lie in gas phase inertia dominated regime ($We_{GS} > 1$). On the other hand, for T1 and T2, as the phase Weber numbers are less than unity, in majority of the cases, it can be clearly concluded that all the flow regimes are surface tension dominated in mini channels.
- For the micro channel annular flow is observed as a dominating flow pattern. On the other hand, range of existence of annular flow is observed in T1 are limited and dependent on orientation. For vertical orientation it occurs for $We_{LS} < 0.0005$ and $We_{GS} > 0.001$. For T3, annular flow occurred for $We_{LS} > 0.0001$ and $We_{GS} > 0.1$.
- In similar range of phase Weber numbers, ring flow is noticed by Malhotra et al. (2017). At $We_{GS} = 1$, a comparison of T1, T2 and T3 further reveals that existence of annular structure increased from $We_{LS} 0.001$, $We_{LS} 0.01$ to $We_{LS} 0.1$ as the diameter of the channel changes its characteristics from mini(T1) to micro (T3). Zhou et al. (2017) also reported annular flow in serpentine geometry with confinement number 15.3. Liquid phase Weber number in case of annular flow, estimated from their data are $We_{LS} 1.17$ for $We_{GS} 0.04$.
- Hence, it can be said that micro channels favour the formation of annular flow for larger range of We_{LS}. Higher the confinement number higher is the value of We_{LS} .

- Churn flow is the dominating flow pattern in T1. A comparison of Figures 4b and 5b at same phase Weber numbers ($We_{GS} > 0.1$ and $We_{LS} > 0.01$) reveals that churn flow at T1, slug at T2 converted to annular flow in T3

A comparison with Lu et al. (2009) and Lu et al. (2011). It reveals that for parallel hydrophilic gas flow channels at horizontal orientation, two major regimes are observed i.e. slug and film. Lu et al. (2009) also reported mist flow at a higher superficial velocity of air which is not observed in the present case. The differences observed in the flow patterns can be attributed to the fact that the range of water superficial velocity, way of water injection and the geometry of the channels of the two studies.

It has been reported in literature (Lu et al. (2009) that slug flow is responsible for causing mal distribution in gas flow channels. Churn also shows a chaotic and unstable nature. Therefore, it can be concluded that at similar phase Weber numbers micro channels forms more desirable flow regimes. On the other hand, a film/annular flow is a favourable pattern in PEMFC from the perspective of water removal (Lu et al. (2009)). Hence, it can be said that lowering hydraulic diameter to micro rage, favours water removal at lower water velocities.

3.2. Pressure drop Characteristics

Pressure drop characteristic has an important role in two phase flow and particularly in PEMFC. Bend of the channel adds an extra dimension by adding on the pressure as well as inducing changes in the interaction of air water flow that leads to either coalescence or disintegration of bubbles and slugs. Attempts have been made to understand the pressure drop characteristics during air-water flow through the serpentine channels in both the orientation and document the effect of hydraulic diameter on the pressure drop. In this section, first the experimental characteristics of pressure observed is discussed followed by analytical modelling of the same.

3.2.1. Experimental Pressure Drop

The pressure transmitter measured differential pressure between the inlet and outlet of the test section. Experimental pressure drop is denoted by ΔP . Figure 3.8 and Figure 3.9 show the raw signals and corresponding PDF for T1 and T3.

It can be seen from Figure 3.8 for the annular flow, signal varies with time. However, amplitude of variation is less. A sharp peak in PDF is noticed at a ΔP of 10668. On the other hand, the peak is not defined for churn flow which represents the chaotic nature of the flow regime.

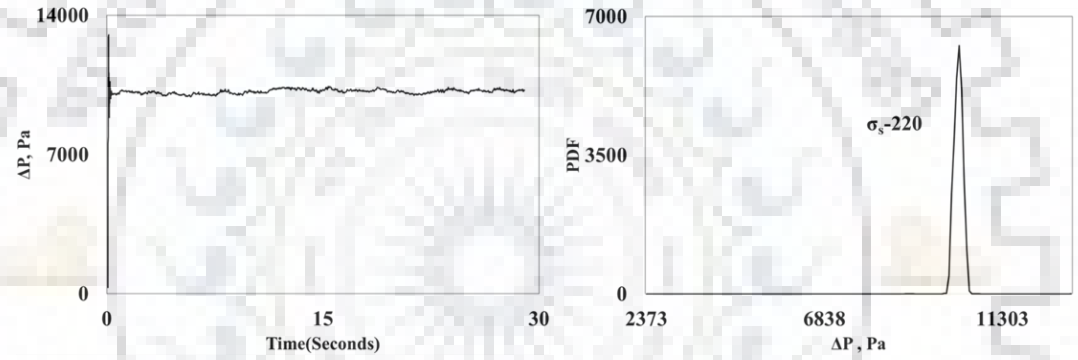

a) Annular Flow

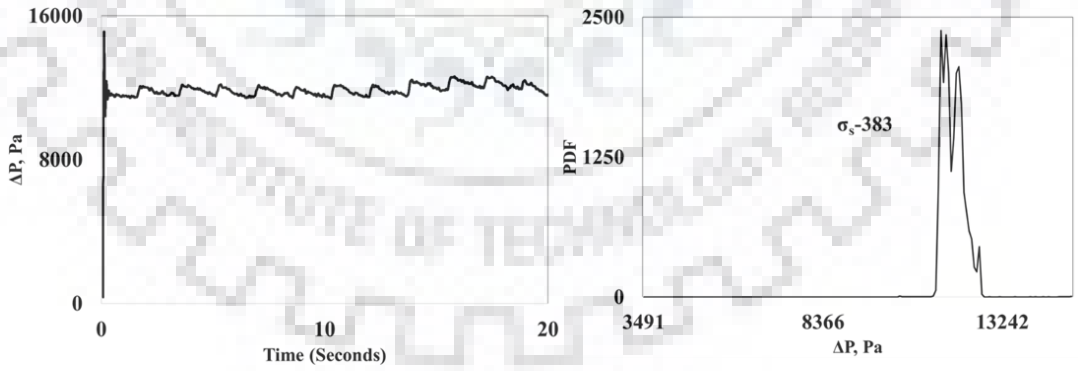

b) Churn Flow

Figure 3.8: Pressure Signal and corresponding PDF for T1

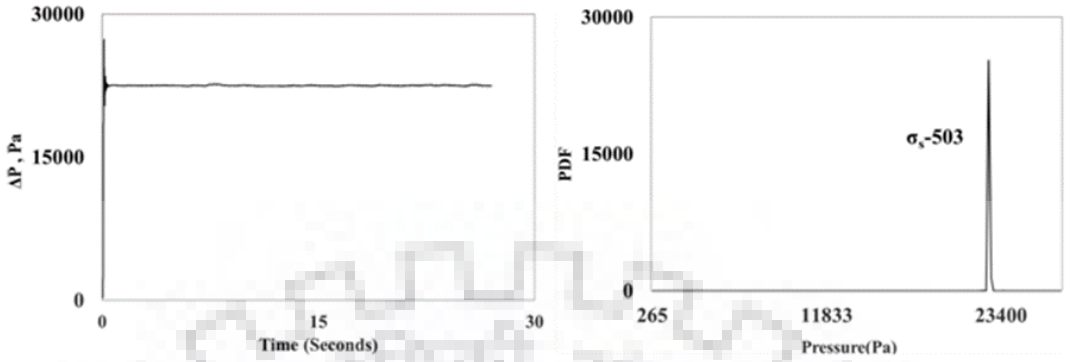

a) Annular Flow

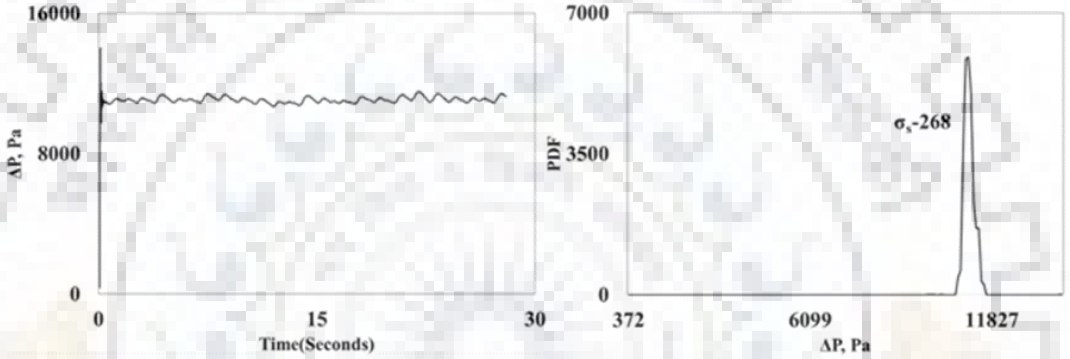

b) Wavy Annular Flow

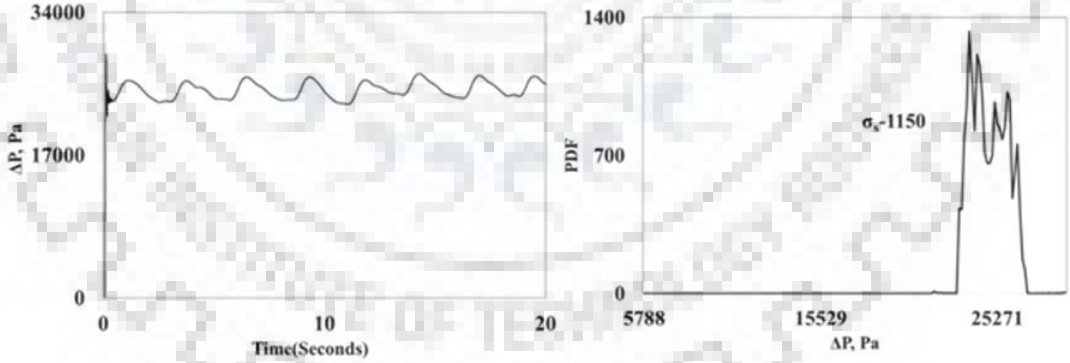

c) Slug Flow

Figure 3.9: Pressure Signal and corresponding PDF for T3

Similarly, Figure 3.9 shows a very sharp peak for annular flow and peak with larger standard deviation for wavy annular flow and slug flow.

Hence, it can further establish the chaotic nature of these flow regimes.

Next, the experimental pressure drop is normalized ($\Delta P(\mathrm{n})$) using velocity head of primary phase (air) as follows

$$\Delta P(\mathrm{n}) = \frac{\Delta P}{0.5\rho_G U_{GS}^2} \tag{3.9}$$

$\Delta P(n)$ is plotted as a function of liquid phase Reynolds number (Re_{LS}) for different gas phase Reynolds number (Re_{GS})for T1, T2 and T3 in Figure 3.10,3.11 and 12 respectively. Flow patterns are shown as different legends in both the figures. Following points are observed in both the figures:

- Figures show that, pressure drop increases with increase in Re_{LS} at a given Re_{GS} . This increase is very sharp and the magnitude of non-dimensional pressure is more for lower Re_{GS} .

- In case of T1, the pressure drop in horizontal is less than that of vertical orientation. It can be clearly seen from Figure 3.10. It gives a comparison of non- dimensional pressure for both the orientations at same Re_{GS} .

- Reverse is the case for T2 and T3. In this cases, vertical orientation shows lesser pressure drop. A steep rise of pressure is observed for Re_{GS_406} for T2 in horizontal orientation. However, more fluctuations in pressure are observed for Re_{GS_294} in horizontal orientation for T3.

- A comparison of Figure 3.10b (vertical orientation of T1) and Figure 3.12a (horizontal orientation of T3) further reveals that, the value of $\Delta P(n)$ for Re_{GS_338} in T1, is almost 4 times higher than that in T3 for Re_{GS_294} at Re_{LS_50}

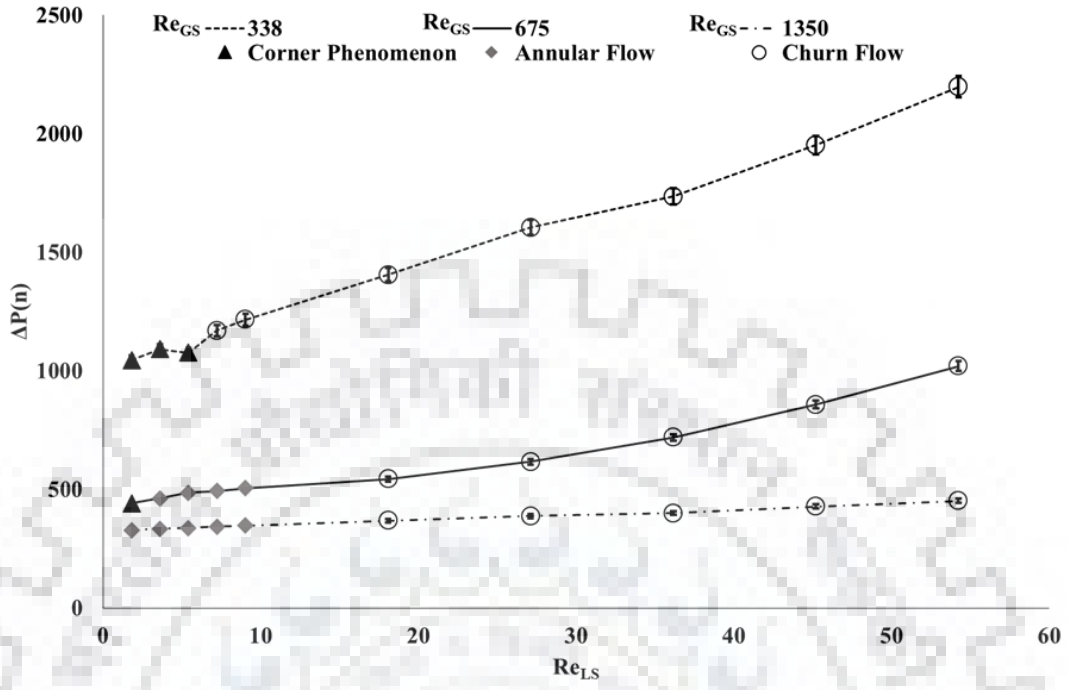

a) Horizontal

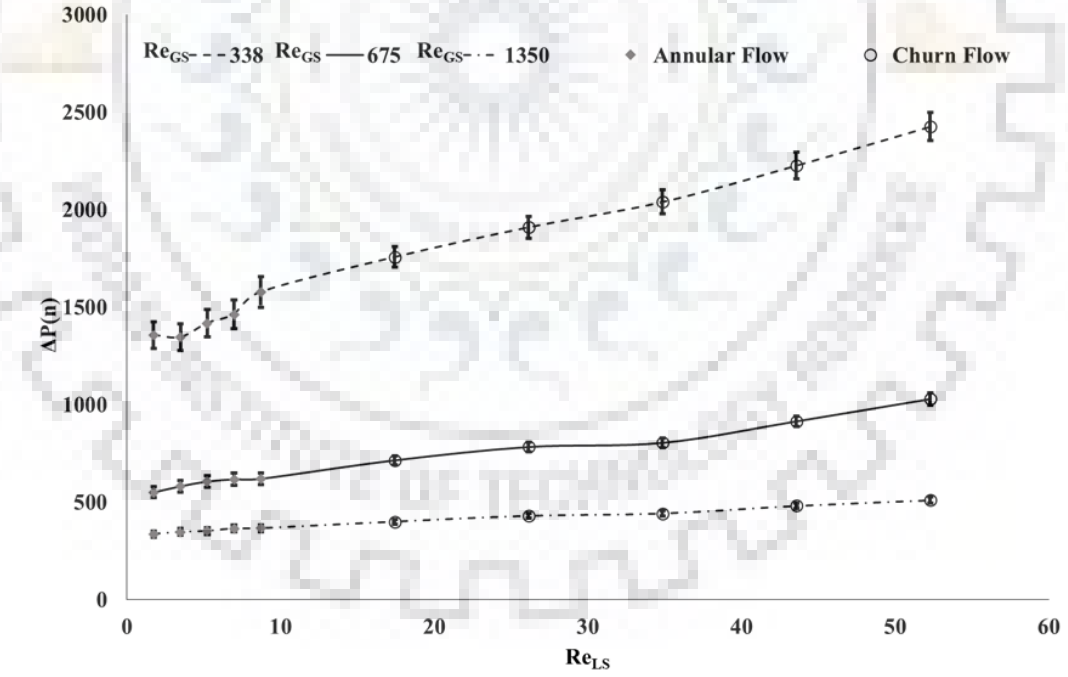

b) Vertical

Figure 3.10: Experimental pressure drop as a function of for Re_{GS} and Re_{LS} as parameter for T1

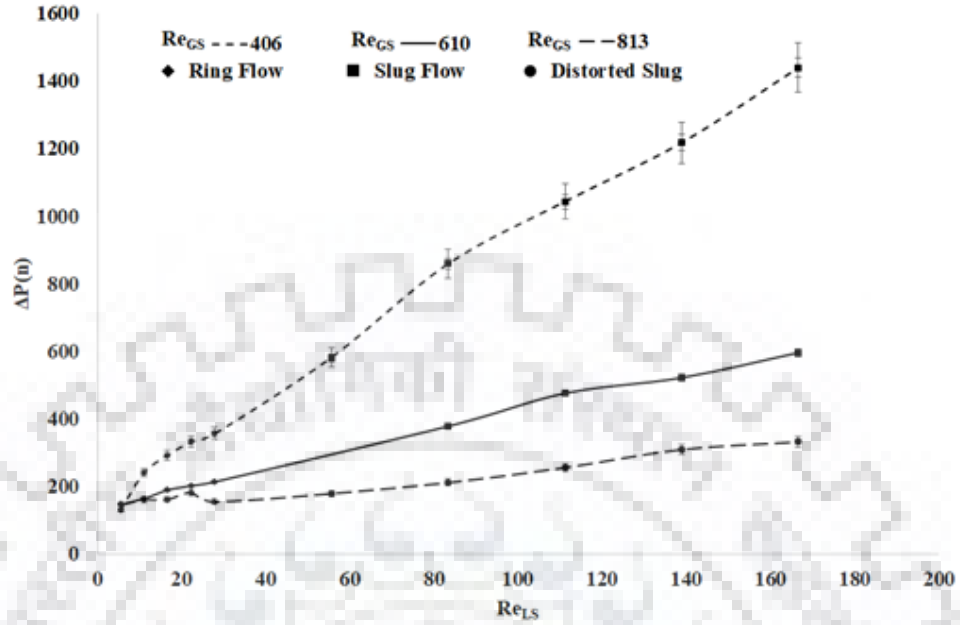

a) Horizontal

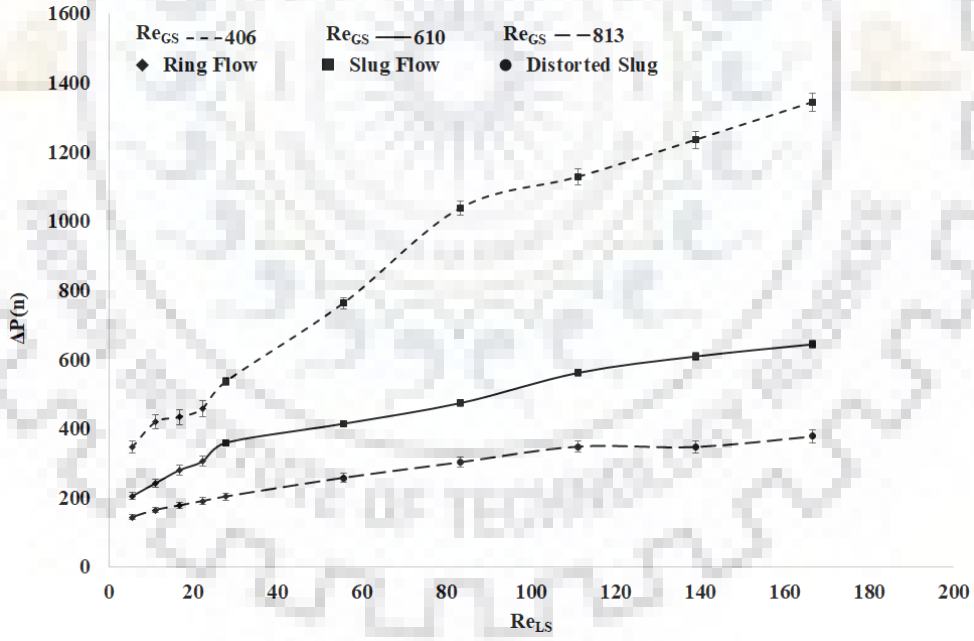

b) Vertical

Figure 3.11: Experimental pressure drop as a function of for Re_{GS} and Re_{LS} as parameter for T2

- Similarly, comparing Figure 3.11a (T2 and 3.12a (T3) at Re_{GS_406} at Re_{LS_50} reveals that T2 has 1.5 times higher pressure drop than T3.

- This indicates that vertical orientation of micro channel is desirable as it results in annular flow and drains out the liquid easily. It also actually offset the increase in frictional pressure drop due to reduction in hydraulic diameter. The reason may be attributed to increased capillary effect in vertical orientation**.**

- Further, attempts are made to understand the difference in pressure drop in vertical and horizontal orientation of T2 and T3. In order to understand the phenomenon, flow distributions at same Re_{GS} and different Re_{LS} are given in Figure 3.13 for horizontal orientations for T2.

- The Figure 3.14 depicts that there are irregular slug and large water pockets at Re_{GS_441} in horizontal orientation. This eventually results in mal distribution in downstream channels, thus increasing the pressure drop.

- On the other hand, at vertical orientation, small and regular slugs are noticed throughout the channels which reduce the water bridge length. As a result, pressure drop at vertical orientation lesser than that in horizontal. Similar observation is made for T3 also from Figure 3.14.

In case of two-phase flow in macro dimension, volume fraction measurement can be done using conductivity probe (Das et al. 2002, Mandal et al.2010, De et al.2010), conductance probe (Demori et al.2010, Strazza et al.2011) and quick closing valve technique etc. However, they are not relevant in the present case.

Therefore, a measurement technique based on image processing has been adopted in the present case. Details about image processing is discussed in chapter 2. In order to understand in a better way, time averaged volume fraction of water i.e. water coverage ratio (α_t) is estimated for Re_{GS_441} in both orientations for T3.

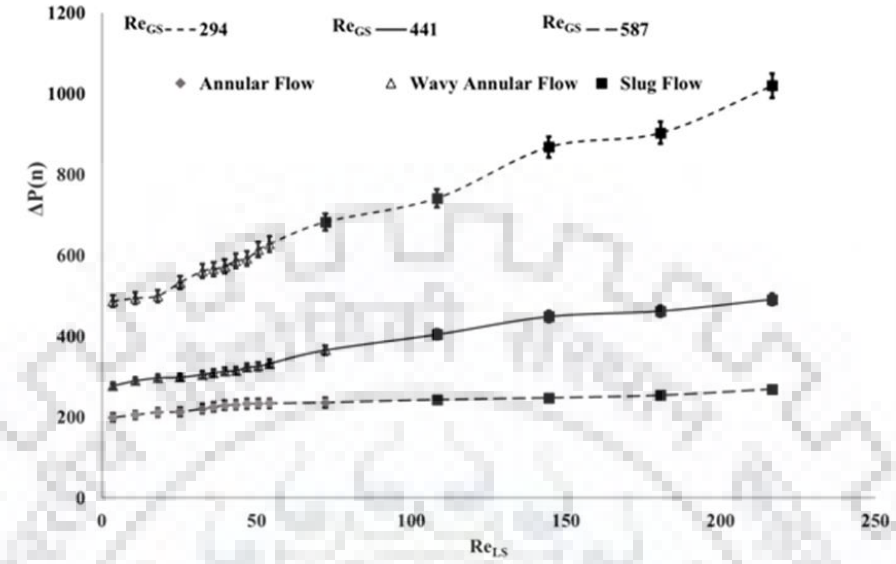

a) Horizontal

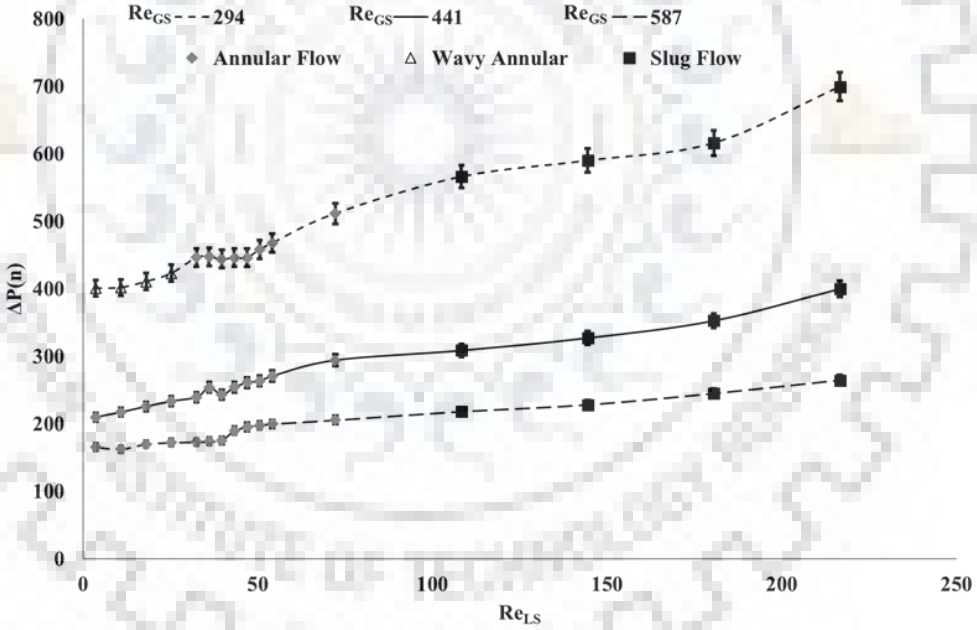

b) Vertical

Figure 3.12: Experimental pressure drop as a function of for Re_{GS} and Re_{LS} as parameter for T3

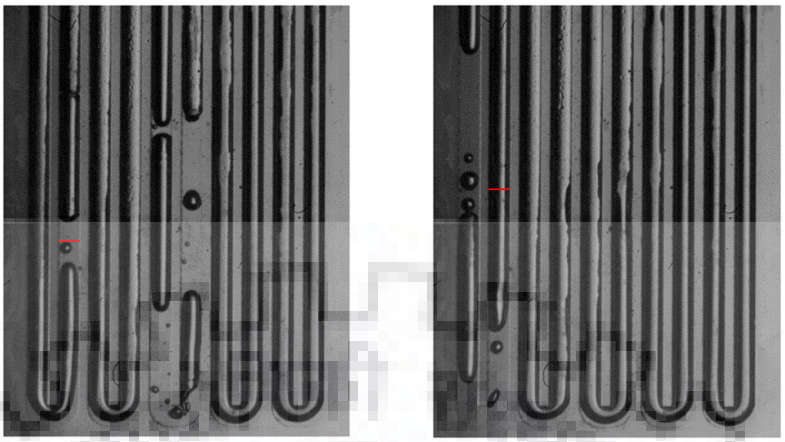

a) Re_{LS} = 5.5 b) Re_{LS} = 83.33

Figure 3.13: Flow distribution inside T2 at Re_{GS_200} in horizontal orientation for different Re_{LS} (length of bar 1 mm)

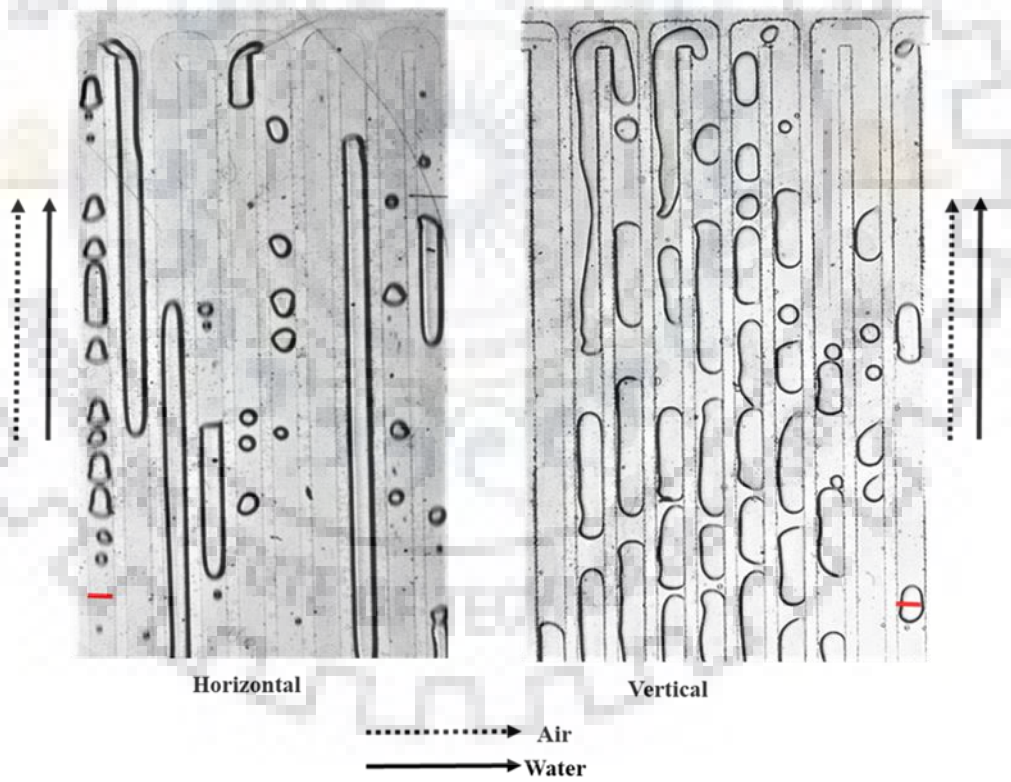

Figure 3.14: Flow distribution inside T3 at Re_{LS_144} and Re_{GS_440} (length of bar 1 mm)

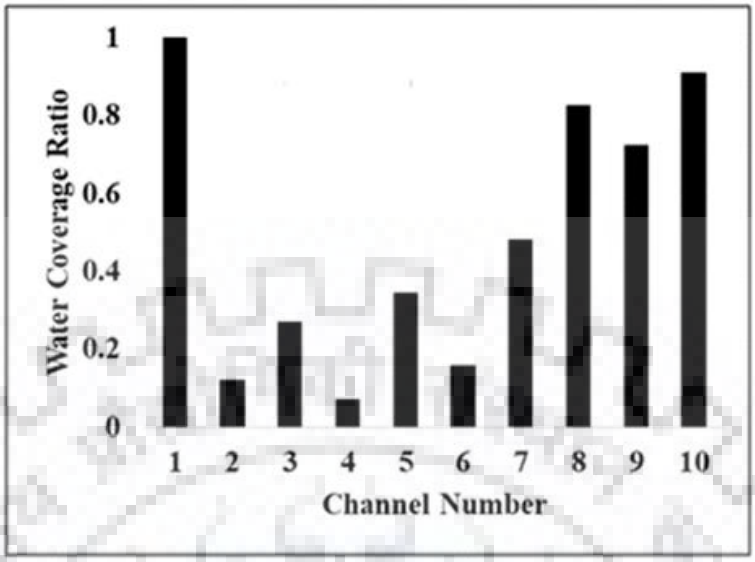

a) Horizontal

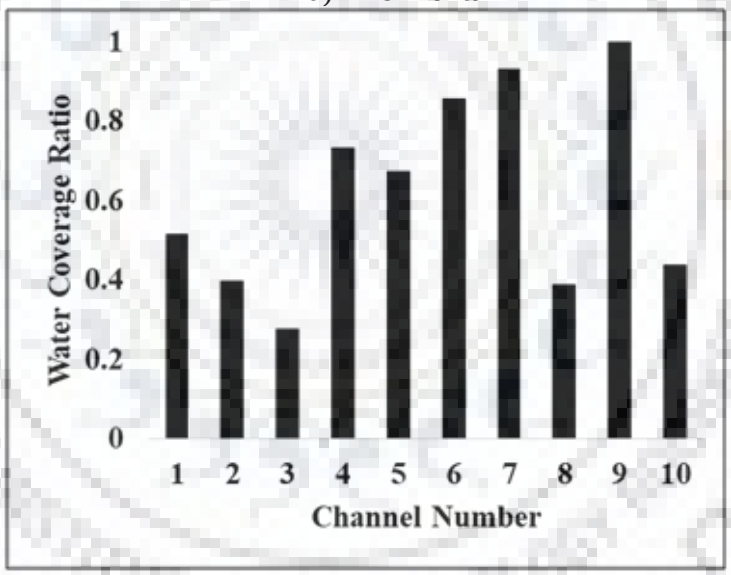

b) Vertical

Figure 3.15: Water coverage inside T3 at for Re_{GS_440} and Re_{LS_144} in both the orientations

Figure 3.15 shows the water coverage ratio (α_t) for both the orientations**.** It can be observed from the figure that, in horizontal orientation, majority of the channels are covered with more than 50% of water.

However, in case of vertical orientation, at least half of the channels have very less amount of water coverage. This leads to reduction in pressure drop in vertical orientation. This is in accordance with the finding of Ashrafi and Shams (2017) for a serpentine gas flow channels in an active fuel cell.

3.2.2. Various models used in pressure drop estimation

An interest is felt to establish analytical models to predict the experimental pressure drop. Homogenous and Separated Flow Model are used to predict the pressure drop for all flow patterns. These two models are widely tested by previous researchers (Choi and Kim 2011, Del Col et al. 2013) for predicting pressure drop in mini channels.

The total pressure drop in the test section can be given as

$$\Delta P = \Delta P_f + \Delta P_{hydro} + \Delta P_g \tag{3.10}$$

where, ΔP_f is the frictional pressure drop in the straight portions, ΔP_{hydro} is the pressure drop at return bend and ΔP_g is the gravitational effect. For all the cases the gravitational component is calculated and found in the range of 0.1% to 0.5% of total pressure drop measured by the transducers. Hence the effect of ΔP_g is taken to be negligible.

a) **Homogenous Model**: In the present study, the homogenous model is used to estimate the frictional pressure gradient for mixed flow patterns. The model assumes no slip between the phases and predicts frictional pressure gradient using mixture properties as:

$$\Delta P_f = \frac{2 f_m L \rho_m U_m^2}{D_H} \tag{3.11}$$

where f_m is obtained based on mixture Reynolds number as

$$f_m = \frac{14.2}{\mathrm{Re}_m} \text{ for laminar flow} \tag{3.12}$$

$$f_m = 0.079(\mathrm{Re}_m)^{-0.25} \text{ for turbulent flow} \tag{3.13}$$

and mixture Reynolds number (Re_m) is defined as:

$$\mathrm{Re}_m = \frac{D_H U_m \rho_m}{\mu_m} \tag{3.14}$$

where D_H being the pipe diameter and ρ_m is the mixture density

$$\rho_m = \rho_G(1-\beta_L) + \rho_L \beta_L \tag{3.15}$$

μ_m is the mixture viscosity expressed in terms of the individual viscosities of gas (μ_G) and liquid (μ_L):

$$\mu_m = 1/(\frac{1-\beta_L}{\mu_G} + \frac{\beta_L}{\mu_L}) \tag{3.16}$$

$$U_m = U_{GS} + U_{LS} \tag{3.17}$$

For a 10 mm diameter pipe as discussed by Sharma et al. (2011) ΔP_{hydro} can be written as

$$\Delta P_{hydro} = \frac{\Delta P_f}{L} L_b + \Delta P_{Bend} \tag{3.18}$$

$\frac{\Delta P_f}{L} L_b$ accounts for the equivalent frictional losses in the bend length and ΔP_{Bend} is the pressure drop due to change in direction.

For single phase flow of water in return bend ΔP_{hydro} can be estimated through loss coefficient, $\Delta P_{hydro(w)} = k_w \frac{1}{2} \rho_w U_{sw}^2$ (3.19)

k_w is the bend loss coefficient for single-phase water flow.

Idelchik (1996) estimated k_w in case of 180^0 U bend as:

$$k_w = f \frac{L_b}{D} + 0.294(\frac{R}{D})^{0.5} \quad (3.20)$$

with, R is the radius of curvature of the bend and f is the single-phase friction factor.

For the recent case the final equation of pressure drop in test section having nine 180^0 U bend estimated as

$$\Delta P_{Predicted} = \frac{2 f L \rho_m U_m^{\ 2}}{D_H} + 9 * k_w \frac{1}{2} \rho_m U_m^{\ 2} \quad (3.21)$$

This pressure is normalized ($\Delta P(\mathrm{n})_{Predicted}$) using velocity head of primary phase (air) as follows

$$\Delta P(\mathrm{n})_{Predicted} = \frac{\Delta P_{Predicted}}{0.5 \rho_G U_{GS}^{\ 2}} \quad (3.22)$$

Mean absolute Error as defined by Choi and Kim (2011) is estimated as

$$MAE = \frac{1}{M} \sum \left[\frac{\left| \Delta P(n) - \Delta P(n)_{predicted} \right|}{\Delta P(n)} \times 100 \right] \quad (3.23)$$

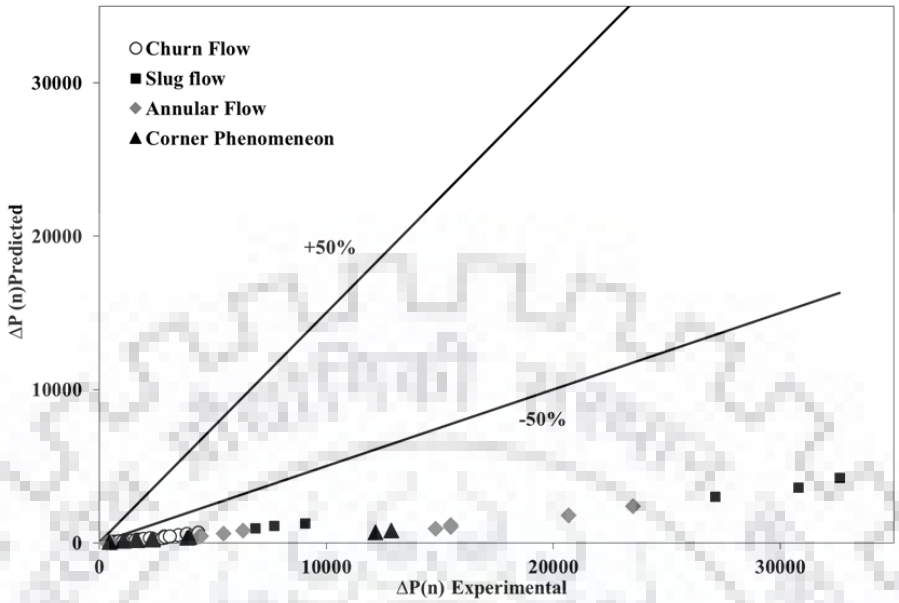

a) Horizontal

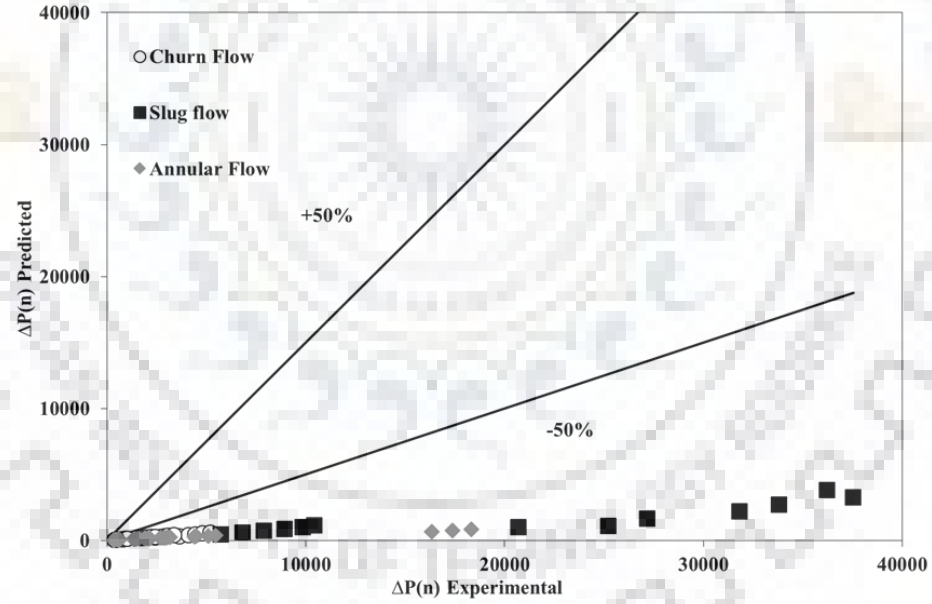

b) Vertical

Figure 3.16: Prediction of experimental pressure drop in both the orientation using homogenous model and Fanning's friction factor for T1

The value of MAE in horizontal orientation is 55% and that in vertical orientation is 65%. As the gravitational component is very small, addition of static head didn't reduce the error. Figure 3.16 shows that, the predictions of equations (3.25) with experimental data for T1 in both orientations. It shows that prediction deviate more than $\pm$ 50%. Similar results are obtained for other test sections.

b) Separated Flow Model: This model is based on two-phase flow multiplier as

$$\phi_L^2 = \frac{\left(\frac{\Delta P}{\Delta Z}\right)_{TP}}{\left(\frac{\Delta P}{\Delta Z}\right)_L} \tag{3.24}$$

where ϕ_L^2 can be obtained from Martinelli parameter as suggested by Lockhart and Martinelli (1949) as

$$\phi_L^2 = 1 + \frac{C}{X} + \frac{C}{X^2} \tag{3.25}$$

$$X = \sqrt{\frac{\left(\frac{\Delta P}{\Delta Z}\right)_L}{\left(\frac{\Delta P}{\Delta Z}\right)_G}} \tag{3.26}$$

where X is defined as ratio of liquid only and gas only pressure drop.

The value of MAE in horizontal orientation is 41% and that in vertical orientation is 35%. Figure 3.17 shows prediction of non-dimensional pressure using separated model with experimental data for T1 in both the orientations. It shows that prediction deviate more than $\pm$ 50%. Similar results are obtained for other test sections.

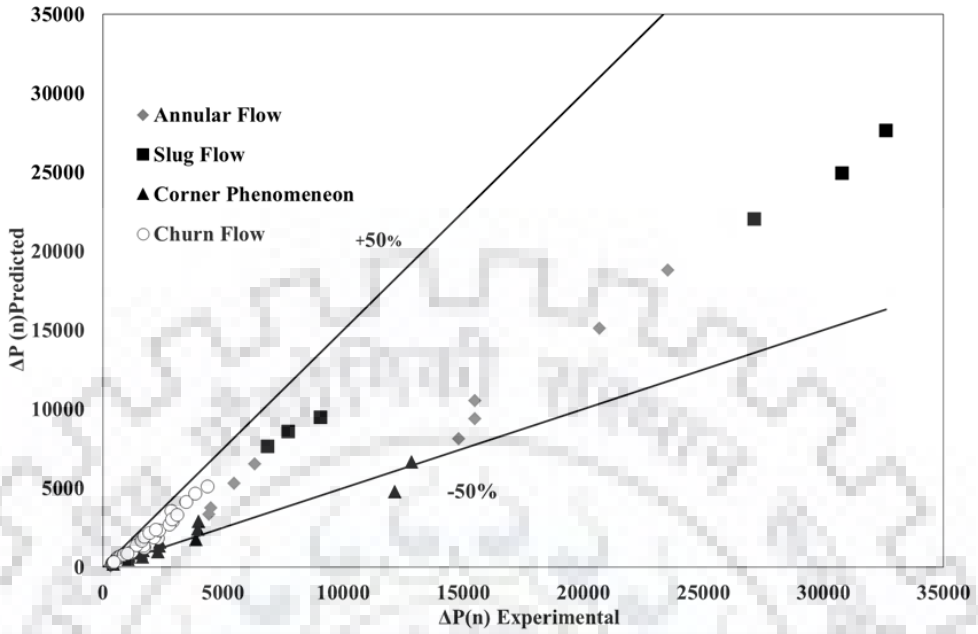

a) Horizontal

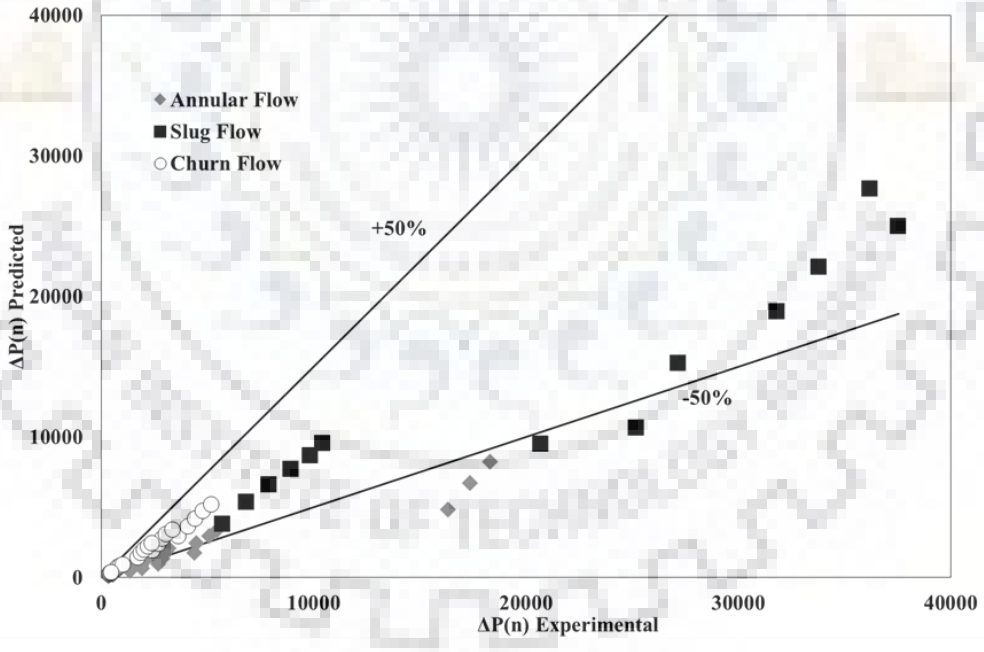

b) Vertical

Figure 3.17: Prediction of experimental pressure drop in both the orientation using separated flow model for T1

c) Model based on modified friction factor

It may be noted that the large mismatch reported above is in agreement with some recent studies of air water in miniature geometry. Hence, it can be said that a proper estimation of friction factor is necessary for these cases. Donaldson et al. (2011) suggested, bend friction factor is a function of Reynolds number as well as Capillary number ($Ca_{LS} = \frac{\mu_L U_{LS}}{\sigma}$) for miniature channels unlike in conventional geometries where friction factor is a function of Reynolds number only. Taking a clue from this in the present study the friction factor is estimated as function of two dimensionless numbers. In the present work, the friction factor is estimated as

$$f = \frac{C}{(\mathrm{Re}_m \, Ca_{LS})^n} \tag{3.27}$$

where, C and n are constants

This modified friction factor is used with homogenous model in order to predict the pressure drop. For current study, pressure drop data of T1, T2 and T3, and in both orientations are considered. Figure 3.18 shows the variation of experimental friction factor $f_{\exp}$ with $\mathrm{Re}_m \, Ca_{LS}$ for both orientations.

A best fit curve of experimental points gives the value of C and n as 0.93 and 0.78 for horizontal and 1.4 and 0.85 for vertical orientation. Using these best fit values, MAE in horizontal orientation is obtained as 59.11% and that in vertical is 29.7%. Hence, in order to reduce the MAE further, flow regimes are examined separately. The experimental data is further divided on the basis of flow regimes and tested separately. This results in following combinations of C and n

- For vertical orientation, C ranges from 1.2 to 2 and n from 0.8 to 1.
  Annular and churn C value is 1.95 and n is 0.9. For slug and distorted slugs C is 0.76 and n is 0.8. In case of ring C value is 1.4 n is 0.85.
- In case of horizontal orientation, the values are as follows

Corner phenomenon, C 1.3 n 0.6

Annular and wavy annular flow C 0.92 n 0.7, Ring flow C 0.25 n 0.55

Churn flow C 2.5 n 1.0, Slug and distorted slug for ring, C 0.33 n 0.7

This demarcation based on flow regime irrespective of diameter reduces the MAE to 15% in horizontal orientation and 19% to vertical orientation**.** Figure 3.19 shows the prediction of non-dimensional pressure drop using equation (29). It can be seen the pressure drop can be predicted within $\pm$ 25% in both orientations for, T1, T2 and T3

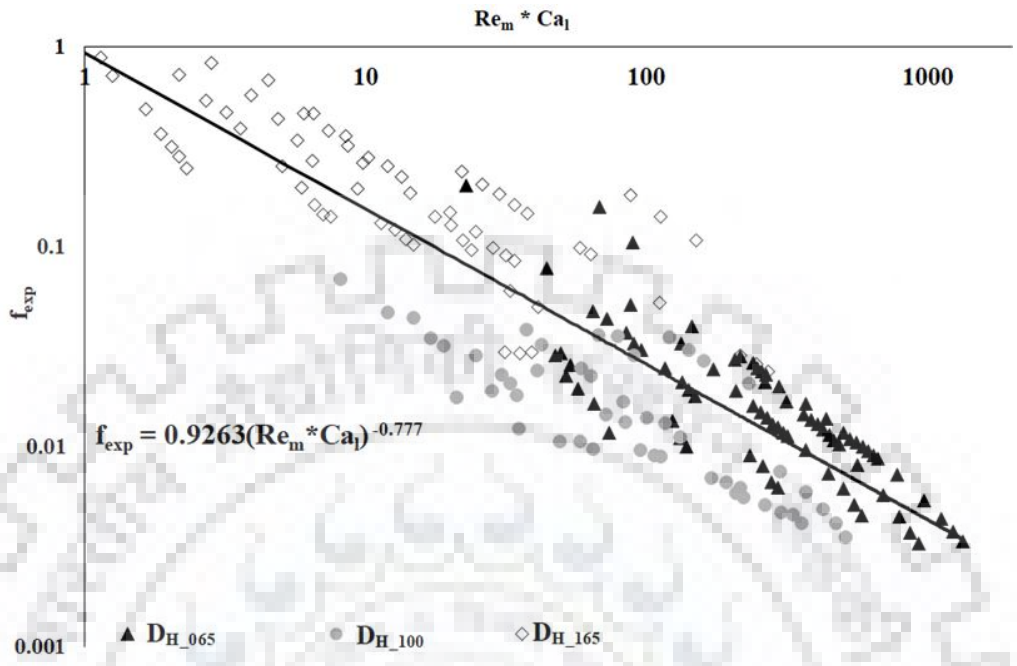

a) Horizontal

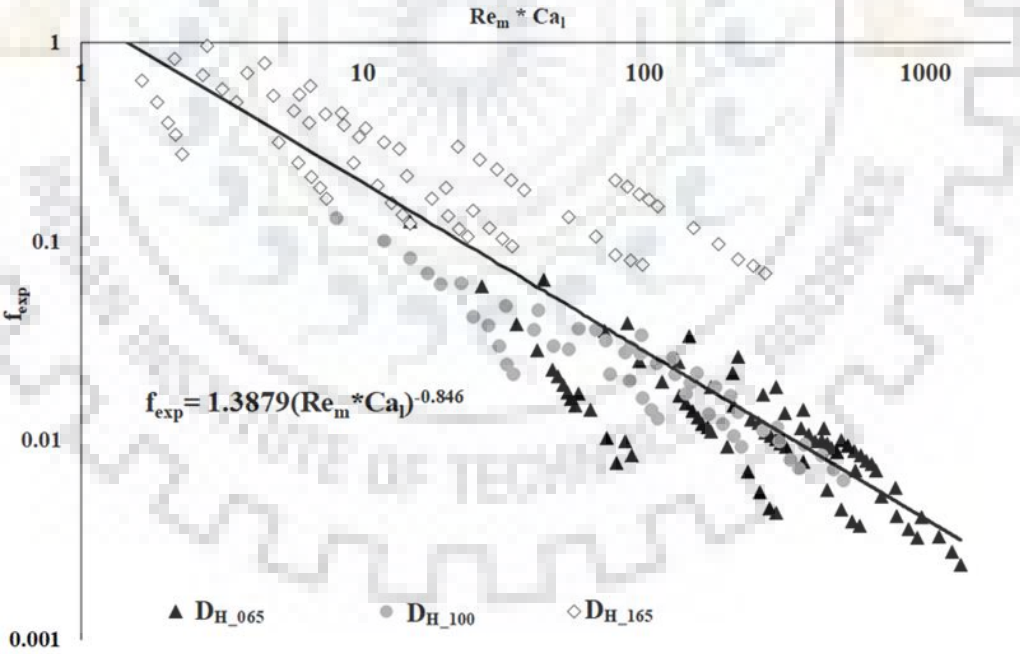

b) Vertical

Figure 3.18: Prediction of modified friction factor in both the orientation T1, T2 and T3

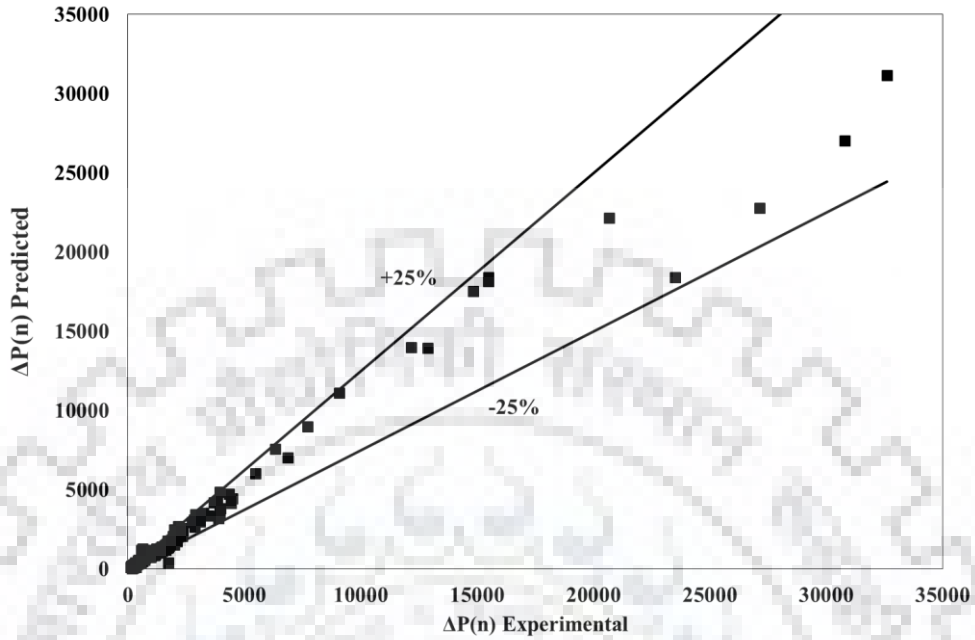

a) Horizontal

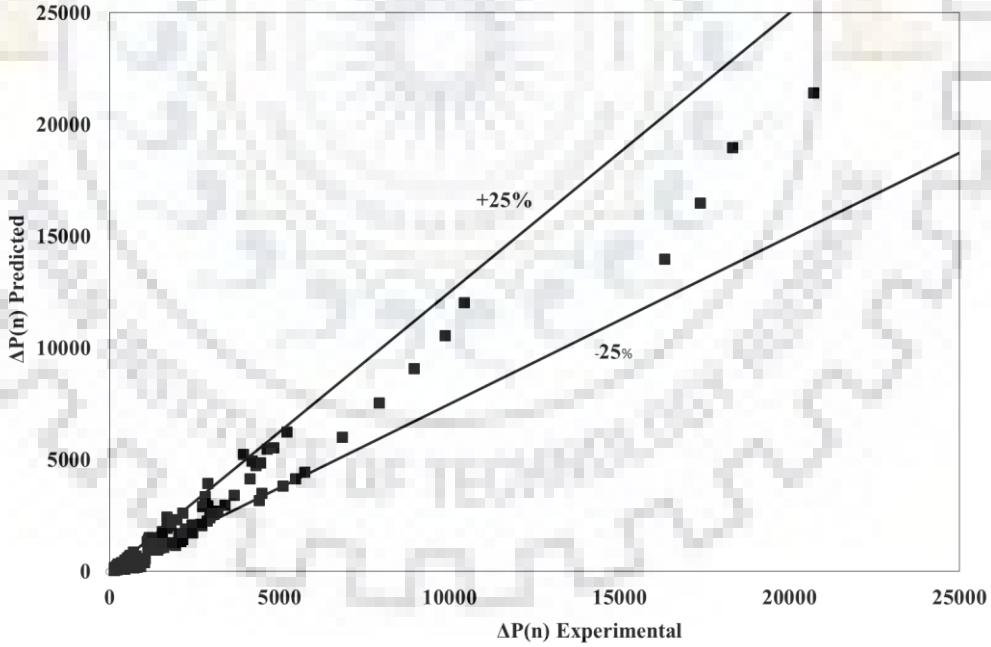

b) Vertical

Figure 3.19: Prediction of experimental pressure drop in both the orientation using modified friction factor for T1, T2 and T3

CHAPTER 4 NUMERICAL INVESTIGATION OF AIR WATER FLOW

In the previous chapter, different phase distributions of air-water two-phase flow through serpentine channels of different hydraulic diameter and bottom wall contact angle are discussed. Though various flow patterns are reported in the previous chapter. It can be noticed that the slug flow in T2 and T3 test section causing maldistribution which leads to higher pressure drop. An interest is felt to investigate the role of wettability gradient in order to remove water easily in these situations, therefore reducing the maldistribution. However, it is difficult to create the wettability gradient and carry out repeated experiments in present experimental situation. This leads to numerical investigation of the same. Before simulating the actual situations, some test cases are simulated with drop in a U-shaped geometry. In the test cases, at first bottom wall at downstream after the bend is modified for removal of suspended drop. This is done to understand if the drop is scattered at adhered at the bend, which type of gradient (positive or negative) are effective of its removal. Later a combination of hydrophilic and phobic gradient is applied at upstream and downstream of the U-shaped geometry. This is termed as combined gradient. Finally, large amount of water is introduced through inlet at the U-shaped geometry and the effect of combination gradient is seen on the water coverage. Commercial CFD software FLUENT 16 [27] is used for the simulation.

4.1. Numerical model

3D numerical models have been developed using commercial software to study air-water flow U shaped geometry. Finite volume technique is used to discretize the governing equations with suitable discretization schemes for each equation. After the discretization, the governing equations are solved by using the segregated solver. The computation has been done for unsteady flow to investigate the initial development of air-water distribution. The salient assumptions include unsteady flow, immiscible fluid pair, and constant fluid properties

Three different broad situations are simulated. First case to decide which type of surface is suitable for removal of suspended drop, followed by realistic situations observed in T1. All these situations are shown below with corresponding geometry

a) Suspended drop and single modified bottom wall

Figure 4.1 schematically represents the flow geometries. A single serpentine U-shaped geometry is considered for the simulation. The dimension of the geometry of the gas channel is shown in Figure 4.1. It is a serpentine channel with square cross-sectional section of 1 mm^2. In the present case the length of each arm of the channel is taken to be 0.02 m. Air and water are used as test fluids. Two different cases are simulated with single drop of different volume. It is assumed that the drops are suspended in the channel. As discussed by Quan (2005) that such drops are often scattered at bend and removal is difficult from the bend. Hence, effect of modified wettability of GDL surface after bend is explored

b) Drop on bottom surface for a combined modified bottom surface

The dimensions of the computational geometry have been the same as previous case. The difference lies in the fact that the drop is on bottom surface 2 mm from the inlet (Figure 4.2). The gradient is applied both at the upstream and downstream bottom surfaces. In case of upstream surface, the gradient is negative w.r.t direction of flow. In case of downstream surface, it is positive w.r.t direction of flow (Figure 4.3). This makes the surface hydrophilic for upstream and hydrophobic for downstream. In figure 4.2 it has been highlighted in different colors, the red one indicating bottom surface 1 and green color indicating bottom surface 2.

c) Slug flow in a U bend

This situation is typically representing the slug flow regime of T2 test section in chapter 3. One of the air water flow combination has been selected and

simulated with different surface characteristics exhibited in bottom wall. This is represented in figure 4.4. Water is introduced at the inlet.

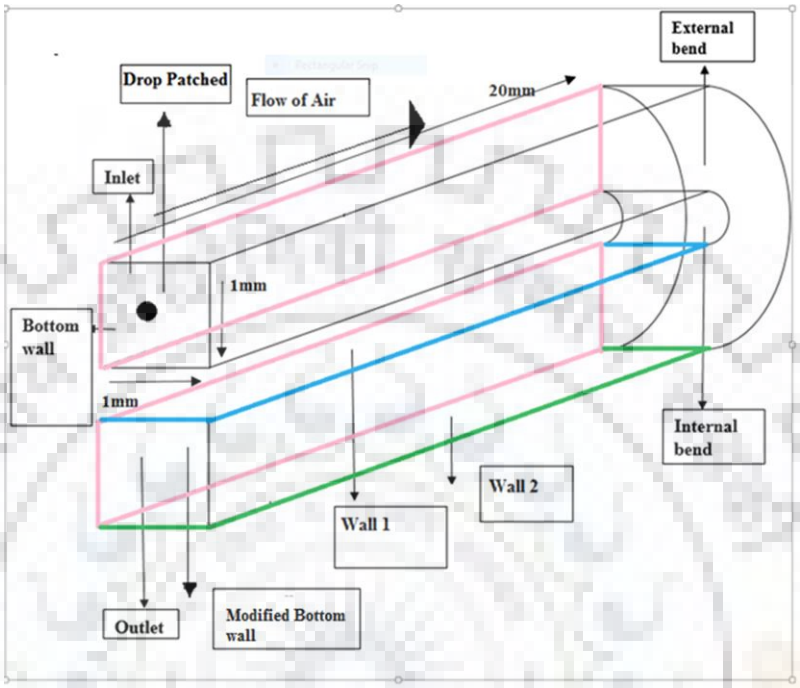

Figure 4.1: Schematic of computational domain for suspended drop

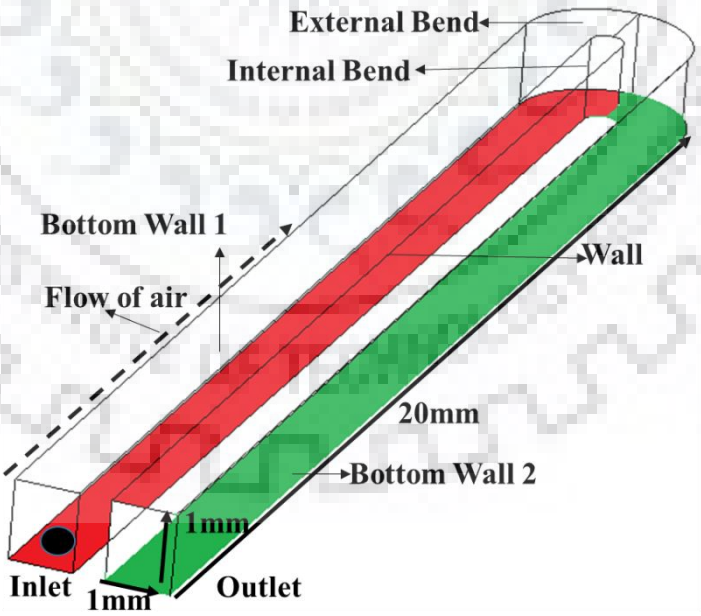

Figure 4.2: Schematic of computational domain for drop attached to bottom wall

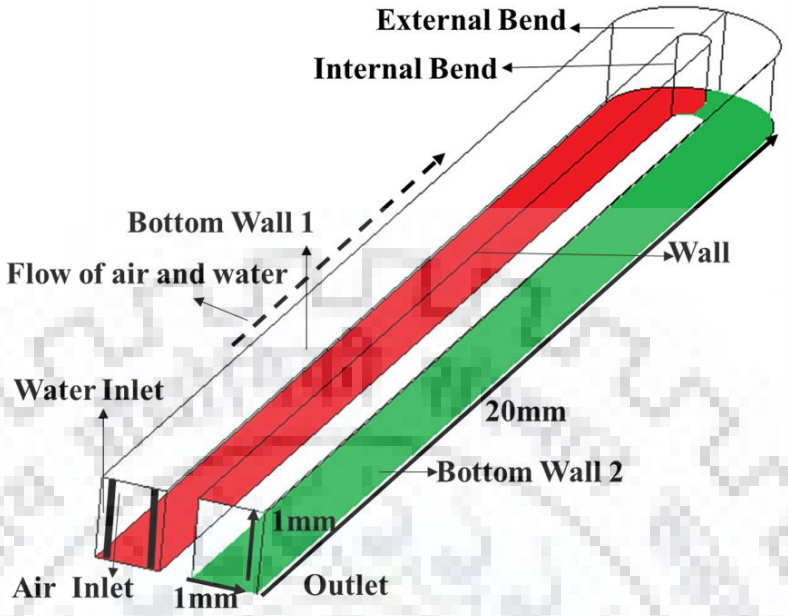

Figure 4.3: Schematic of computational domain for slug flow

a) GDL with wettability gradient

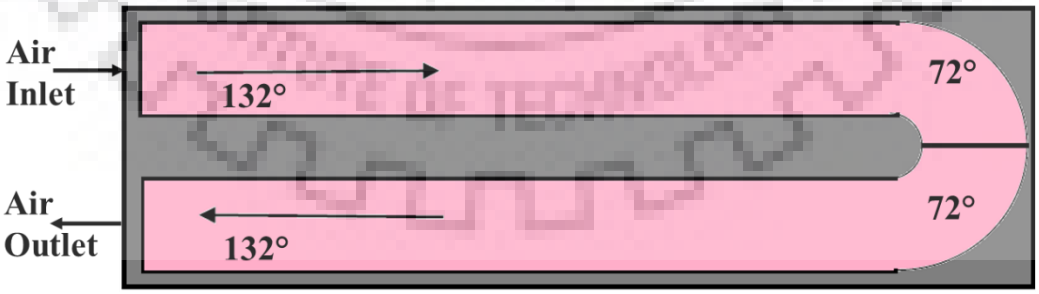

b) GDL as bottom surface of the channel

Figure 4.4: Schematic representation of modified bottom surface

4.1.1. Governing equations

In present study, movement of water drop in presence of varied air velocity were simulated. The interface between the water and air is very distinguishably identified. There are few algorithms available for interface tracking in case of multiphase flow. Among those widely used is Eulerian-Eulerian based Volume of Fluid VOF. This method is used widely by researchers both for microfluidic devices (Saha and Mitra 2009) as well as macro dimension (Gueyffier 1999). Another widely used method is Level set (Gada and Sharma 2009, Datta et al.2011). Apart from these Lattice Boltzmann method (Gunstensen et al. 1991, Rothman and Zaleski 1994, Kumar et al. 2008 and Ghosh et al. 2012). In the present study VOF is used. In case of VOF a single set of momentum equation is shared by both air and water. The interface is reconstructed from the information of volume fraction of each phase in a particular computational cell. The governing equations used in the present study are as follows:

Continuity:

$$\frac{\partial(\rho)}{\partial t} + \nabla.(\rho U) = \sum_{q} S_q \tag{4.1}$$

where, ρ ,U , α , t, S are density, velocity, phase fraction, time and mass source respectively. In the present case S is zero.

Momentum:

$$\frac{\partial(\rho U)}{\partial t} + \nabla.(\rho U.U) = -\nabla P + \nabla.\left[\mu\left(\nabla U + \nabla U^{T}\right)\right] + (\rho g) + F \tag{4.2}$$

where, P, g, F, μ are pressure in the flow field, acceleration due to gravity, surface force acting on the system and viscosity of the flow system respectively.

Density and viscosity used in previous equations can be estimated as:

$$\rho = \rho_1 \alpha_1 + \rho_2 (1 - \alpha_2) \tag{4.3}$$

$$\mu = \mu_1 \alpha_1 + \mu_2 (1 - \alpha_2) \tag{4.4}$$

where, α_1 is volume fraction of phase 1(air), ρ_1 is the density of phase 1 and ρ_2 is that of phase 2 (water), μ_1 is the viscosity of phase 1 and μ_2 is that of phase 2 (water), As mentioned earlier for reconstruction of the interface, a separate continuity equation for α considered as follows

$$\frac{\partial \alpha_1}{\partial t} + (U_1 . \Delta) = S_{\alpha 1} \tag{4.5}$$

The VOF model includes the effects of surface tension along the interface between the phases. The surface tension model uses the continuum surface force (CSF) model. In this model, the addition of surface tension to the VOF calculation results in a source term in the momentum equation

$$F = \sum_{ij} \sigma_{ij} \frac{\alpha_i \rho_i \kappa_j \nabla \alpha_j + \alpha_j \rho_j \kappa_i \nabla \alpha_i}{\frac{1}{2}\left(\rho_i + \rho_j\right)} \tag{4.6}$$

The curvature, κ, is defined in terms of the divergence of the unit normal, n

$$\kappa = \nabla . n \tag{4.7}$$

$$n = \frac{n}{|n|} \tag{4.8}$$

n is the surface normal defined as the gradient of α_a. According to ANSYS FLUENT theory guide, n is expressed mathematically as:

$$n = \nabla \alpha_a \tag{4.9}$$

For present system

$$\kappa_a = -\kappa_w \text{ and } \nabla \alpha_a = -\nabla \alpha_w \tag{4.10}$$

This modifies equation (4.6) as:

$$F = \sigma_{aw} \frac{\rho \kappa_a \nabla \alpha_a}{\frac{1}{2}(\rho_a + \rho_w)} \tag{4.11}$$

where ρ is the volume-averaged density computed using equation (4.3).The above equation shows that the surface tension source term for a cell is proportional to the average density in the cell.

4.1.2. Boundary condition:

Inlet boundary condition

In all cases, velocity of the air is defined at the entry of the channel. In case of slug flow, water is introduced at the inlet though an annular portion with dimension 0.8 mm× 0.8 mm.

Outlet

At the exit of the channel, pressure outlet boundary is used.

Wall Boundary: Wall boundary conditions are different for suspended and attached drop cases as discussed below.

a) Suspended drop case: In this case, apart from the GDL surface, which is the bottom surface of the channel after the bend all the walls are defined as the stationary walls having a constant contact angle. As mentioned earlier that Quan et al. (2005) noticed that the deformed drop adheres to the bend after bend section. Taking a clue from them the GDL surface after the bend treated differently. Two different

types of GDL surfaces are considered. a) Gradual hydrophilic surface with contact angle changes from 90˚ to 10˚ having a gradient of 4˚ mm^{-1}. b) Gradual hydrophobic surface with contact angle changes from 90˚ to 170˚ having a gradient of + 4˚ mm^{-1} is specified. These surfaces are termed as surface A and B respectively. For these cases separate User Defined Function has been incorporated at the wall boundary.

b) Drop attached on bottom surface and slug flow: As observed from the suspended drop case that surface B is more effective in removal of water from downstream of bend, so in these cases only surface B has been used. However, the gradient varied. Also, these cases are simulated for drops adhered to the bottom surface of inlet, hence, upstream surface wettability are taken into consideration. Figure 4.3 shows a detailed schematic of the contact angle gradient for GDL surface. Three different gradients of 3°/ mm, 4°/ mm, 5°/ mm are used for present work. Apart from the GDL surface, which is the bottom surface of the channel after the bend all the walls are defined as the stationary walls having a constant contact angle of 72°.

4.1.3. Numerical Scheme

The coupled scheme PISO algorithm is applied for pressure velocity coupling. This scheme accommodates larger time steps efficiently thus found to be more suitable for the studies. The flow phenomenon is dynamic in nature, both in terms of time and space. The PRESTO (Patankar 1980) algorithm has been used to discretize continuity equation, while momentum equation is discretized by first order upwind method.

4.1.4. Meshing of the model

A total of 260945 cells were used in the model. In order to capture the boundary layer, the grid was made very fine at the surfaces and started to coarsen as it moved away from the walls. Rigorous grid independence tests have been performed for all the problems. The above grid arrangements have been selected based on those tests. Meshed geometry is shown in Figure 4.5. The meshed geometry for slug flow in hydrophilic bend is show in Figure 4.6. This consists of 130986 cells. The meshing is

purposefully kept fine in the downstream area because the deformation of the drop starts after the bend. As the water removal is of interest hence downstream region is refined exhaustively.

The time step of $5x10^{-8}$ seconds was used for two phase case. The Courant number was kept between 0.01 - 0.1 and the simulations were run for 50 - 300 ms. The real run-time of the simulation varied between 7 – 10 days. The simulation is said to be converged if the values of residuals of mass, velocity, volume fraction etc. are below 0.001. Figure 4.7 shows the typical convergence history for a specific case. It depicts the residuals are well below the limit set for convergence.

Figure 4.5: Meshed geometry for drop cases

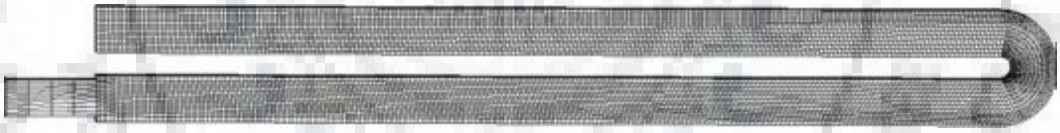

Figure 4.6: Meshed geometry of slug flow

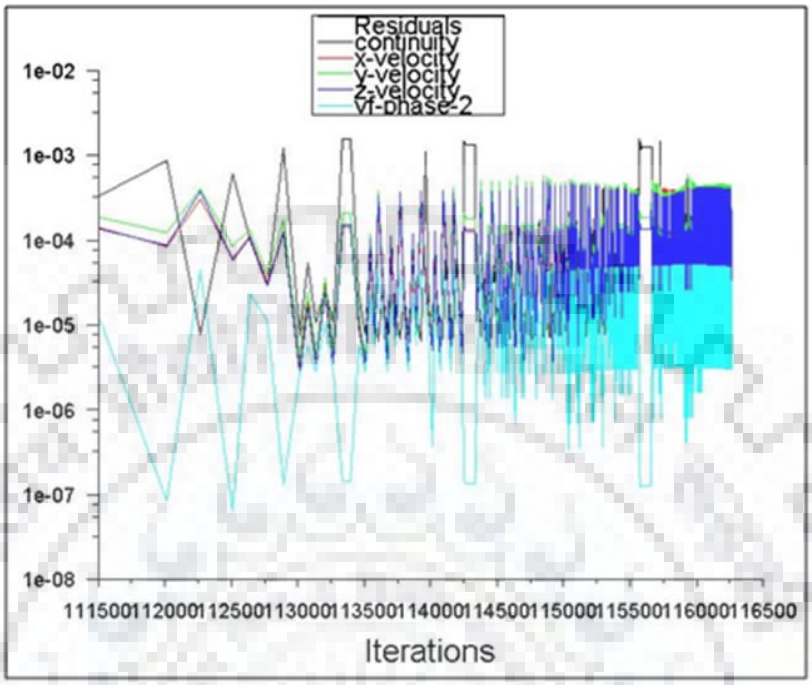

Figure 4.7: Convergence Details

4.2. Validation of models

In the present case, the model is validated against literature for constant contact angle and against experiments.

a) **Validation of stationary drop against literature:** In order to check the model two stationary drops are considered. First one with a volume of 1.75 mm^3 is placed on a hydrophilic surface. Young's equation for equilibrium contact angle and that measured from contour is 83°. Its equilibrium shape is compared with simulated profile that reported by Iliev (1997) (Figure 4.8a). Second drop is simulated with volume of 2 mm^3 placed on a hydrophobic surface. In this the contact angle is 139°. Its shape is compared with experimental contour that reported by Zhenyu et al. (2016) in Figure 4.8b. In both the cases, it shows good matching with the literature.

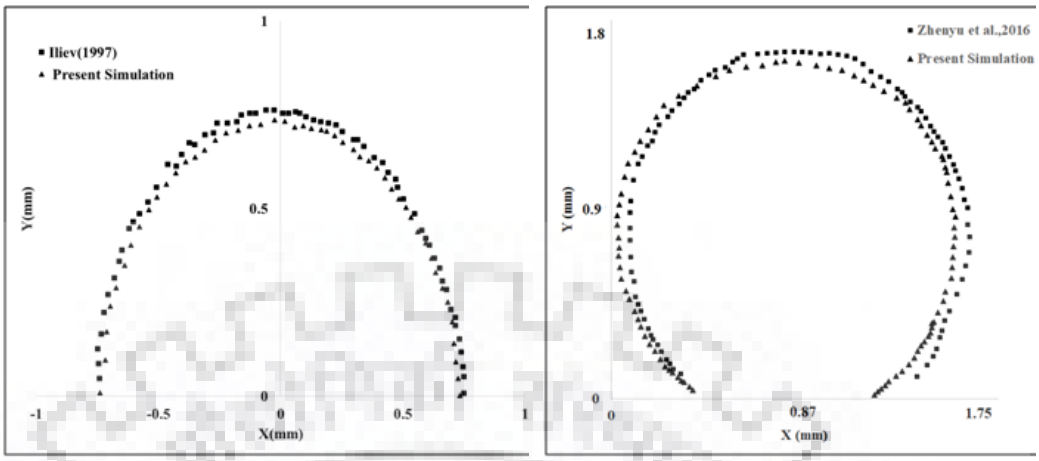

a) Hydrophilic surface with contact angle 83°

b) Hydrophobic surface with contact angle 139°

Figure 4.8: Comparison of stationary drop on hydrophilic and hydrophobic surface with literature

b) Validation with existing experimental setup: Further simulations are performed with water drop along air is moving inside a serpentine channel. Additional experiments are performed in a single U-shaped serpentine channel with square cross section of 1 mm^2 and a length of 20 mm. Water was injected inside the channel by using 10 mm^3 glass syringe. Three different volumes of water are injected 4 mm^3, 5 mm^3 and 6 mm^3. In order to validate the simulation, air flow rate is kept constant at 0.6 LPM which corresponds to an air velocity (U_g) of 10 m/s.

c) The photographs are studied using Image J software to estimate water film thickness at the downstream of bend. The comparison between numerical and experimental images has been shown in figure 4.9

Initially simulations are carried out for walls of uniform constant contact angle with air velocity of 10m/s and water volume of 4 mm^3, 5 mm^3 and 6 mm^3. Photographs are compared with the contours obtained from simulation are show in Figure 4.9. It shows good resemblance between the two. Water film thickness obtained from simulation and experiments are measured using a image processing

software Image J. This comparison is shown in Table 4.1. Further the pressure drop noted from the experiment and numerical pressure drop are compared in Table 4.2. It is noticed that the model over predicts the experimental data over predicts experimental one within 13%.

Table 4.1 Water Film Thickness Validation

Volume (mm^3)	Water Film Thickness (mm)	
	Experimental	Simulation
4	0.178	0.155
5	0.179	0.184
6	0.185	0.195

Table 4.2 Pressure Drop Validation

Volume (mm^3)	Experimental ΔP(Pa)	Simulation ΔP(Pa)
4	631.6	584.7
5	658.6	585.2
6	673.5	585.6

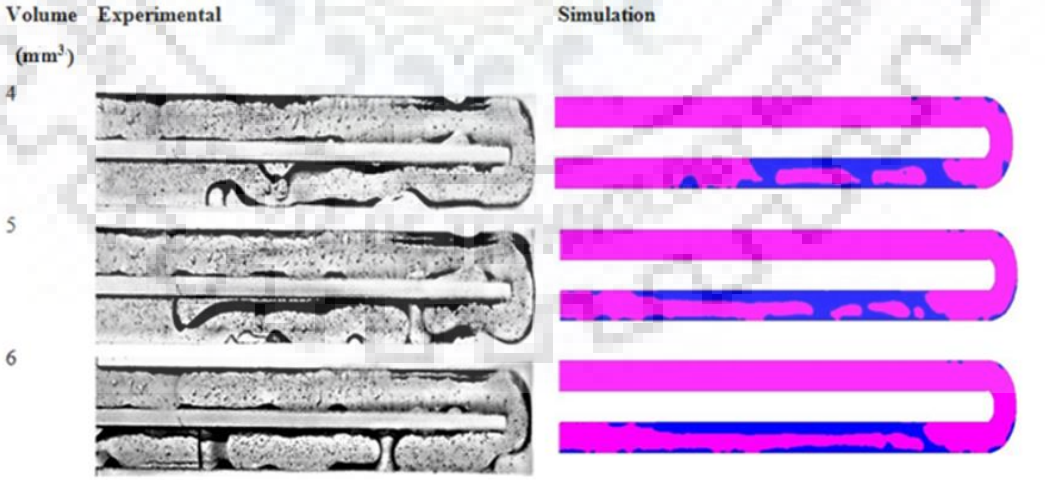

Figure 4.9: Comparison of experimental and numerical phase contours

4.3. Single suspended drop

In case of experimentation also it is noted that after the water volume entered the bend, they are difficult to remove from downstream. Hence, GDL surface after the bend is modified. This particular surface is denoted by modified bottom surface in Figure4.1. Contact angle of this surface now become a function of flow direction with a constant gradient. Simulations are carried out for two drops of volume 0.035 mm^3 and 0.27 mm^3.

Table 4.3: Simulations for different wettability characteristics of the bottom surface

Case No.	Air velocity (m/s)	Water volume (mm^3) (initial radius, mm)	Wettability of bottom surface	Residence time (ms)
1	3	3.35×10^{-2} (0.2)	Surface A (90° to 10°)	12.1
2	3	3.35×10^{-2} (0.2)	Surface B (90° to 170°)	10.6
3	3	0.27 (0.4)	Surface A (90° to 10°)	16.5
4	3	0.27 (0.4)	Surface B (90° to 170°)	13.8
5	5	3.35×10^{-2} (0.2)	Surface A (90° to 10°)	8.4
6	5	3.35×10^{-2} (0.2)	Surface B (90° to 170°)	7.65
7	5	0.27 (0.4)	Surface A (90° to 10°)	14.5
8	5	0.27 (0.4)	Surface B (90° to 170°)	13.5
9	10	3.35×10^{-2} (0.2)	Surface A (90° to 10°)	5.7
10	10	3.35×10^{-2} (0.2)	Surface B (90^0 to 170°)	5.5
11	10	0.27 (0.4)	Surface A (90° to 10°)	9.5
12	10	0.27 (0.4)	Surface B (90° to 170°)	8

Drop of 0.035 mm^3 corresponds to a drop radius of 0.2 mm and the other one is of 0.4 mm. In both the cases the drops are freely suspended at the center of the channel at a distance of 5 mm from the inlet**.** Air velocity (U_g) is varied from 3, 5 to 10 m/s. Details of the simulations are provided in Table 4.3.

The range of gas phase Reynolds number varies from 204 to 680. These corresponds to active fuel cell operating condition with current densities in the range of 0-1.5 A/cm^2 and a maximum stoichiometric ratio of 10.

a) **Effect of wettability gradient on Hydrodynamics of drops**: Figure 4.10 shows gradual deformation of the suspended drop with time for U_g 10 m/s. Initially spherical drop is deformed with time. After 1.5 ms it hits the bend. The trend is matching with that reported by Quan et al. (2005). After it hits the bend tiny drops are formed at the downstream of the bend due to presence of secondary flow at the bend. Next, the shape of the drop is compared at surface A and B in Figure 4.11. The additional surface force can be written as

$$F_s \propto r\gamma\left(\cos\theta_f - \cos\theta_r\right) \tag{4.12}$$

where, r is the radius or characteristic length of the drop, γ is the interfacial tension between air and water. θ_f and θ_r are forward and rear contact angles respectively. The magnitude of $\cos\theta_f - \cos\theta_r$ will decrease as the drop moves towards the outlet. In case of the surface A the direction of the force is positive (in the direction of flow) while for that of surface B it is negative (opposite to the direction of flow).

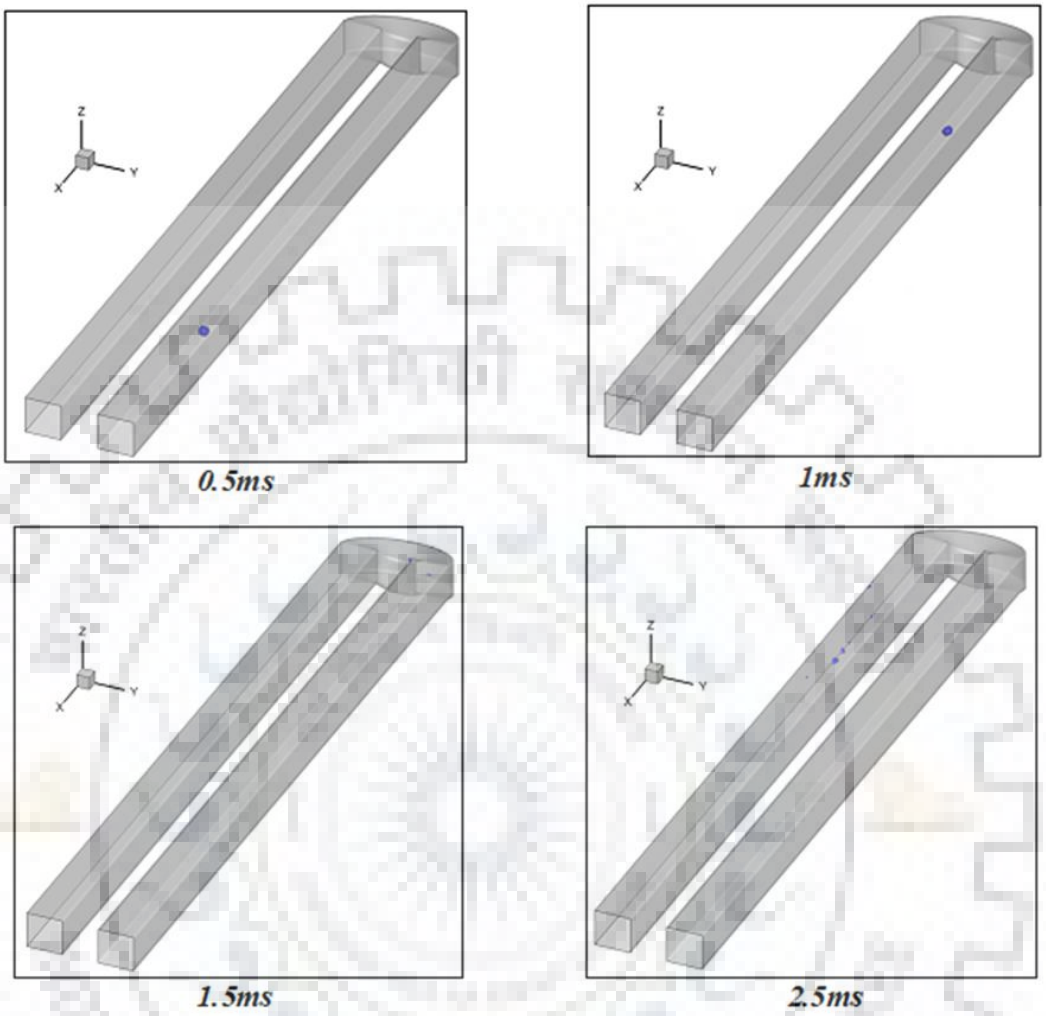

Figure 4.10: Deformation of single drop of 0.035 mm^3 with time in serpentine channel with surface A, at U_g 10 m/s

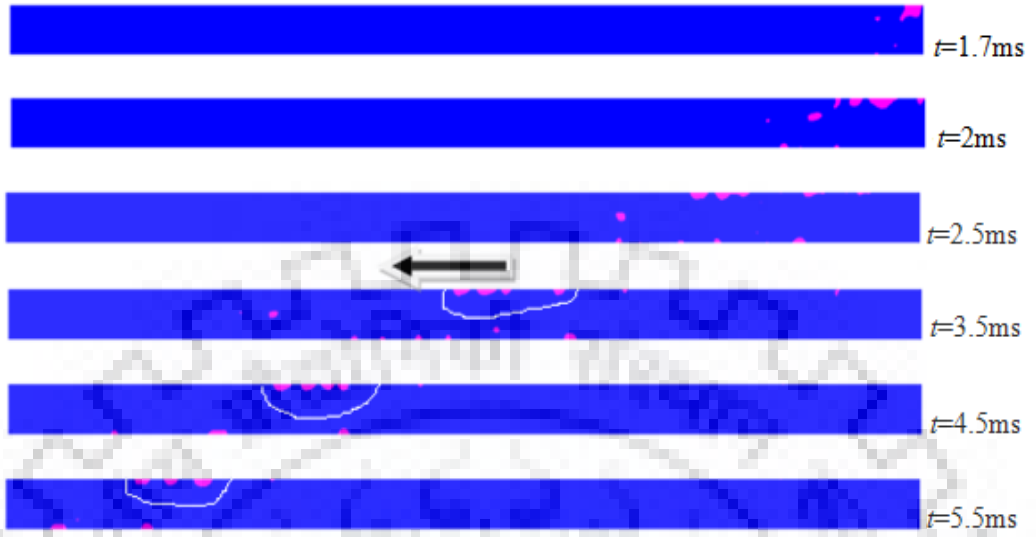

a) Surface A

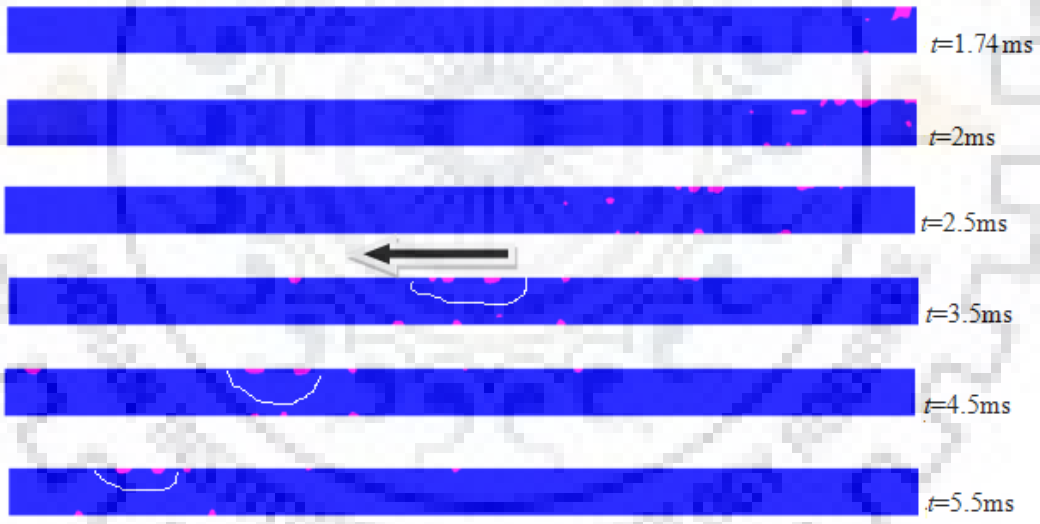

b) Surface B

Figure 4.11: Time variation of the phase contour for the drop of 0.035 mm^3 at modified GDL surfaces at U_g 10 m/s

It can be seen from the Figure 4.11 the size of the drops is smaller on surface B and tends to be more spherical as expected. In the simulation results, the pink color refers to the presence of water, while the dark blue color refers to the presence of air.

A critical analysis of the figures shows some interesting facts. In both the cases, it has been observed that tiny fractions of water formed at the bend are move swiftly by the air and coalesces with larger fraction. This is highlighted in both the modified GDLs. As the larger fractions are moving towards the outlet, they become more spherical for surface B because of continuous increase of contact angle. This in turn helps in removal of the drop. However, the drops are not fragmented due to the presence of additional surface force.

Hence it can be said that at U_g 10 m/s, drag is much higher, which governs the coalesce and subsequent removal of tiny water fractions of the water drop.

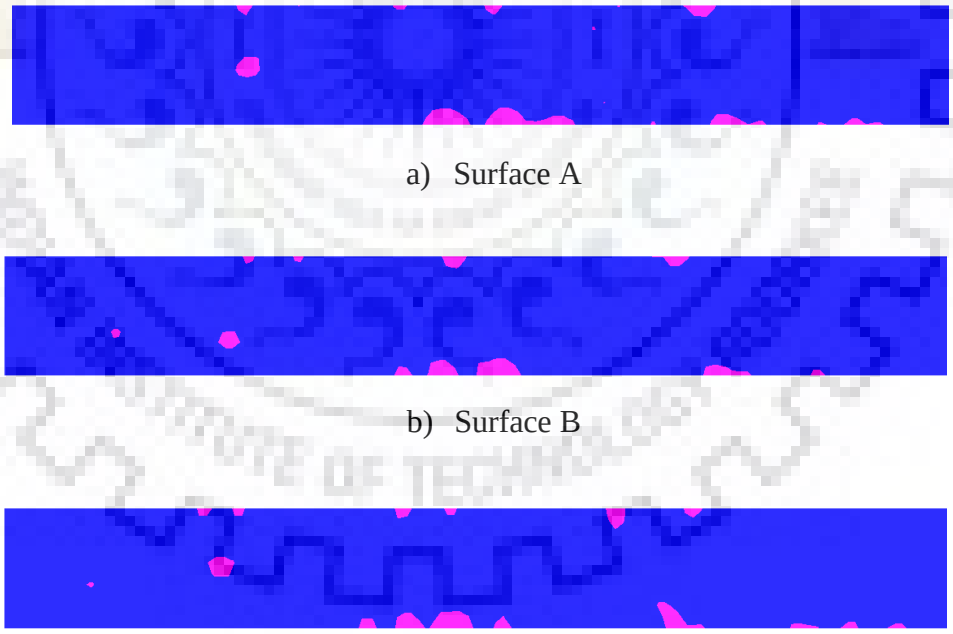

a) Surface A

b) Surface B

c) Constant contact angle of 90°

Figure 4.12: Phase contours at different GDL at time 2.5 ms for U_g 10 m/s and drop volume 0.035 mm^3

At this point a case has been simulated with a partially wetted GDL of constant contact angle of 90˚ in order to check if the gradient of wettability has any influence on water content. The contours for this GDL and other two cases are shown in Figure 4.12. The water amount in the constant contact angle GDL, is more than that of surface A and B.

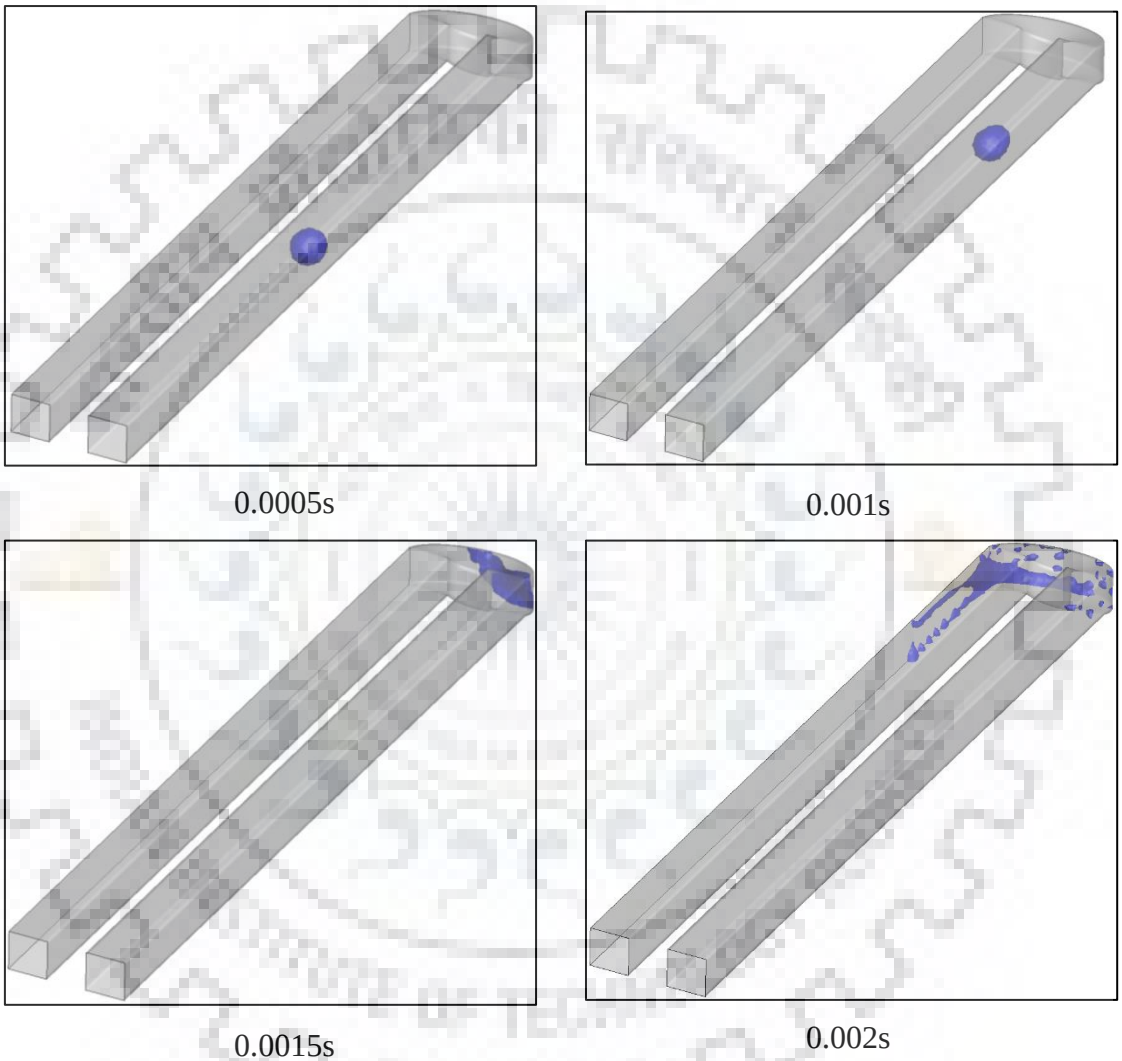

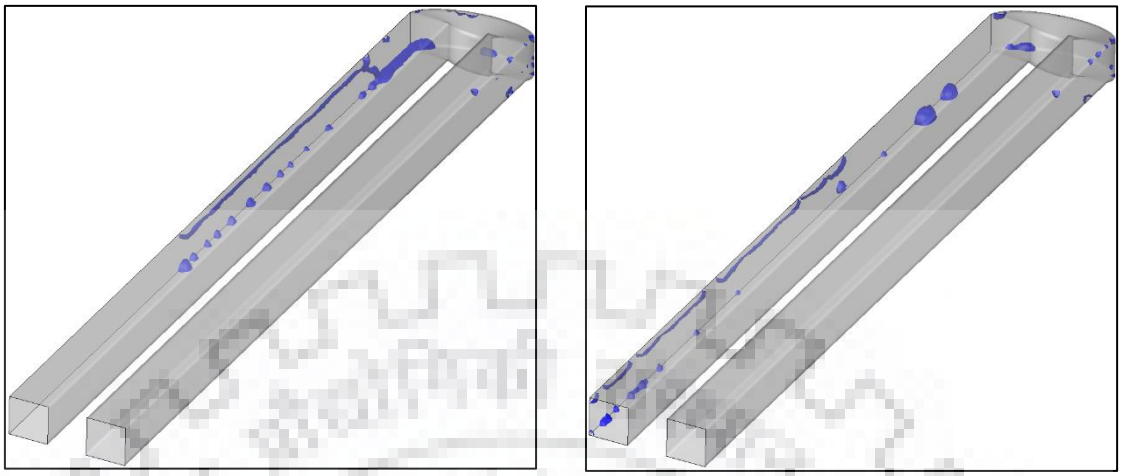

0.003s 0.005s

Figure 4.13: Deformation of single drop of 0.27 mm^3 with time in serpentine channel with surface A at U_g 10 m/s

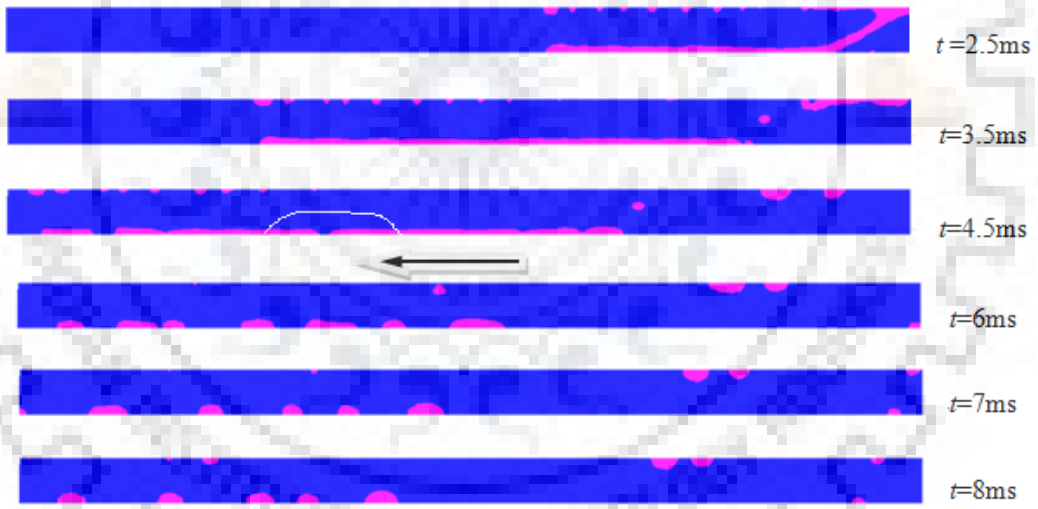

a) Surface A

b) Surface B

Figure 4.14: Time variation of the phase contour for the drop of 0.27 mm^3 at modified GDL surfaces at U_g 10 m/s

This is in agreement with the observation of Jiao and Zhou (2006). They also reported that hydrophobic GDL of 135° retains higher amount of water. The reason can be attributed to the fact that in absence of wettability gradient in the GDL. As mentioned earlier, in surface A, surface force acting in direction of flow. Hence aiding the movement of the drop. In surface B, surface force acting opposite to the direction of the flow. However, water fractions are dragged by air, they become more spherical and easily removed by air. On the other hand, in absence of this surface force, water drop coalesces and increases water content.

Next interest is felt to increase the drop size. Hence simulations are carried out for a freely suspended drop of radius 0.4 mm. Figure 4.13denoted the sequence of drop deformation with time for same air velocity single drop of 0.27 mm^3. It can be noted the larger drop started deforming after 0.6 ms. From the figure it is evident that the drop deforms slightly with time before it forms a film at the bend. After the bend, it forms a thin layer of water at the inner side of the bottom surface and forms tiny drops at the outer side.

Next the phase contours at surfaces A and B are compared in Figure 4.14. A closer observation of the figure reveals the following: in case of the surface B the film at the inner side of the bottom surface is broken at two positions as compared to a very smooth film at the surface A at 4.5 ms. In case of surface A, where the bottom surface become gradually hydrophilic, the water film spreads leading to formation of smooth continuous film which is difficult to remove. However, when the film encounters a gradual increase in contact angle it tries to minimize the contact area and as a result the film breaks. This in turn helps in removal of the water fraction. It can be seen from the figure that the surface A retain a longer thin film of water at the inner side. On the other hand, the surface B initiates a break in the same. Hence, it can be said that a gradual hydrophobic bottom surface is preferable after the bend if the drop volume is sufficiently large.

As mentioned earlier the water spreading on GDL surface reduces its performance. Hence one of the major objectives of water management that minimum area is covered by water. In the present study the modified bottom surface is considered as GDL. Next, efforts are made to understand the wettability effect on instantaneous in-situ volume fraction of water (α). For this α is estimated for bottom surface after bend. It is estimated from the contours of bottom surface using a small program of MATLAB. The contours obtained from the simulation are subjected to gray scale and subsequently to black and white conversion. The black and white images thus obtained used to estimate the instantaneous volume fraction as

$$\alpha = \frac{A_w}{A} \tag{4.13}$$

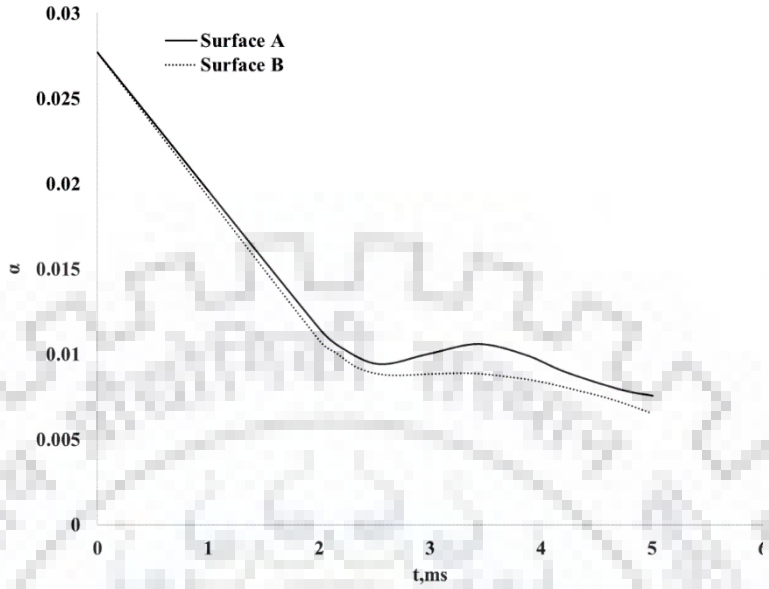

a) Drop volume 0.035 mm^3

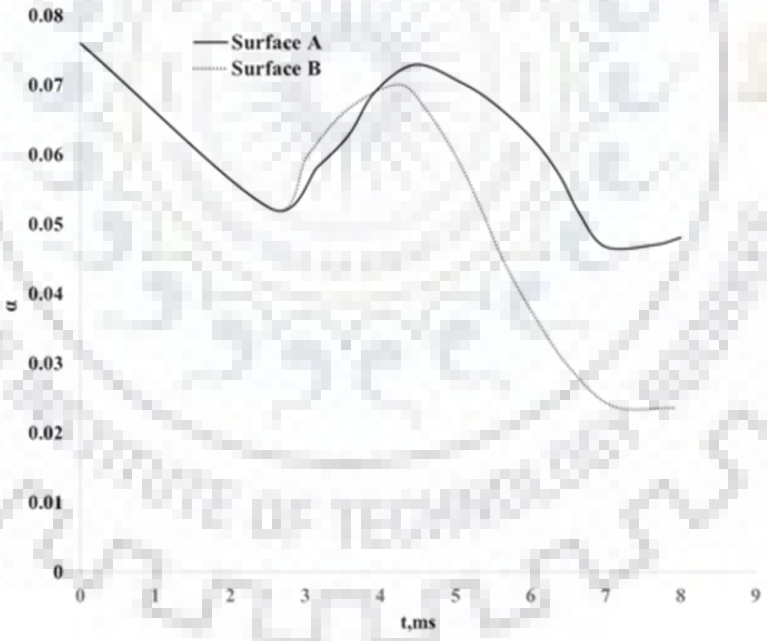

b) Drop volume 0.27 mm^3

Figure 4.15: In-situ water content as a function of time for different GDL surfaces at 10 m/s

where, A_w is the area occupied by water and A is area of the modified bottom surface in the contour.

Figure 4.15 a and b depict the variation of α with time at U_g 10 m/s for drop radius of 0.2 mm and 0.4 mm respectively. As seen from the figures, that the instantaneous profile of α is different for the two drops. It can be seen from Figure 4.15a that α first decreases with time and then increases and followed by a steady decrease for surface A. For Surface B it is almost a continuous decrease. This can be attributed to the fact that at surface B, as the drops move their contact area are lesser leading to less water content. In surface A, due to drop coalescence and spreading water content increase with time.

However, after a critical value of drop radius is reached, the surface force become larger and aiding for the removal of the drop. Similar trend is also observed for the larger drop. In this case the drop was not fragmented at the bend rather a film was form as evident from Figure 4.14a and b. Hence, as it starts moving downstream after the bend, α increases for both types of GDL surfaces reaches a maximum and start decreasing. Higher water amount is observed for surface A then surface B.

Figure 4.16 a and b show time variations of radial pressure along the axis of the modified GDL surfaces. The peaks in the pressure profile represent presence of water in that particular axial location. It can be noted from the figure that surface A always shows at higher pressure than surface B for both the cases. The reason can be attributed to lesser contact surface area for a hydrophobic surface and therefore the pressure drop. In case of the larger drop, surface B tends to break to form smaller ones hence reduces the pressure. In case of surface A, as it is covered with thin film so the area available for air is lesser.

This in turn leading to a higher velocity which leads to a higher pressure drop. However, the surface area covered with water in hydrophobic case is smaller in comparison to the former hence a lower pressure drop is encountered in this case.

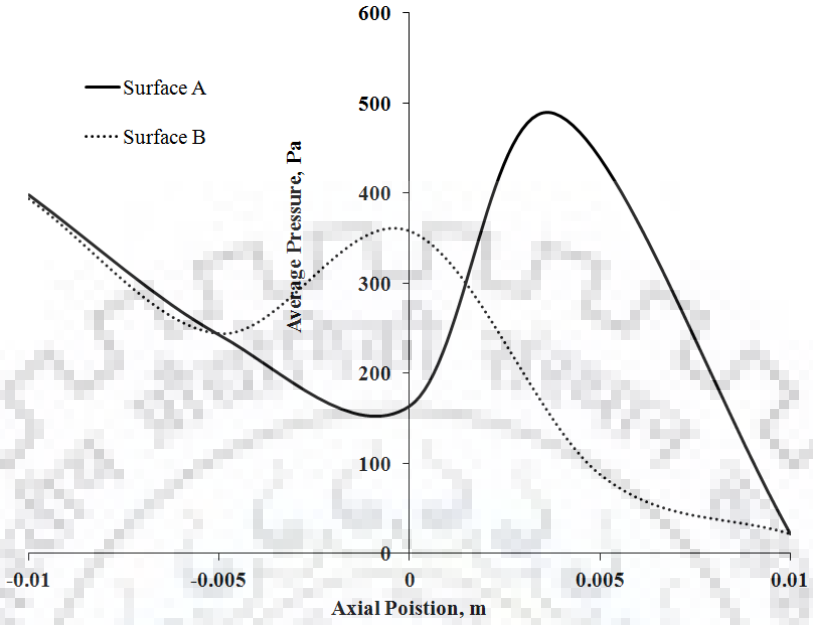

a) Drop volume 0.035 mm^3

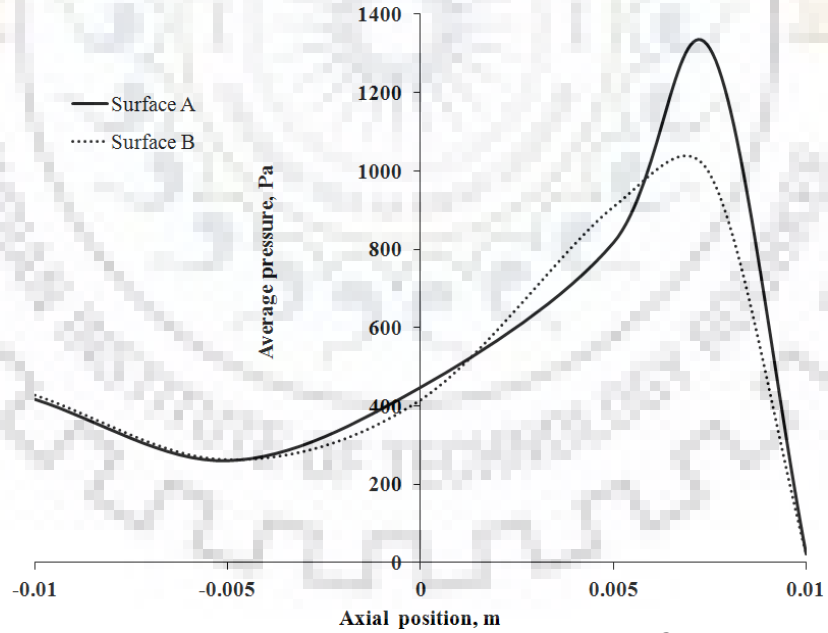

b) Drop volume 0.27 mm^3

Figure 4.16: Average pressure as a function of axial position for different GDL surfaces at 4.5 ms and U_g 10 m/s

b) Effect of air velocity on drop dynamics: Next interest is felt to investigate the drop dynamics in reduced air velocities.

For this purpose, air velocities are changed from 10 to 5 and 3 m/s. In order to compare the water coverage of the bottom surfaces by water at different air velocities, time averaged α values, denoted by α_t is plotted as a function of U_g for both the surfaces in Figure 4.17a. It can be seen from the Figure 4.17a that the water coverage is minimum for U_g 3 m/s for both the surfaces. It increases with increase in U_g and slightly decreases with further increase at U_g 10 m/s.

However, a close observation of the figure reveals that the water coverage at surface B is almost 0.2 % while that of surface A is 1% at the same U_g 3 m/s. Also, the variation of α_t for surface A is very less with increase in U_g. On the other hand, it varies 5 times for surface B. The reason explained as decrease in inertial force on drop. As the inertial force over power by surface force, at U_g 3 m/s, fragmentation is easier in case of a hydrophobic surface. At the same time, in a hydrophilic surface, drop coalescence takes place more easily and formed a larger fraction which is difficult to remove.

This is also evident from Figure 4.18 where the magnified view of the water fractions are shown for drop volume of 0.035 mm^3 on both the surfaces at U_g 3 m/s. For the larger drop volume, trend of variation of α_t with U_g is similar to that of the previous case. However, α_t first remain same then increases with increase in U_g for surface B. The reason can be attributed to increase of inertial force which enhances the tendency of drop coalescence. Hence, it can be said that if a GDL in serpentine channel is coated with a hydrophobic gradient then it has less water coverage on the surface at lower air velocities.

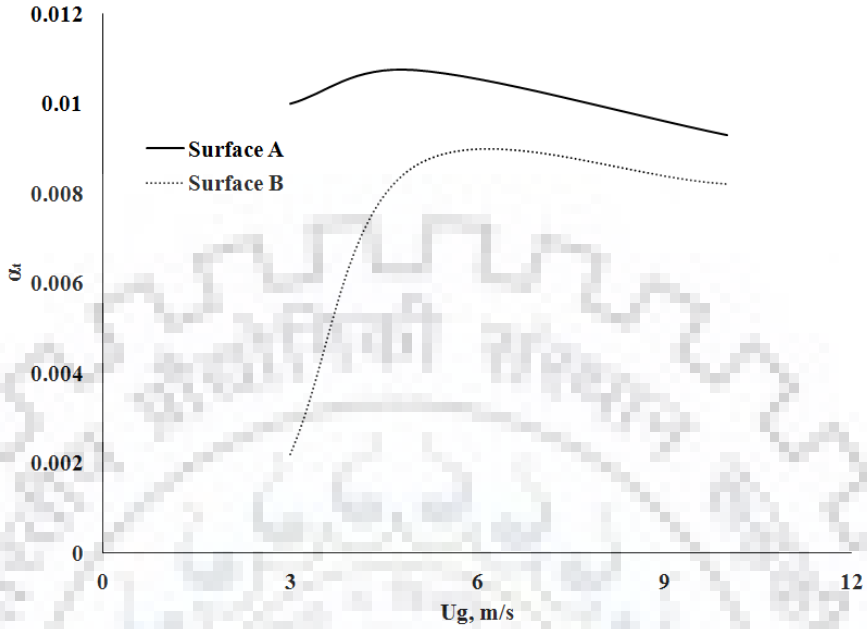

Drop volume 0.035 mm^3

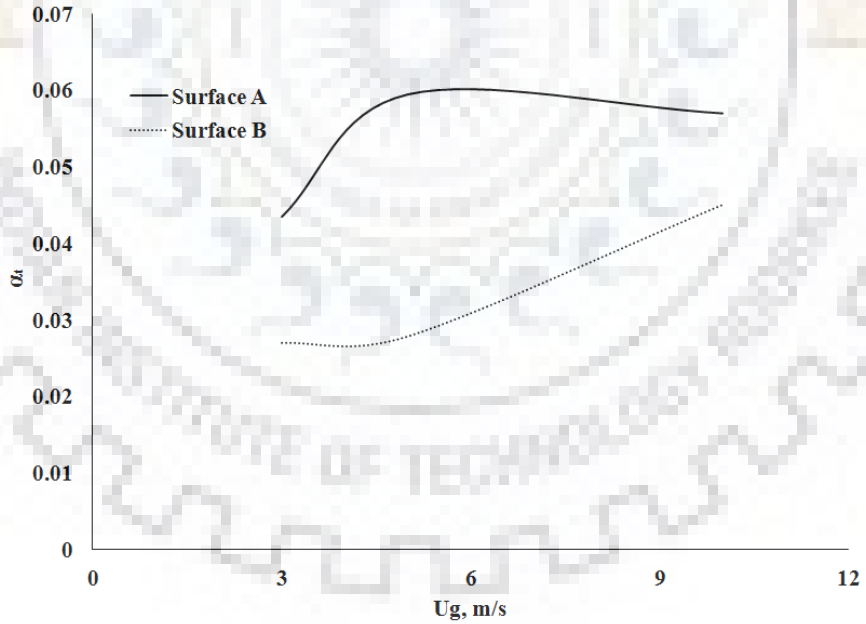

a) Drop volume 0.27 mm^3

Figure 4.17: Time averaged water content as a function of inlet gas velocity with GDL surfaces as parameter

a) Surface A

b) Surface B

Figure 4.18: Transition of drop from modified surfaces to side wall at U_g 3 m/s for drop volume of 0.035 mm^3

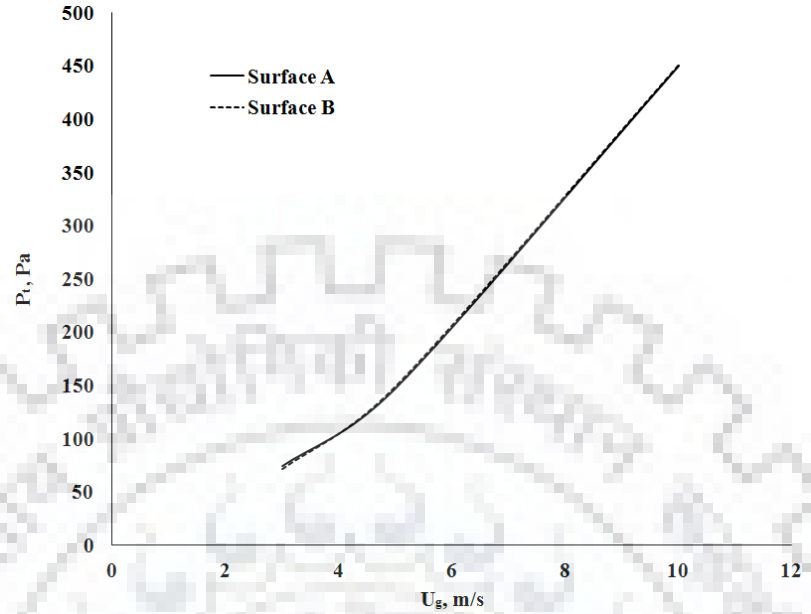

a) Drop volume 0.035 mm^3

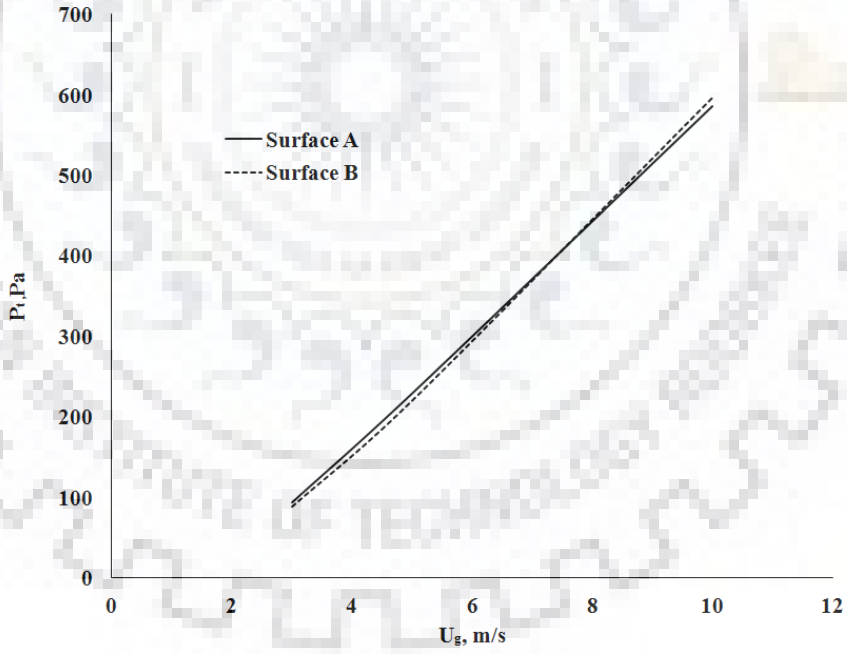

b) Drop volume 0.27 mm^3

Figure 4.19: Time averaged pressure as a function of inlet gas velocity with GDL surfaces as parameter

Next the time averaged pressure drop between inlet and outlet of the serpentine channel is plotted against air velocity with GDL surfaces as parameter in Figure 4.19. It can be seen that the time averaged pressure drop is a linear function of air velocity and it remains almost same for both the surfaces. However, it increases with increase in drop volume. Hence it can be said that from the point of view of pressure drop it is effective if the PEMFC is operated at lower air velocity

4.4. Drop on bottom surface

Next, interest is felt to study the dynamics of a drop if it is on the bottom surface at upstream instead of suspended. Since the drop is at the upstream of bend, hence a hybrid bottom surface is used in present case as discussed earlier. The bottom wall of the channel has been divided into surfaces and two different use defined functions have been compiled and incorporated. Table 4.4 gives the details of simulation of drop on bottom surface.

A constant drop volume of 0.27 mm^3 is taken for this purpose. It is adhered to bottom surface at 2 mm from the inlet

Table 4.4: Simulations for different wettability characteristics of the bottom surface for combined gradient

Air Velocity(m/s), U_g	**Wettability Gradient**
3	4°/ mm
	5°/ mm
5	4°/ mm
	5°/ mm
10	4°/ mm
	5°/ mm

Magnitudes of gradient used in this case are 4°/ mm and 5°/ mm. Figure 4.20 shows the deformation of an adhered drop in presence of 5°/ mm at U_g of 5 m/s.

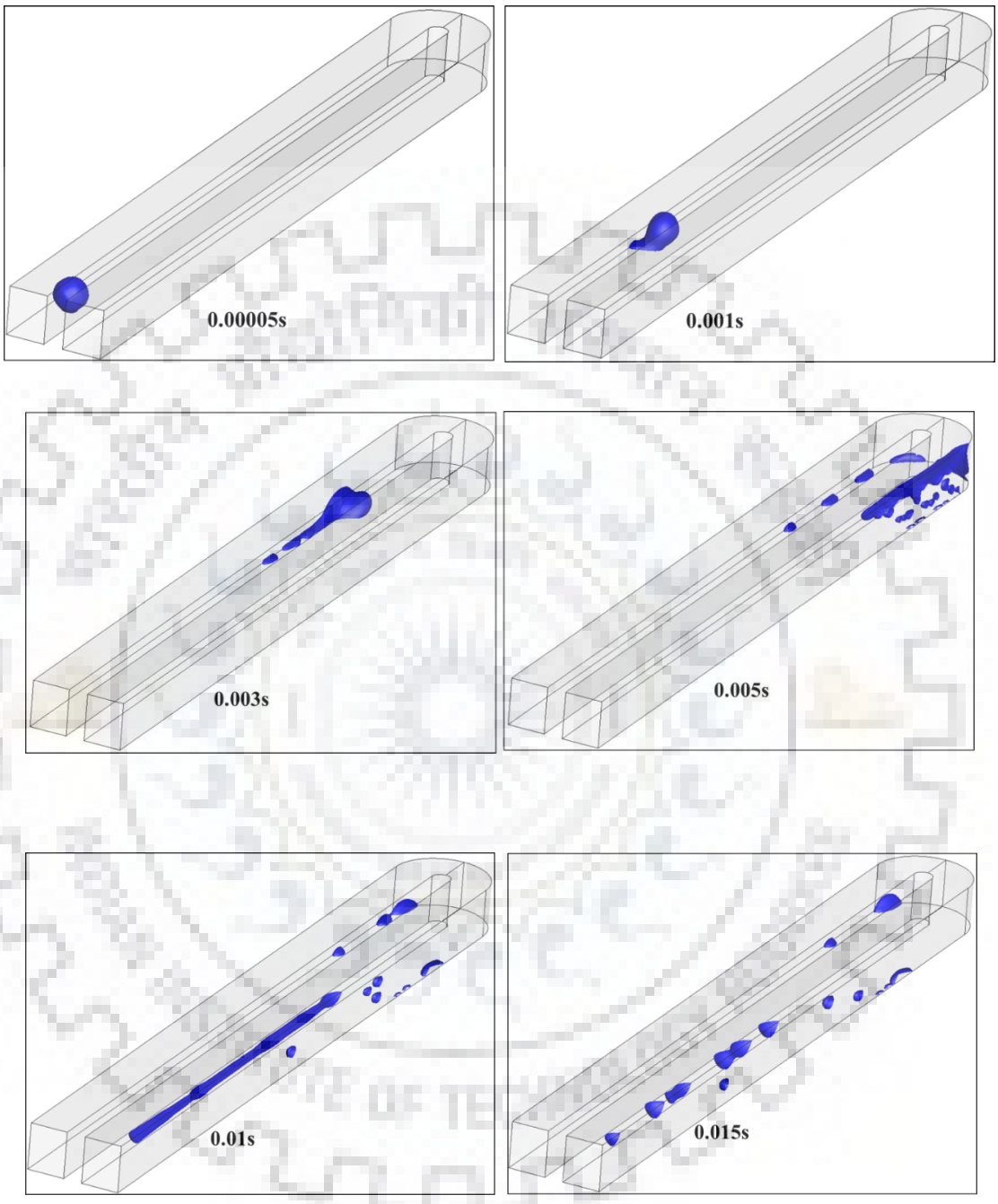

Figure 4.20: Deformation of attached drop at 5^0/ mm at U_g 5 m/s

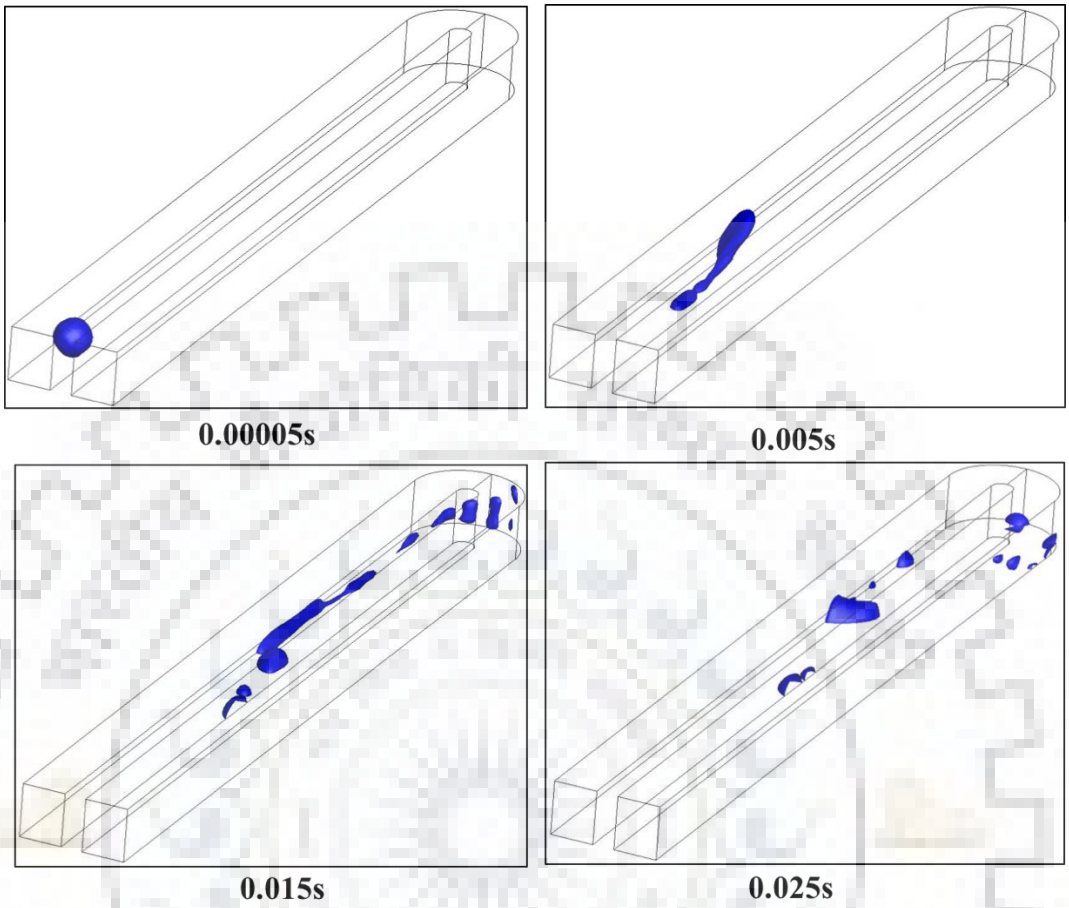

Figure 4.21: Deformation of drop (0.27 mm^3) on constant contact angle of 72°and U_g 5 m/s velocity

Figure 4.20 depicts a time series of drop movement. In the figure, blue color marks presence of water. It can be seen from the figure that the drop starts spreading at upstream bottom surface where contact angle reduces in the direction of flow. On comparing with suspended drop it can be observed that, the deformation dynamics is very different in this case. The drop started deforming at the upstream and a trail of water is formed. Fragmentation of this trail initiates before the drop hits at bend. After the drop hit the bend, larger portion of it remains at outer top surface of the bend. Some smaller drops are seen at the downstream bottom surface. But, majority of the fraction travel as film at the corner of top surface and side wall. With time this film is fragmented and formed drops which are removed subsequently.

a) Effect of wettability gradient on drop dynamics

Next investigations are performed to understand the effect of wettability gradient on drop dynamics. In order to do so, simulations are performed in same geometry which has a constant contact angle of 72° with same volume of water. Phase contours for this situation is shown in Figure 4.21 for U_g 5 m/s.

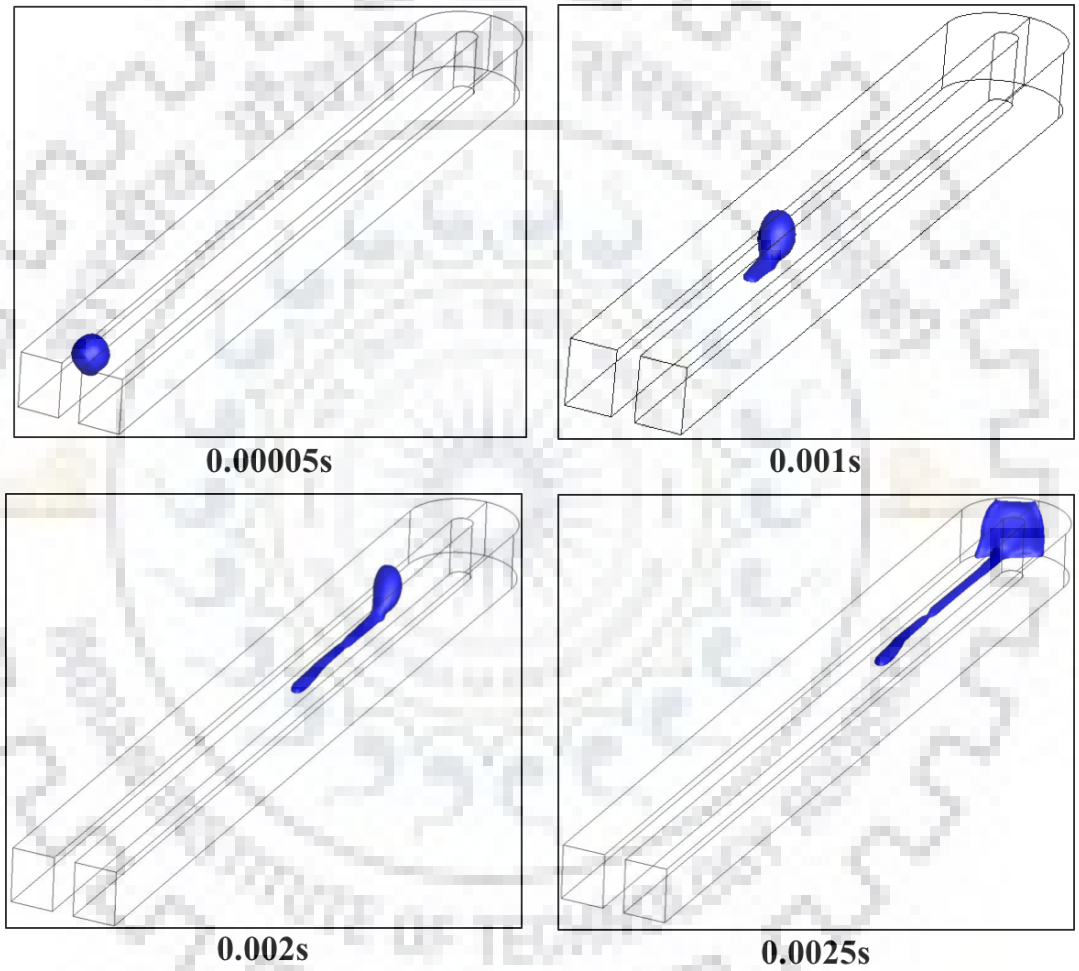

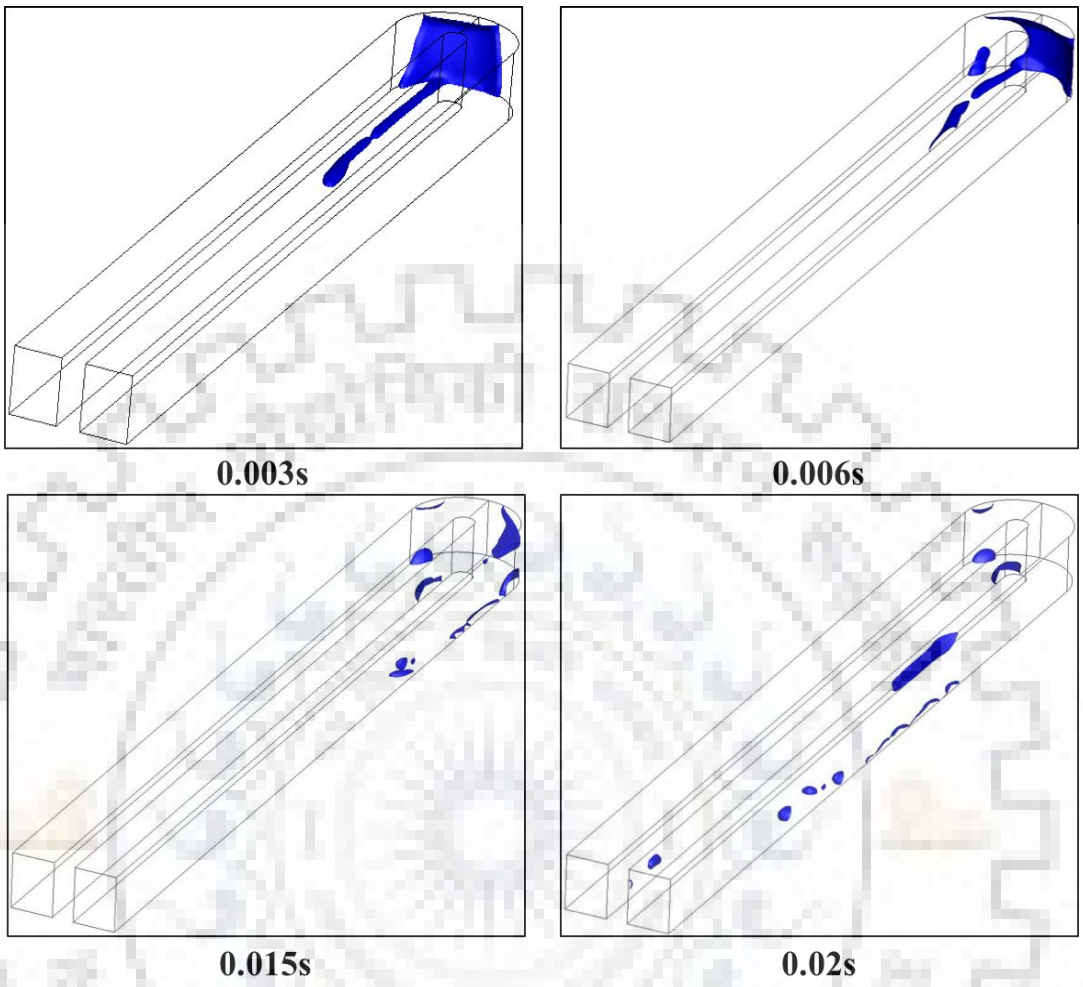

Figure 4.22: Deformation of drop (0.27 mm^3) at constant contact angle (72°) and U_g 10 m/s velocity

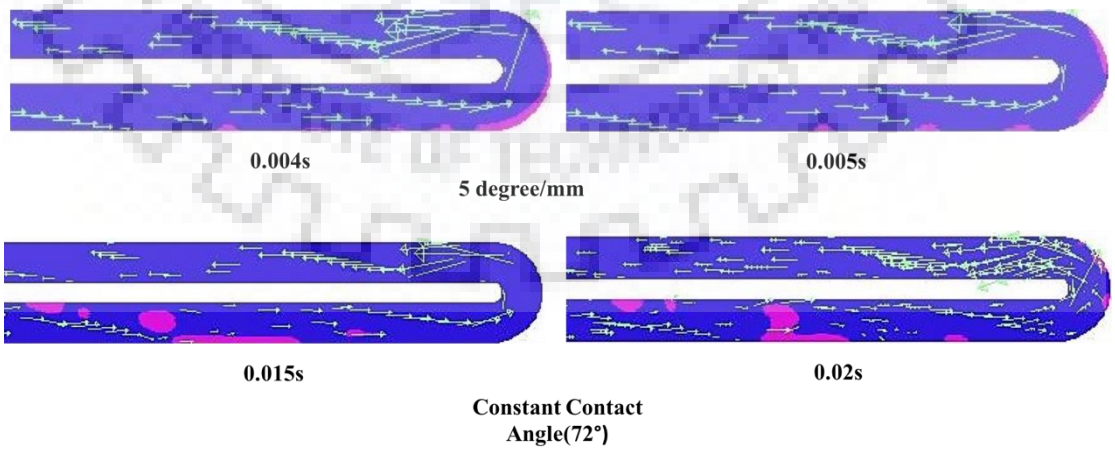

Figure 4.23: Velocity vectors with phase contours at U_g 5 m/s

A close look of Figure 4.20 and Figure 4.21 reveals that the dynamics of drop deformation and removal is completely different for these two cases. In later case, the drop is moving slowly in comparison of 5°/ mm surface. Also, it deformed early and continuously sticking to the bottom surface. On the other hand, due to presence of an additional surface force, drop moves quickly in former. It also remains intact while colliding with bend and major fraction of it are at the top surface, leaving the GDL free. Similar observations can also be made for U_g 10 m/s in Figure 4.22.

Next, Figure 4.23 shows velocity vectors with phase contours at U_g 5 m/s for both 5°/ mm gradient and constant contact angle (72°). It can be seen that velocity vectors are similar in nature for both cases. However, the position of water fraction is different.

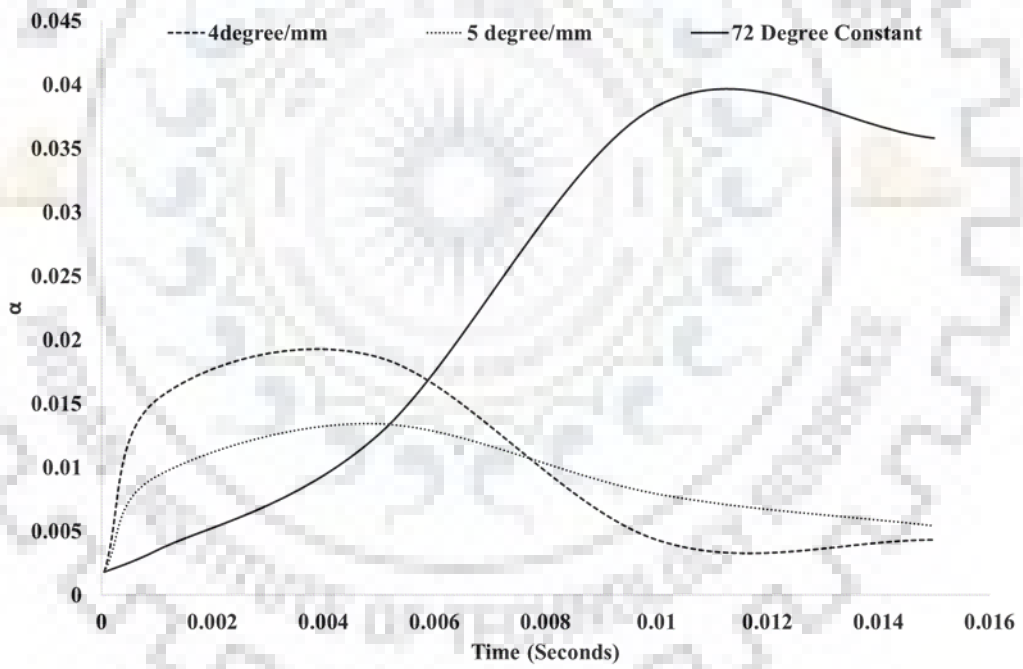

Figure 4.24: In-situ water content as a function of time for different GDL surfaces at U_g 5 m/s

This difference in dynamics expected to cause a change of the variation of α . Figure 4.24 shows that instantaneous values of α for 4°/ mm, 5°/ mm and constant 72° for U_g

5 m/s. It can be noticed from the figure that due to adherence of water at constant hydrophilic surface a large fraction of channel is covered with water. For same instant of time 0.015 s the retention of water on constant 72° is almost 7 times than that in 5°/ mm gradient. Hence, it can be concluded that such kind of hybrid gradient are useful in removing the adhered drop from surfaces.

b) Comparison with suspended drop

Next, an interest is felt on visualizing the difference of dynamics in case of suspended drop and adhered drop. As the suspended drop are simulated for a gradient of 4°/ mm. Figure 4.25 depicts deformation of a drop-in case of drop on surface with a gradient of 4°/ mm at U_g 10 m/s. A comparison with Figure 4.13 shows that two significant differences. As the drop remain suspended till it hits the bend, hence the overall time of removal in case of suspended drop is much smaller than adhered drop. On the other hand, in case of suspended drop a large amount of water after hitting bend remains on GDL surface while in case of adhered drop it remains on top surfaces.

In order to compare quantitatively, Figure 4.26 compares variation of α for 4°/ mm gradient and U_g 10 m/s in both the situations including both upstream and downstream bottom surfaces together. A close look of the figure reveals that for the same drop volume of 0.27 mm^3, suspended drop takes half of the time taken by adhered drop, however the area coverage with water is order of magnitude higher in presence of a wettability gradient.

Therefore, it can be said that suspended drop remains intact at upstream and hit the corner of the bend due to centrifugal force. After the collision, fragmented drop falls on the bottom surface at downstream of bend. While, in case of adhered drop, fragmentation of drop started at upstream, after hitting the bend, the tiny fractions are remaining on the upper surface. Hence, it can be concluded that, when a drop is suspended it may be removed quickly in comparison to adhered drop. However, it blocks the GDL to a higher extent. Modified surfaces with wettability gradient are instrumental in moving adhered drop at upstream before hitting the bend.

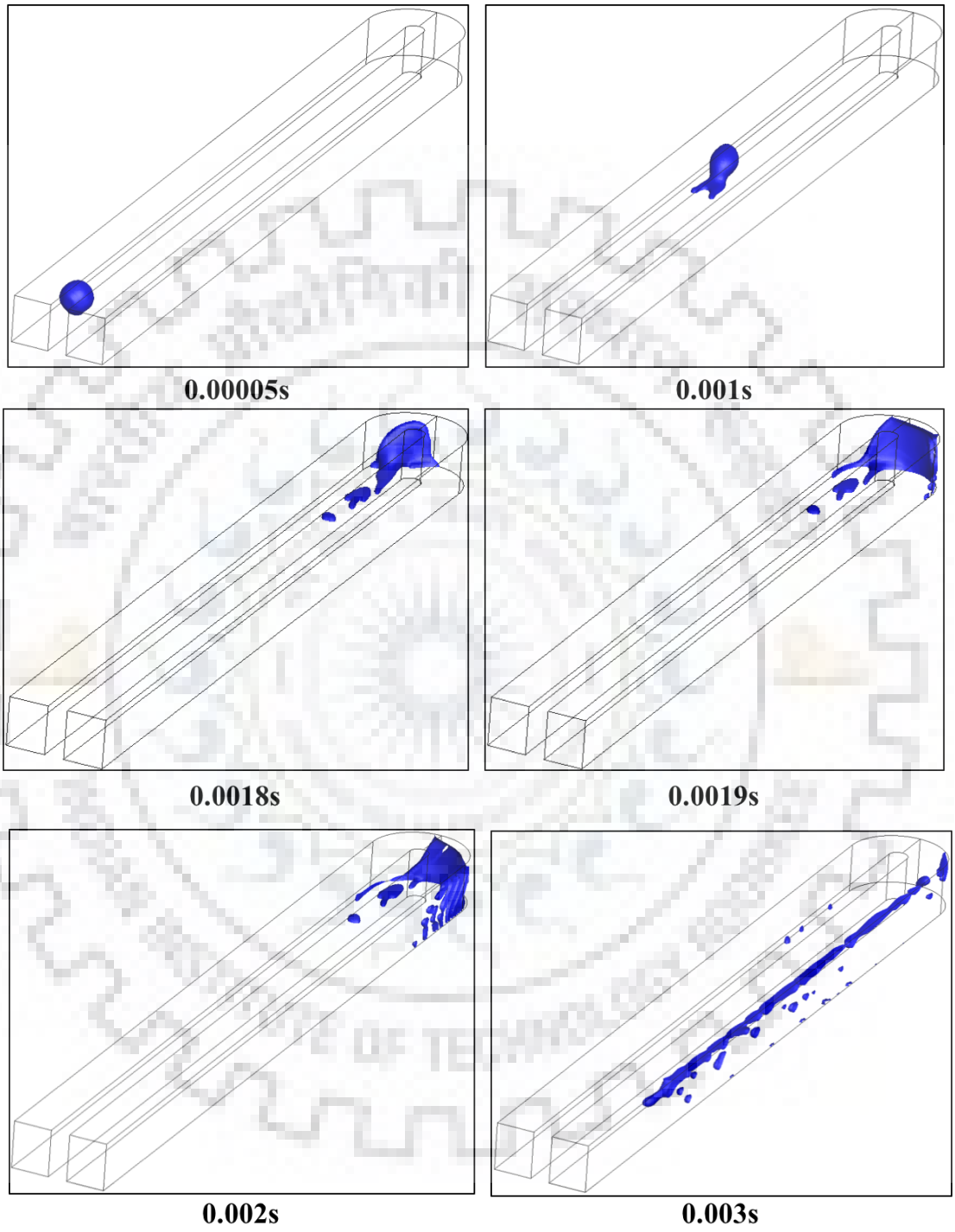
0.00005s
0.001s
0.0018s
0.0019s
0.002s
0.003s

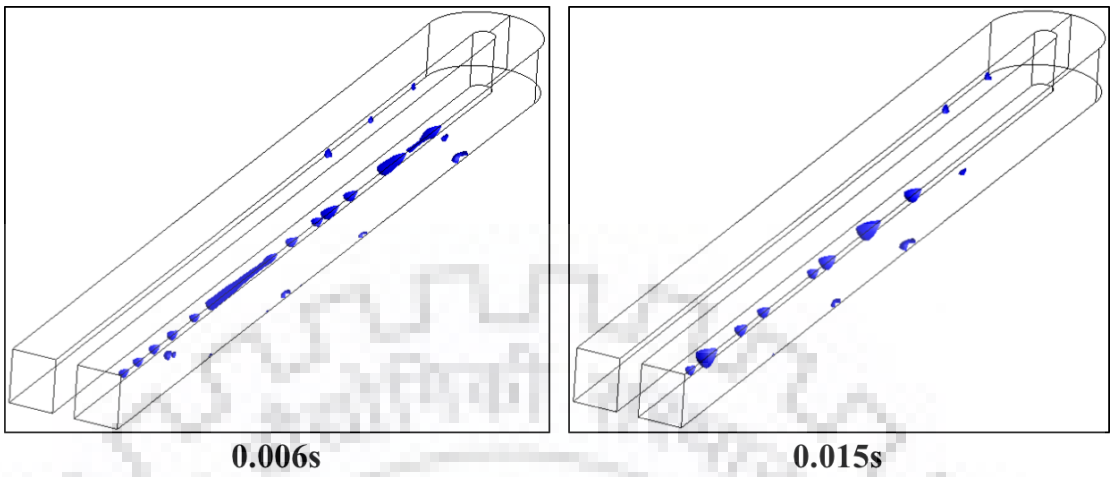

Figure 4.25: Deformation of drop (0.27 mm^3) at 4°/ mm gradient and U_g 10m/sec velocity

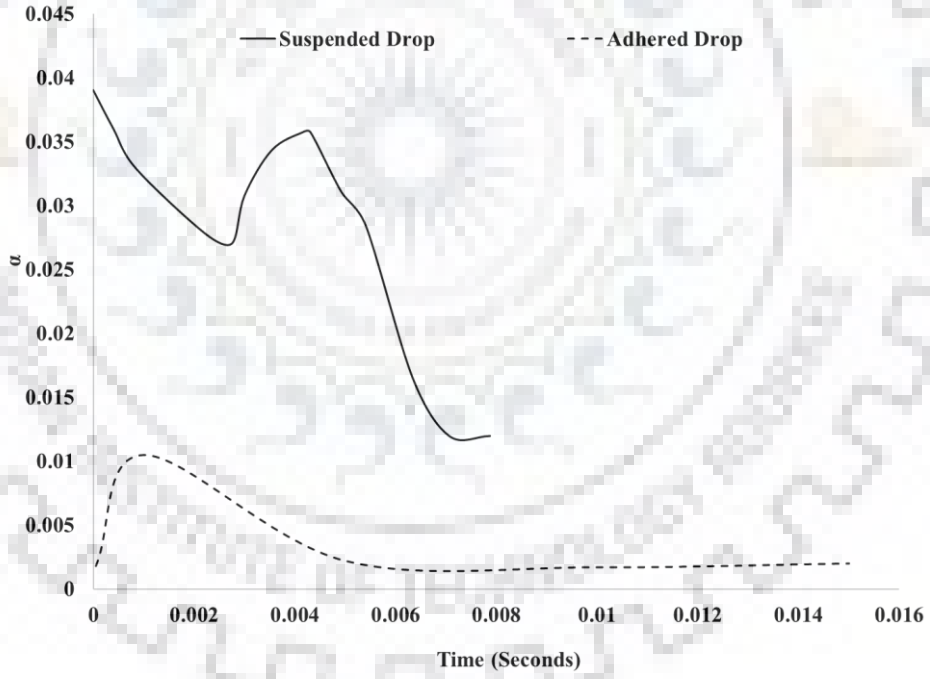

Figure 4.26: In-situ water content suspended drop (0.27 mm^3) and adhered drop (0.27 mm^3) at 4°/ mm gradient and U_g 10m/s velocity

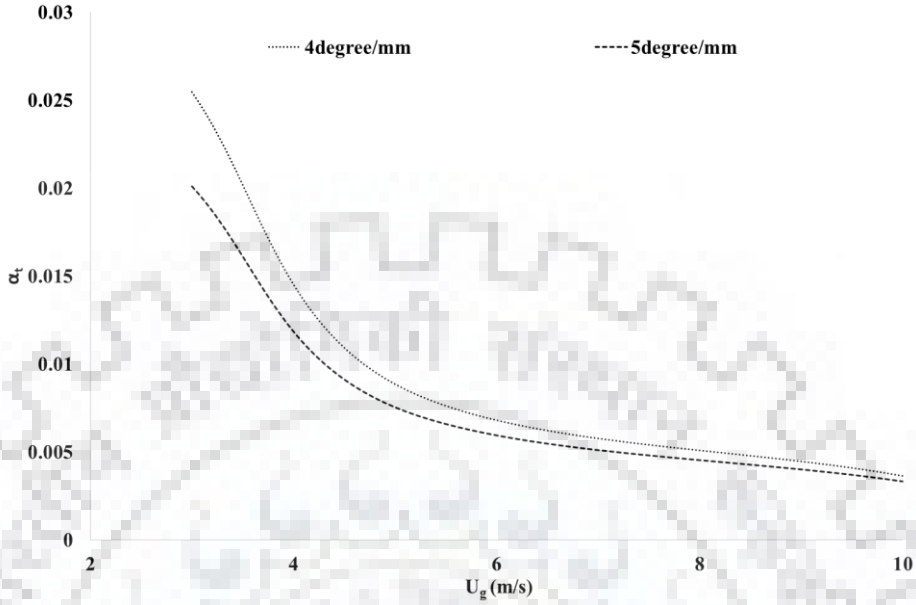

Figure 4.27: Time averaged water content as a function of inlet gas velocity with GDL surfaces as parameter for combined gradient

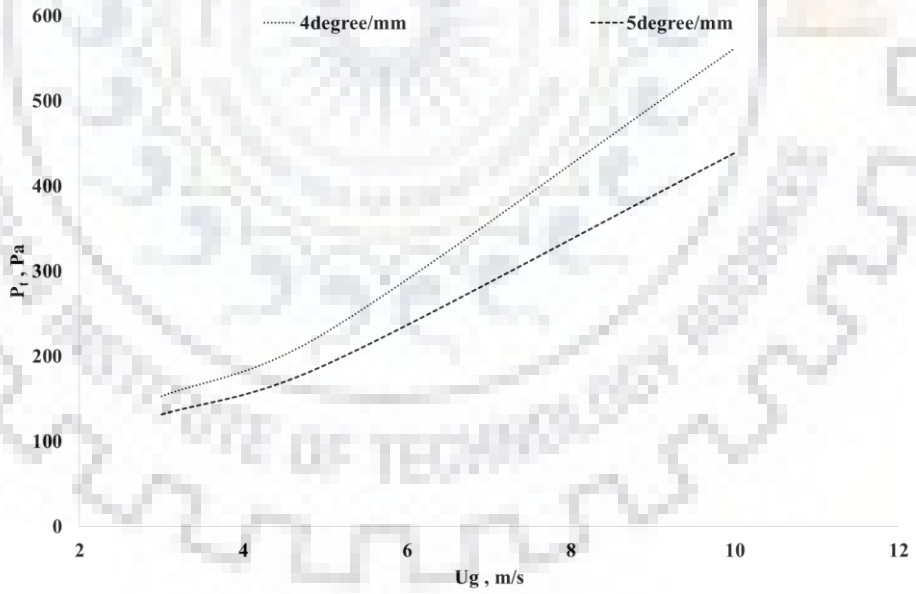

Figure 4.28: Time averaged pressure as a function of inlet gas velocity with GDL surfaces as parameter

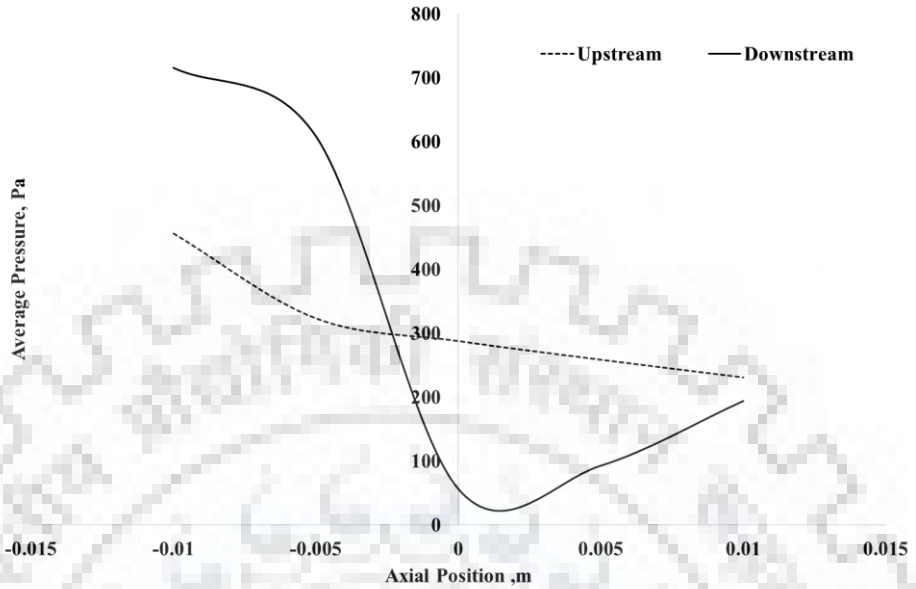

Figure 4.29: Average pressure as a function of axial position at U_g 5m/s, 5°/ mm at 0.01 s

c) Effect of air velocity

Further simulations are performed to understand the influence of air velocity on drop dynamics. Figure 4.27 shows the variation of α_t with U_g for adhered drop. It can be seen from the figure that α_t decreases with increase of U_g. This decrease is gradual, and the trend is similar for both the gradients. It can be seen that, with increase of U_g the value of α_t is similar for both the gradient. On the other hand, for smaller magnitudes of U_g, α_t values are slightly higher for 4˚/mm gradient.

Figure 4.28 depicts P_t with U_g. It shows an increase of pressure with U_g for both the cases. However, P_t is higher for 4˚/mm than 5˚/mm. The reason can be attributed to initial higher retention of water for 4˚/mm as can be seen from Figure 4.25. In case of 4˚/ mm, presence of higher amount of water for longer time may results in higher time averaged pressure. Figure 4.29 shows an instantaneous pressure with axial position at

up and downstream of U bend. It can be seen from the figure that the pressure at upstream is lower than downstream. This indicates the position of water drop at downstream as also can be seen from phase contours in Figure 4.20.

4.5. Slug flow in U bend

In this section slug flow is simulated with a separate entry of water. The flow combinations used for present simulation corresponds to slug flow situation in T2 for chapter 3.

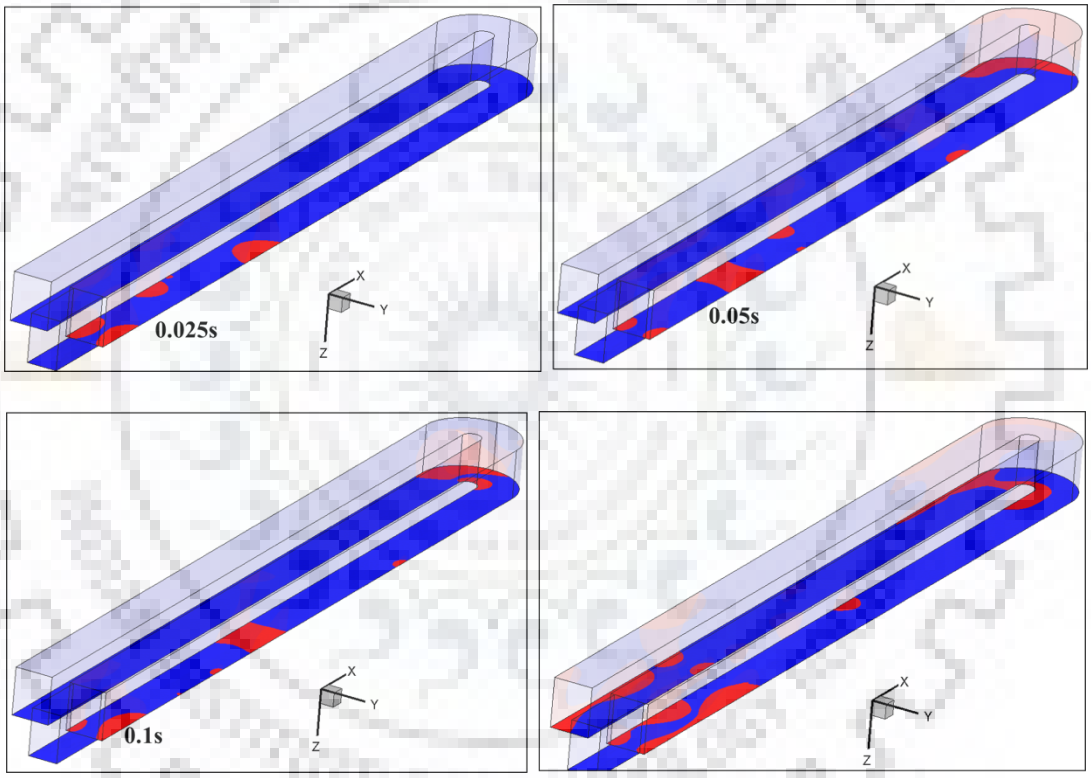

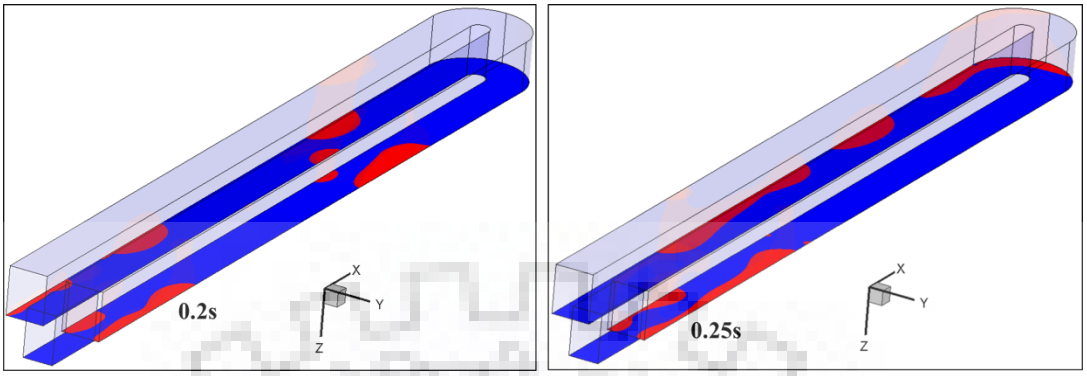

Figure 4.30: Bottom wall contours of slug flow at U_g = 3.33 m/s and U_l = 0.083 m/s at constant 72°

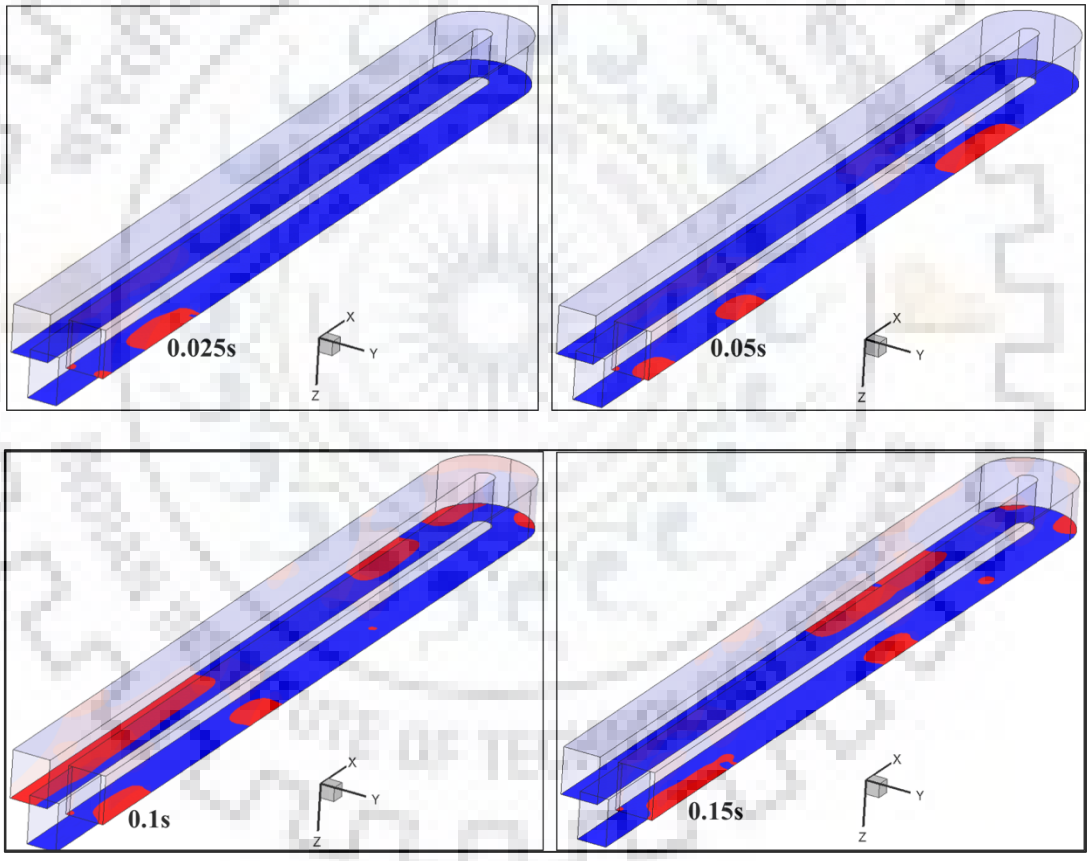

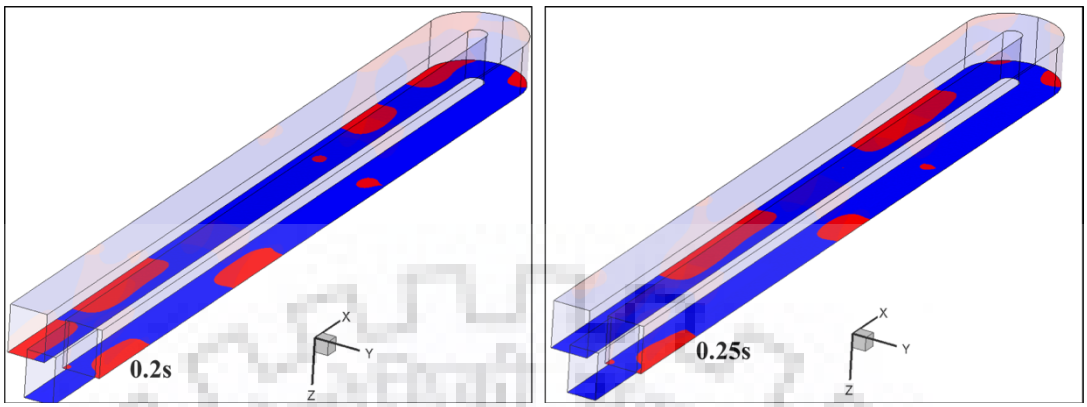

Figure 4.31: Bottom wall contours of slug flow at U_g = 3.33 m/s and U_l = 0.083m/s at 4°/ mm

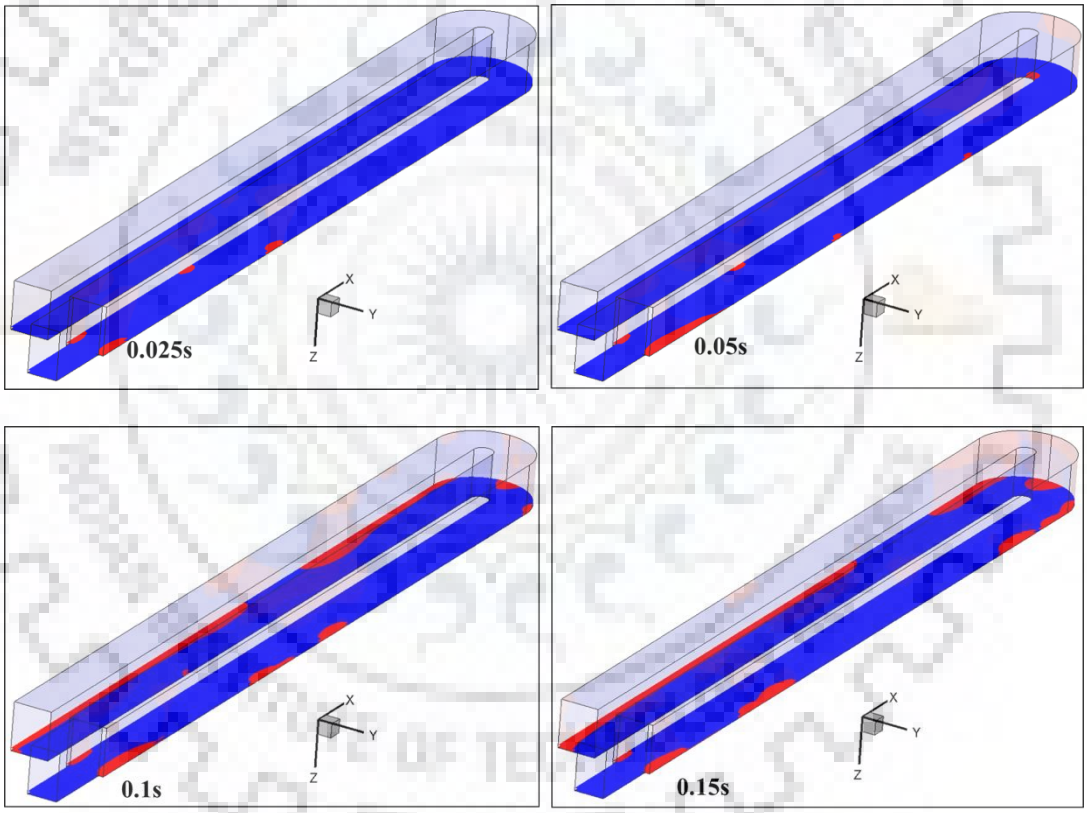

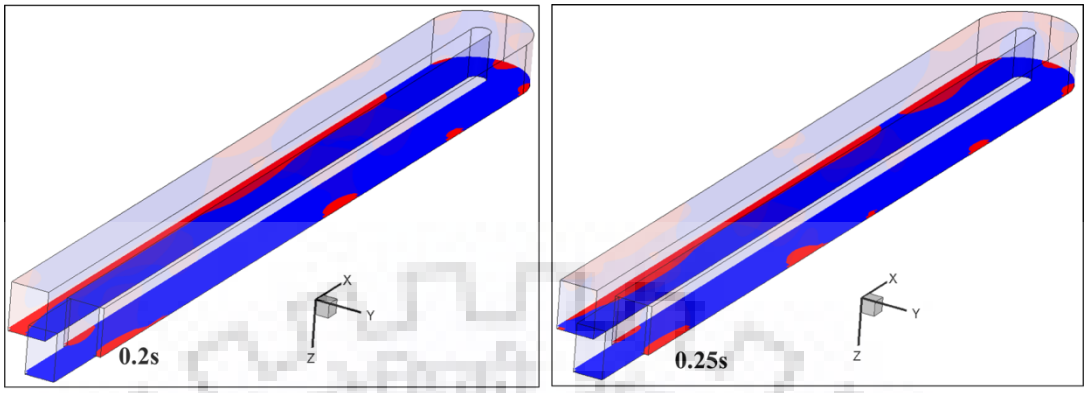

Figure 4.32: Bottom wall contours of slug flow at U_g = 3.33 m/s and U_l = 0.083 m/s at 5°/ mm

Figure 4.30 depicts the phase contours of slug flow in acrylic channel with uniform contact angle of 72°. Red color in the figure shows presence of water and blue indicates presence of air. It can be seen that as the water is introduced small hemispherical slugs are formed and they travel upstream of bend before hitting at bend. At the bend, water can be seen at the outer surface due to centrifugal forces. Formation of slightly distorted slugs at the downstream can be noticed.

Figure 4.31 and 4.32 shows the phase contours for 4˚/mm and 5˚/mm gradient. Figure 4.31 shows at the downstream when the bottom surface becomes gradually hydrophobic, in direction of flow the slugs are well defined. They tend to become spherical in direction of flow as evident from Figure 4.31.

On the other hand, with increasing the gradient to 5˚/mm, the distribution changes completely as shown in Figure 4.32. In this case, it can be seen that at the downstream of bend, instead of slugs, thin film of water is formed. This can be attributed to increase of magnitude of surface force along the contact line of slugs while the inertial force remains same.

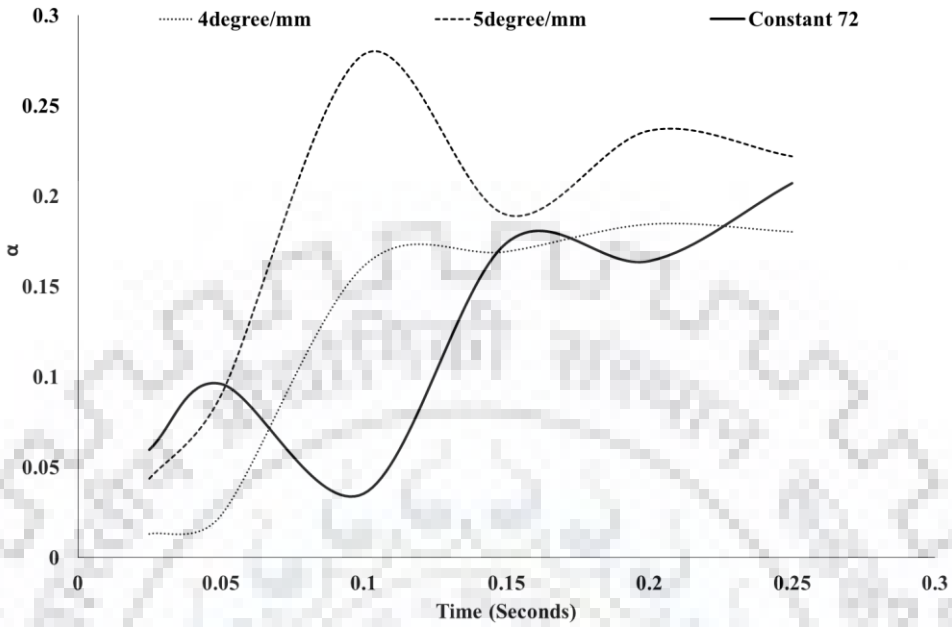

Figure 4.33: Water coverage ratio in slug flow at U_g = 3.33 m/s and U_l = 0.083 m/s with respect to wettability gradient

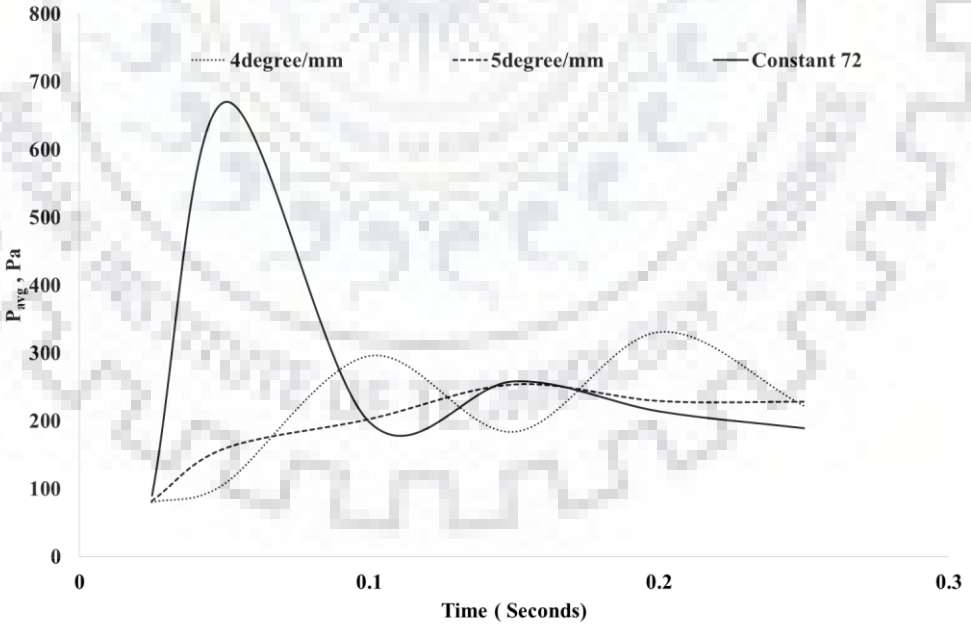

Figure 4.34: Average pressure as a function of time for different GDL surfaces at U_g = 3.33 m/s and U_l = 0.083 m/s

As a result, of increase of surface force in opposite direction of flow, slugs join and form a thin film. Hence, it can be concluded that in case of slug flow there exist a critical value of positive wettability gradient in direction of flow. Increasing the gradient beyond this value converts the slug to film.

Figure 4.33 shows α with time for all the three cases. It can be observed that amount of water retention is higher for 5°/mm gradient. On the other hand, 4°/mm gradient shows an increase of α with time till 0.1 s after that it remains almost constant. From the phase contours of Figure 4.31 it is evident that after 0.01 s the long water film breaks and forms well defined slugs at downstream. For constant 72°, α shows a fluctuating characteristic over time.

Corresponding pressure are plotted in Figure 4.34. It can be seen pressure fluctuates with time both for constant 72° and 4°/mm gradient. This is also evident from experiments, that formation of slugs caused fluctuations in pressure. While it can be depicted a smooth increase for 5°/mm gradient till 0.15 s then decreases slightly.

This is also in agreement with experiments where formation of film structure shows a smooth pressure with time. Figure 4.34 also shows a sharp increase of pressure for constant 72° at 0.05s. From the phase contours of the same in Figure 4.30 it is evident that at 0.05s water sticks to outer surface of the bend, this might lead to increase of pressure at this particular time. Hence it can be said that presence of wettability gradient enhances the chance of formation of slug flow into a more desirable film flow. In such cases, though the instantaneous water retention is higher but are beneficial with respect to pressure fluctuation

CHAPTER 5 CONCLUSION AND SCOPE OF FUTURE WORK

The present study aims to investigate the hydrodynamics of air-water system through extensive experimentation and numerical analysis. The experiments have been performed on air-water through three different serpentine channels. Two of them are falling in the category of mini channel and one of them in range of micro channel. This enable us to identify the influence of hydraulic diameter on the hydrodynamics of flow. Apart from this orientation of the channels are also tested. In all the cases, flow patterns have been identified by high speed video camera and analyzed by image processing software and pressure drop has been measured using differential pressure transmitter. The experimental observations reveal that hydraulic diameter influences range of existence and occurrence of flow regimes. Based on the experimental observations, suitable transition criteria are proposed in terms of phase Weber numbers in all three cases.

In addition, some phenomena which are likely to cause disturbance in case of PEMFC are identified as stagnant region of water and maldistribution in presence of slug flow.

As prediction of pressure can be one of the crucial parameters of operation in such geometries, an expression of modified friction factor has been proposed. This expression has been further tuned in accordance to flow regimes. The friction factor thus obtained can predict the experimental pressure drop with a mean absolute error of 15-18%.

As water removal from serpentine gas flow channels is the desirable for better performance of PEMFC, further attempts have been made to develop CFD models for air-water flow through a single serpentine unit (U shaped geometry) of hydraulic diameter of 1 mm. Commercial CFD software ANSYS FLUENT18 has been used for the simulation. VOF model is used to capture the interface. Extensive investigations are made to understand the pressure and in-situ time averaged phase distribution. In order to remove water effectively, wettability gradients are applied on bottom surfaces. Different types of gradient (positive /negative) and magnitude are tested. Separate user

defined functions are incorporated at bottom surfaces. Three different flow situations are tested suspended drop, drop at bottom surface and slug flow.

5.1. Conclusions

The salient features of the present studies are as follows:

- Annular, slug, ring and churn are the dominating flow patterns observed for the channels. Churn is observed only in channel with D_H of 1.65 mm, while ring and distorted slug are observed only in D_H of 1 mm. In case of D_H of 1.65 mm stagnant region of water is also observed for horizontal orientation. Micro channel favours the formation of annular flow. Range of existence in terms of We_{LS} increased as the confinement number increased. For PEMFC, micro serpentine channels in vertical orientation are desired configuration as they form annular flow which favours draining of water as well as results in lesser pressure drop.

- All the flow regimes for D_H of 1.65 mm and 1 mm are surface tension dominated for present range of experiments, on the other hand majority of the regime for D_H of 0.65 mm regimes are gas inertia dominated. Effect of orientation on flow regime and their range of existence, gradually disappears as the channel characteristics changes from mini to micro. For D_H of 1.65 mm separate transition criteria between flow regimes are noted in terms of phase Weber numbers. However, for D_H 1 mm and 0.65 transition criteria remain same in both orientations.

- Due to effect of gravity vertical orientation has higher pressure drop than horizontal orientation for mini channels. In case of the micro channel, horizontal orientation suffers mal-distribution due to irregular flow distribution inside the channels at low water flow rates inside the channels.

This leads to higher pressure drop in horizontal orientation. With increase of water flow rate flow distributions are more uniform. For micro channel vertical orientation gives 4 times of reduction in non- dimensional pressure in comparison to horizontal orientation of mini channel at similar gas phase Reynolds number.

- New correlations are proposed for friction factor as a function two-phase Reynolds number and Capillary number for these smaller serpentine channels irrespective of their hydraulic diameter. This shows reasonable agreement with experimental data with mean absolute error of 15% in horizontal orientation and 19% in vertical orientation
- In case of suspended drop, it is observed bottom surface wettability gradient influences water coverage of bottom surface. Lesser water coverage always observed for a gradual hydrophobic surface. At higher air velocity, a constant contact angle channel, has higher water retention in comparison to that of a gradual hydrophilic bottom surface. This is attributed to the absence of surface force in the former case. Low air velocity and gradual hydrophobic bottom surface results in lesser pressure drop as well as water coverage
- For removal of water drop situated at the bottom of the surface, it is noticed that presence of a gradual hydrophilic surface in direction of flow at the upstream of bend, changes the dynamics of drop movement. Presence of such a surface accelerates the drop at the upstream of bend. After the drop hits the bend it remains majorly on the top surface. Very little amount of water on bottom surface has been observed.
- In case of slug flow, presence of gradual hydrophobic surface in direction of flow, converts the slugs to film at the downstream of bend, after a threshold value of gradient is reached. Film can be removed easily from the channel and can be helpful in reducing the maldistribution.

5.2. Future work and Recommendations

Based on the information obtained from the present work, the following investigations are recommended as future work.

- The influence of porous media at the bottom of the channel can be explored.
- A CFD modeling of air-water flow through the aforementioned porous geometries. This will enable us to understand the in-situ distribution of water as well as its removal.
- Detailed experimental and theoretical investigations are proposed on effect of injecting air-water in horizontal orientation for reducing mal distribution.
- Mesoscale numerical algorithm can be used to simulate the circulation inside the drops which might clarify the physics of water drop removal in presence of wettability modified surfaces

REFERENCES

1. Akbar MK, Plummer DA, Ghiaasiaan SM. On gas – liquid two-phase flow regimes in microchannels 2003; 29:855–65
2. Anderson R, Blanco M, Bi X, Wilkinson DP. Anode water removal and cathode gas diffusion layer flooding in a proton exchange membrane fuel cell. Int J Hydrogen Energy 2012; 37:16093–103.
3. Anderson R, Wilkinson DP, Bi X, Zhang L. Two-phase flow pressure drop hysteresis in parallel channels of a proton exchange membrane fuel cell. J Power Sources 2010; 195:4168–76.
4. Anderson R, Zhang L, Ding Y, Blanco M, Bi X, Wilkinson DP. A critical review of two-phase flow in gas flow channels of proton exchange membrane fuel cells. J Power Sources 2010; 195:4531–53.
5. Ashrafi M, Shams M. The effects of flow-field orientation on water management in PEM fuel cells with serpentine channels. Appl Energy 2017; 208:1083–96.
6. Banerjee R, Kandlikar SG. Liquid water quantification in the cathode side gas channels of a proton exchange membrane fuel cell through two-phase flow visualization. J Power Sources 2014; 247:9–19.
7. Barreto EX, Oliveira JLG, Passos JC. International Journal of Multiphase Flow Frictional pressure drop and void fraction analysis in air – water two-phase flow in a microchannel. Int J Multiph Flow 2015; 72:1–10.
8. Bozorgnezhad A, Shams M, Kanani H, Hasheminasab M, Ahmadi G. The experimental study of water management in the cathode channel of single-serpentine transparent proton exchange membrane fuel cell by direct visualization. Int J Hydrogen Energy 2015; 40: 2808–32.
9. Cai YH, Hu J, Ma HP, Yi BL, Zhang HM. Effects of hydrophilic/hydrophobic properties on the water behaviour in the micro-channels of a proton exchange membrane fuel cell. J Power Sources 2006; 161:843–8.

10. Carton JG, Lawlor V, Olabi AG, Hochenauer C, Zauner G. Water droplet accumulation and motion in PEM (Proton Exchange Membrane) fuel cell mini channels. Energy 2012; 39:63–73
11. Charnay R, Bonjour J, Revellin R. Experimental investigation of R-245fa flow boiling in minichannels at high saturation temperatures: Flow patterns and flow pattern maps. Int. J. Heat Fluid Flow 2014;46: 1–16.
12. Chen L, He YL, Tao WQ. Effects of surface microstructures of gas diffusion layer on water droplet dynamic behaviors in a micro gas channel of proton exchange membrane fuel cells. Int J Heat Mass Transf 2013;60:252–62
13. Chen YS, Peng H. Studying the Water Transport in a Proton Exchange Membrane Fuel Cell by Neutron Radiography and Relative Humidity Sensors. J Fuel Cell Sci Technol 2009; 6: 031016.
14. Chinnov EA, Ron'shin F V, Kabov OA. Two-phase flow patterns in short horizontal rectangular microchannels. Int J Multiph Flow 2016; 80:57–68.
15. Choi C, Kim M. Flow pattern based correlations of two-phase pressure drop in rectangular microchannels. Int J Heat Fluid Flow 2011; 32: 1199–207.
16. Coeuriot V, Dillet J, Maranzana G, Lottin O, Didierjean S. An ex-situ experiment to study the two-phase flow induced by water condensation into the channels of proton exchange membrane fuel cells (PEMFC). Int J Hydrogen Energy 2015; 40:1–12.
17. Coleman JW, Garimella S. Characterization of two-phase flow patterns in small diameter round and rectangular tubes. Int J Heat Mass Transf 1999; 42:2869–81.
18. Daniel S, Chaudhury MK. Rectified motion of liquid drops on gradient surfaces induced by vibration. Langmuir 2002; 18:3404-3407.
19. Daniel S, Sircar S, Gliem J, Chaudhury MK. Ratcheting motion of liquid drops on gradient surfaces. Langmuir 2004; 20:4085–92.
20. Das G, Das PK, Purohit NK, Mitra AK. Liquid Holdup in Concentric Annuli during Cocurrent Gas-Liquid Upflow. Can J Chem Eng 2002; 80:153–7.

21. Datta D, Gada VH, Sharma A. Analytical and Level-Set Method-Based Numerical Study for Two-Phase Stratified Flow in a Plane Channel and a Square Duct. Numer Heat Transf Part A Appl 2011;7782.
22. De B, Mandal TK, Das G. The rivulet flow pattern during oil – water horizontal flow through a 12 mm pipe. Exp Therm Fluid Sci 2010; 34:625–32.
23. Del Col D, Bisetto A, Bortolato M, Torresin D, Rossetto L. Experiments and updated model for two phase frictional pressure drop inside minichannels. Int J Heat Mass Transf 2013; 67:326–37.
24. Demori M, Ferrari V, Strazza D, Poesio P. A capacitive sensor system for the analysis of two-phase flows of oil and conductive water. Sensors Actuators A Phys 2010;163:172–9.
25. Donaldson AA, Kirpalani DM, Macchi A. Single and two-phase pressure drop in serpentine mini-channels. Chem Eng Process Process Intensif 2011; 50:877–84.
26. Dutta S, Shimpalee S, Van Zee JW. Three-dimensional numerical simulation of straight channel PEM fuel cells. J Appl Electrochem 2000; 30:135–46.
27. Engelbrecht N, Chiuta S, Everson RC, Neomagus HWJP, Bessarabov DG, À L. Experimentation and CFD modelling of a microchannel reactor for carbon dioxide methanation. Chem Eng J 2016; 313:847–57
28. English NJ, Kandlikar SG. An experimental investigation into the effect of surfactants on air-water two-phase flow in minichannels. Heat Transf Eng 2006; 27:99–109
29. Falsetti C, Jafarpoorchekab H, Magnini M, Borhani N, Thome JR. Two-phase operational maps, pressure drop, and heat transfer for flow boiling of R236fa in a micro-pin fin evaporator. Int J Heat Mass Transf 2017;107:805–19.
30. Ferreira RB, Falcão DS, Oliveira VB, Pinto AMFR. Numerical simulations of two-phase flow in an anode gas channel of a proton exchange membrane fuel cell. Energy 2015; 82:619–28

31. Flipo G, Josset C, Bellettre J, Auvity B. Clarification of the surface wettability effects on two-phase flow patterns in PEMFC gas channels. Int J Hydrogen Energy 2016; 41:15518–27.
32. Gada VH, Sharma A. On Derivation and Physical Interpretation of Level Set Method – Based Equations for Two-Phase Flow Simulations. Numer Heat Transf, Part B Fundam 2009;7790:307–22
33. Ghosh S, Patil P, Mishra SC, Das AK, Das PK. 3-D Lattice Boltzmann model for asymmetric Taylor bubble and Taylor drop in inclined channel. Eng Appl Comput Fluid Mech 2012; 6:383–94.
34. Gogate PR, Shirgaonkar IZ, Sivakumar M, Senthilkumar P, Vichare NP, Pandit AB. Cavitation Reactors: Efficiency Assessment Using a Model Reaction. AIChE J 2001; 47: 2526–38.
35. Greenspan HP. On the motion of a small viscous droplet that wets a surface. J Fluid Mech 1978; 84:125.
36. Grimm M, See EJ, Kandlikar SG. Modeling gas flow in PEMFC channels: Part I Flow pattern transitions and pressure drop in a simulated ex-situ channel with uniform water injection through the GDL. Int J Hydrogen Energy 2012; 37:12489–503.
37. Gueyffier D, Li J, Nadim A, Scardovelli R, Zaleski S. Volume-of-Fluid Interface Tracking with Smoothed Surface Stress Methods for Three-Dimensional Flows. J Comput Phys 1999; 152: 423–56.
38. Gunstensen AK, Rothman DH, Zaleski S. Lattice Boltzmann model of i mmiscible fuids. Phys Rev A 1991; 43:4320–7.
39. Harries N, Burns JR, Barrow DA, Ramshaw C. A numerical model for segmented flow in a microreactor. Int J Heat Mass Transf 2003; 46:3313–22
40. Hussaini IS, Wang CY. Visualization and quantification of cathode channel flooding in PEM fuel cells. J Power Sources 2009; 187:444–51.
41. Ide H, Kariyasaki A, Fukano T. Fundamental data on the gas–liquid two-phase flow in minichannels. Int J Therm Sci 2007; 46:519–30.

42. Idelchik, I. E.1986. Handbook of hydraulic resistance, Hemisphere, New York.
43. Iliev SD. Static drops on an inclined plane: Equilibrium modeling and numerical analysis. J Colloid Interface Sci 1997; 194:287–300.
44. Iranzo A, Biesdorf J, Cochet M, Salva A, Boillat P, Rosa F. Effect of Serpentine Multi-pass Flow Field Channel Orientation in the Liquid Water Distributions and Cell Performance. Fuel Cells 2016; 16:777–83.
45. Iranzo A, Boillat P, Biesdorf J, Salva A. Investigation of the liquid water distributions in a 50cm^2 PEM fuel cell: Effects of reactants relative humidity, current density, and cathode stoichiometry. Energy 2015; 82:914–21.
46. Iranzo A, Boillat P, Biesdorf J, Tapia E, Salva A, Guerra J. Liquid water preferential accumulation in channels of PEM fuel cells with multiple serpentine flow fields. Int J Hydrogen Energy 2014; 39:15687–95
47. Jiao K, Zhou B, Quan P. Liquid water transport in parallel serpentine channels with manifolds on cathode side of a PEM fuel cell stack. J Power Sources 2006; 154:124–37.
48. Jiao K, Zhou B, Quan P. Liquid water transport in straight micro-parallel-channels with manifolds for PEM fuel cell cathode. J Power Sources 2006; 157:226–43.
49. Jiao K, Zhou B. Effects of electrode wettabilities on liquid water behaviours in PEM fuel cell cathode. J Power Sources 2008; 175:106–19.
50. Jo D, Revankar ST. Effect of coalescence and breakup on bubble size distributions in a two-dimensional packed bed. Chem Eng Sci 2010; 65: 4231–8.
51. Jo JH, Kim WT. Numerical simulation of water droplet dynamics in a right angle gas channel of a polymer electrolyte membrane fuel cell. Int J Hydrogen Energy 2015; 40:8368–83.
52. Johnson NA, Das S, Sen AK. Effects of Copper Corrosion in the Performance of Polymer Electrolyte Membrane Fuel Cells. ECS Trans 2017; 80: 477–83.

53. Kandlikar SG, Lu Z, Domigan WE, White AD, Benedict MW. Measurement of flow maldistribution in parallel channels and its application to ex-situ and in-situ experiments in PEMFC water management studies. Int J Heat Mass Transf 2009; 52:1741–52.
54. Kandlikar SG. Fundamental issues related to flow boiling in minichannels and microchannels. Exp Therm Fluid Sci 2002; 26:389–407.
55. Kim HJ, Kim TW. Numerical Investigation of Gas-Liquid Two-Phase Flow inside PEMFC Gas Channels with Rectangular and Trapezoidal Cross Sections. Energies 2018;11:1–18
56. Kimball E, Whitaker T, Kevrekidis YG, Benziger JB. Drops, slugs, and flooding in polymer electrolyte membrane fuel cells. AIChE Journal. 2008 May 1;54(5):1313-32.
57. Kirpalani DM, Patel T, Mehrani P, Macchi A. Experimental analysis of the unit cell approach for two-phase flow dynamics in curved flow channels. Int J Heat Mass Transf 2008; 51:1095–103.
58. Kumar SR, Sharma A, Agrawal A. Simulation of flow around a row of square cylinders. J Fluid Mech 2008; 606:369–97
59. Leclerc A, Philippe R, Houzelot V, Schweich D, Bellefon C De. Gas – liquid Taylor flow in square micro-channels: New inlet geometries and interfacial area tuning. Chem Eng J 2010; 165:290–300.
60. Lee, J., Mudawar, I. Two-phase flow in high-heat-flux micro-channel heat sink for refrigeration cooling applications: Part II — heat transfer characteristics. Int. J. Heat Mass Transf. 2005;48, 941–955.
61. Li H, Tang Y, Wang Z, Shi Z, Wu S, Song D, et al. A review of water flooding issues in the proton exchange membrane fuel cell. J Power Sources 2008; 178:103–17.
62. Lin S, Kwok CCK, Li R.Y, Chen ZH, Chen YZ, 1991. Local frictional pressure drop during vaporization of R-12 through capillary tubes. Int. J. Multiph. Flow 17, 95–102.

63. Lockhart RW, Martinelli RC. Proposed Correlation of Data for Isothermal Two-Phase, Two-Component Flow in Pipes. Chem Eng Prog 1949; 45:39–48.
64. Lu Z, Kandlikar SG, Rath C, Gri mm M, Domigan W, White AD. Water management studies in PEM fuel cells, Part II: Ex-situ investigation of flow maldistribution, pressure drop and two-phase flow pattern in gas channels. Int J Hydrogen Energy 2009; 34:3445–56.
65. Lu Z, Rath C, Zhang G, Kandlikar SG. Water management studies in PEM fuel cells, part IV: Effects of channel surface wettability, geometry and orientation on the two-phase flow in parallel gas channels. Int J Hydrogen Energy 2011; 36:9864–75.
66. Malapure VP, Mitra SK, Bhattacharya A. Numerical investigation of fluid flow and heat transfer over louvered fins in compact heat exchanger. Int J Therm Sci 2007; 46: 199–211.
67. Malhotra S, Deshpande A, Ghosh S. International Journal of Multiphase Flow Air – water flow through a single serpentine mini channel – flow distribution and pressure drop. Int J Multiph Flow 2017; 96:48–55.
68. Mandal TK, Das G, Das PK. International Journal of Multiphase Flow An appraisal of liquid – liquid slug flow in different pipe orientations. Int J Multiph Flow 2010; 36: 661–71.
69. Manke I, Hartnig C, Grünerbel M, Lehnert W, Kardjilov N, Haibel A. Investigation of water evolution and transport in fuel cells with high resolution synchrotron x-ray radiography. Appl Phys Lett 2007; 90:3–5.
70. Manke I, Hartnig C, Kardjilov N, Messerschmidt M, Hilger A, Strobl M, Characterization of water exchange and two-phase flow in porous gas diffusion materials by hydrogen-deuterium contrast neutron radiography Characterization of water exchange and two-phase flow in porous gas diffusion materials by hydrogen-deuterium contra 2008;244101:1–4.
71. Mansour M, Kawahara A, Sadatomi M. Numerical Investigation of Two-Phase Flow through a T-Junction Microchannel Reactor. J Environ Sci Eng 2014; 3:42–54

72. Maria MS, Rakesh PE, Chandra TS, Sen AK. Capillary flow-driven microfluidic device with wettability gradient and sedimentation effects for blood plasma separation. Nat Publ Gr 2017:1–12.
73. Megahed, A, Hassan I. Two-phase pressure drop and flow visualization of FC-72 in a silicon microchannel heat sink. Int. J. Heat Fluid Flow 2009;30, 1171–1182.
74. Mishima K, Hibiki T. Some characteristics of air-water two-phase flow in small diameter vertical tubes. Int J Multiph Flow 1996; 22:703–12.
75. Onea A, Martin W, Cacuci DG. A qualitative computational study of mass transfer in upward bubble train flow through square and rectangular mini-channels. Chem Eng Sci 2009; 64:1416–35
76. Pamitran, AS, Choi K, Oh J, Hrnjak P. Characteristics of two-phase flow pattern transitions and pressure drop of five refrigerants in horizontal circular small tubes. Int. J. Refrig. 2010;33, 578–588
77. Pant LM, Mitra SK, Secanell M. Absolute permeability and Knudsen diffusivity measurements in PEMFC gas diffusion layers and micro porous layers. J Power Sources 2012; 206: 153–60.
78. Patankar VS. Numerical Heat Transfer and Fluid Flow, Hemisphere, Washington, DC; 1980
79. Pramod K, Sen AK. Flow and Heat Transfer Analysis of an Electro-Osmotic Flow Micropump for Chip Cooling. J Electron Packag 2018; 136: 1–14.
80. Qian D, Lawal A. Numerical study on gas and liquid slugs for Taylor flow in a T-junction microchannel. Chem Eng Sci 2006; 61:7609–25
81. Qin Y, Du Q, Yin Y, Jiao K, Li X. Numerical investigation of water dynamics in a novel proton exchange membrane fuel cell flow channel. J Power Sources 2013; 222:150–60.
82. Qin Y, Yin Y, Jiao K, Du Q. Effects of needle orientation and gas velocity on water transport and removal in a modified PEMFC gas flow channel having a hydrophilic needle. Int J Energy Res. 2018;1–12.

83. Qiu B, Yang Q, Yan J, Revankar ST. Experimental investigation on the propagation characteristics of pressure oscillation in direct contact condensation with low mass flux steam jet. Exp Therm Fluid Sci 2017; 88: 400–8.
84. Quan P, Zhou B, Sobiesiak A, Liu Z. Water behavior in serpentine micro-channel for proton exchange membrane fuel cell cathode. J Power Sources 2005; 152:131–45.
85. Raj A, Suthanthiraraj PPA, Sen AK. Pressure-driven flow through PDMS-based flexible microchannels and their applications in microfluidics. Microfluid Nanofluidics 2018; 22: 128.
86. Rothman DH, Zaleski S. Lattice-gas models of phase separation: and multiphase flow. Rev Mod Phys 1994; 66: 1417–96.
87. Saha A, Mitra SK. Effect of dynamic contact angle in a volume of fluid (VOF) model for a microfluidic capillary flow. J Colloid Interface Sci 2009; 339:461–80.
88. Saisorn S, Wongwises S. The effects of channel diameter on flow pattern, void fraction and pressure drop of two-phase air-water flow in circular micro-channels. Exp Therm Fluid Sci 2010; 34:454–62
89. Serizawa A, Feng Z, Kawara Z. Two-phase flow in microchannels. Exp Therm Fluid Sci 2002; 26:703–14.
90. Sharma M, Ravi P, Ghosh S, Das G, Das PK. Studies on low viscous oil-water flow through return bends. Exp Therm Fluid Sci 2011; 35:455–69.
91. Sivakumar M, Pandit AB. Ultrasound enhanced degradation of Rhodamine B: optimization with power density. Ultrason Sonochem 2001; 8: 233–40.
92. Song M, Kim H-Y, Kim K. Effects of hydrophilic/hydrophobic properties of gas flow channels on liquid water transport in a serpentine polymer electrolyte membrane fuel cell. Int J Hydrogen Energy 2014; 39:19714–21.
93. Soupremanien U, Person S Le, Favre-Marinet M, Bultel Y. Influence of the aspect ratio on boiling flows in rectangular mini-channels. Exp Therm Fluid Sci 2011; 35:797–809

94. Steinbrenner JE, Lee ES, Hidrovo CH, Eaton JK, Goodson KE. Impact of channel geometry on two-phase flow in fuel cell microchannels. J Power Sources 2011; 196:5012–20.
95. Strazza D, Demori M, Ferrari V, Poesio P. Capacitance sensor for hold-up measurement in high-viscous-oil / conductive-water core-annular flows. Flow Meas Instrum 2011; 22: 360–9.
96. Suda H, Yamada S. Force measurements for the movement of a water drop on a surface with a surface tension gradient. Langmuir 2003; 19:529–31.
97. Suo M, Griffith P, Two-phase flow in capillary tubes. J. Basic Eng. 1964; 86: 576–82.
98. Timung S, Tiwari V, Singh AK, Mandal TK, Bandyopadhyay D. Capillary force mediated flow patterns and non-monotonic pressure drop characteristics of oil-water microflows. Can J Chem Eng 2015; 93:1736–43.
99. Tran TN, Chyu M, Wambsganss MW, France DM. Two-phase pressure drop of refrigerants during flow boiling in small channels: an experimental investigation and correlation development. Int J Multiph Flow 2000; 26:1739–54
100. Triplett KA, Ghiaasiaan SM, Abdel-Khalik SI, Sadowski DL. Gas–liquid two-phase flow in microchannels Part I: two-phase flow patterns. Int J Multiph Flow 1999; 25:377–94.
101. Venkatesan M, Das SK, Balakrishnan AR. Effect of tube diameter on two-phase flow patterns in mini tubes. Can J Chem Eng 2010; 88:936–44
102. Wang Y, Al Shakhshir S, Li X, Chen P. Superhydrophobic flow channel surface and its impact on PEM fuel cell performance. Int J Low-Carbon Technol 2012; 9:225–36.
103. Wook Y, Kim MS. The pressure drop in microtubes and the correlation development. Int. J. Heat Mass Transf. 2006; 49:1804–12.
104. Yan Y, Lin F. Evaporation heat transfer and pressure drop of refrigerant R-134a in a small pipe. Int J Heat Mass Transf J Heat Mass Transf 1998:4183–94

105. Yang C, Webbt RL. Friction pressure drop of R-12 in small hydraulic diameter extruded aluminum tubes with and without micro-fins. Int J Heat Mass Transf 1996; 39:801–9
106. Yu W, France DM. Two-phase pressure drop, boiling heat transfer, and critical heat flux to water in a small-diameter horizontal tube. Int J Multiph Flow 2002; 28:927–41
107. Yue J, Luo L, Gonthier Y, Chen G, Yuan Q. An experimental investigation of gas – liquid two-phase flow in single microchannel contactors. Chem Eng Sci 2008; 63:4189–202.
108. Zhang L, Bi HT, Wilkinson DP, Stumper J, Wang H. Gas – liquid two-phase flow patterns in parallel channels for fuel cells 2008; 183:643–50.
109. Zhang L, Bi XT, Wilkinson DP, Anderson R, Stumper J, Wang H. Gas-liquid two-phase flow behavior in minichannels bounded with a permeable wall. Chem Eng Sci 2011; 66:3377–85.
110. Zhang L, Du W, Bi HT, Wilkinson DP, Stumper J, Wang H. Gas – liquid two-phase flow distributions in parallel channels for fuel cells 2009; 189: 1023–31.
111. Zhang M, Webb RL. Correlation of two-phase friction for refrigerants in small-diameter tubes. Exp Therm Fluid Sci 2001; 25:131–9
112. Zhang P, Yao C, Ma H, Jin N, Zhang X, Lü H, et al. Dynamic changes in gas-liquid mass transfer during Taylor flow in long serpentine square microchannels. Chem Eng Sci 2018; 82:17–27.
113. Zhang W, Hibiki T, Mishima K. Correlations of two-phase frictional pressure drop and void fraction in mini-channel. Int. J. Heat Mass Transf. 2010; 53: 453–65.
114. Zhao TS, Bi QC. Co-current air water two-phase fow patterns in vertical triangular microchannels. Int J Multiph Flow 2001; 27:765–82.
115. Zhao Y, Chen G, Ye C, Yuan Q. Gas – liquid two-phase flow in microchannel at elevated pressure. Chem Eng Sci 2013; 87:122–32.

116. Zhenyu S, Zhanqiang L, Hao S, Xianzhi Z. Prediction of contact angle for hydrophobic surface fabricated with micro-machining based on minimum Gibbs free energy. Appl Surf Sci 2016; 364:597–60.
117. Zhou W, Henderson G, Revankar ST. Condensation in a vertical tube bundle passive condenser – Part 1: Through flow condensation. Int J Heat Mass Transf 2010; 53:1146–55
118. Zhou K, Coyle C, Li J, Buongiorno J, Li W. Flow boiling in vertical narrow microchannels of different surface wettability characteristics. Int J Heat Mass Transf 2017;109:103–14.
119. Zhou Y, Chang H, Qi T. Chinese Journal of Chemical Engineering Gas – liquid two-phase flow in serpentine microchannel with different wall wettability. Chinese J Chem Eng 2017; 25:874–81.

LIST OF PUBLICATIONS

List of Publications

1. Malhotra S, Deshpande A, Ghosh S. Air – water flow through a single serpentine mini channel – flow distribution and pressure drop. Int J Multiph Flow 2017; 96:48–55
2. Malhotra S, Ghosh S. Effect of Gas Diffusion Layer Surface Wettability Gradient on Water Behavior in a Serpentine Gas Flow Channel of Proton Exchange Membrane Fuel Cell. J Fluids Eng Trans ASME 2018;140.
3. Malhotra S, Ghosh S. Effects of channel diameter on flow pattern and pressure drop for air–water flow in serpentine gas channels of PEM fuel cell-An Ex-situ experiment. Exp Therm Fluid Sci 2019; 100:233–50.